Study on Stretch Fabrication of ETFE Tensile Membrane Structures Considering Friction Contact Conditions

(摩擦接触条件を考慮する ETFE フィルムを用いた
膜構造の延伸成形に関する研究)

Graduate School of Urban Innovation
Yokohama National University, Japan

Doctoral Thesis

BUI QUANG HIEU
ブイ　クアン　ヒヨウ

March 2019

Study on Stretch Fabrication of ETFE Tensile Membrane Structures Considering Friction Contact Conditions

Abstract

This thesis is a summary of study on stretch fabrication of saddle type of tensile membrane structures using ETFE (Ethylene tetrafluoroethylene) film considering the effect of friction contact between the film and the supporting galvanized steel arches.

In this thesis, the analytical method which could solve the geometrical nonlinearity, the material nonlinearity and the nonlinearity of friction contact conditions is proposed to evaluate the prestress distribution on the membrane material and the effect of friction contact during the introduced prestress stage in tensile membrane structures. In addition, the stretch fabrication technique for saddle type of ETFE tensile membrane structure with less weld lines by drawing the combination of plane and drape strips is also suggested.

This thesis comprises six chapters, as described below:

Chapter 1, "*Introduction*", presents the proposed stretch fabrication method and its problems for establishing the smooth curved surface of tensile membrane structures using ETFE film. The motivation, the background and the purposes of this thesis are also indicated in this chapter.

Chapter 2, "*Review on form finding and cutting pattern analysis*", describes a review on the form finding and cutting pattern analysis for tensile membrane structures. The saddle type of tensile membrane structure is investigated in this chapter. This structure comprises the outside frame, two supporting arches and ETFE film. The part of the film between two arches is called middle part, while the part between arch and outside frame is called corner part. First, the form finding analysis is carried out with several prescribed stress ratios between machine direction (MD) and transverse direction (TD) for both middle and corner parts. Second, the cutting pattern analysis based on the mathematical approach produces the drape strips which correspond to the shapes obtained from form finding. The effectiveness of weld and drawing works of those drape strips is also discussed in this chapter.

Chapter 3, "*Fabrication of three-dimensional (3D) curved surface using ETFE film by stretching plane strips*", presents the stretch fabrication experiments on the establishment of 3D curved surface of saddle type membrane structures using ETFE film by stretching the combination of plane strips, which was not draped, for the middle part and drape strips for the corner parts. The possibility of fabrication of low-rise 3D curved surface is confirmed, while the establishment of high-rise 3D smooth curved surface by drawing the plane strips still has

problems because of the occurrence of wrinkling and insufficient prestress. The measurement method for pre-tensile strains and prestresses on ETFE film is also presented. In addition, the slide between ETFE film and the supporting galvanized steel arch is investigated.

Chapter 4, "*Total Lagrangian formulation for ETFE tensile membrane structure considering friction contact*", introduces the total Lagrangian formulations for both triangular membrane element and node-to-node contact element. The analytical procedure, which uses these elements, is suggested to solve the geometrical nonlinearity problem, the material nonlinearity problem and the nonlinearity problem of friction contact conditions. The suggested analytical method is in high agreement with commercial software ANSYS for the frictionless case. Moreover, this method indicates the effectiveness for friction contact case too. The results of the experiments in Chapter 3 partially confirm the suggested analytical method for the 0.3 of static friction coefficient between ETFE film and galvanized steel arch.

Chapter 5, "*Fabrication of three-dimensional (3D) ETFE curved surface by stretching drape strips considering friction contact*", shows the stretch fabrication technique on the establishment of 3D curved surface of saddle type of ETFE tensile membrane structures considering the friction contact conditions. First, a test on static friction coefficient between ETFE film and steel pipes, which are black and galvanized types, is proposed. Second, the cutting pattern strips or drape strips, which are obtained in Chapter 2, are used to make the specimens. Third, the analytical method of Chapter 4 predicts the values of drawing boundary. This prediction will guarantee the absence of wrinkling and the sufficiency of introduced prestress. Finally, the stretch fabrication experiments will be carried out. The establishment of high-rise 3D smooth curved surface by drawing the drape strips for both middle and corner parts is confirmed by this fabrication technique. In addition, the pressurization test is carried out to confirm the strength of the structure after above construction stage.

Chapter 6, "*Conclusion*", describes a summary of suggested analytical method and its application on stretch fabrication method for saddle type of tensile membrane structure using ETFE film. The thesis concludes with a discussion, how and to which extent, the tools and results obtained can be used for the design and the construction of ETFE tensile membrane structure.

Contents

List of Figures

Chapter 1.
Introduction

Chapter 1. Introduction

1.1 Motivation and research background

1.1.1. Curved surface fabrication of tensile membrane structure

The tensile membrane structures are now being widely used in public buildings. These structures possess a great of distinct advantages such as light-weight of membrane material, a variety of aesthetically pleasing shapes and the facility for prefabrication. As a result, there have a great number of public buildings, such as Rome Olympic Stadium, Hiroshima Hakuryu Dome, using tensile membrane structures.

Rome Olympic Stadium, Italy Hakuryu Dome, Hiroshima, Japan

Figure 1.1 Examples of tensile membrane structure

The membrane material is thin and flexible, so it has in-plane but not flexural stiffness. When the minimum principle stress of in-plane direction is smaller than zeros, the wrinkling occurs, and the strength of the structure decreases [KI90], [BT92]. Therefore, the determination of an initial configuration in which the specified prestresses are in equilibrium is necessary in the preliminary design of tensile membrane structure. This process is so-called form finding. Generally, the shapes obtained by form finding process are in doubly curved surface, while the membrane material itself is manufactured in plane panel. As a result, the strips of membrane material are cut and joined together to produce the desired curved surface. This period is so-called cutting pattern. On the fabricated tensile membrane surface, there are two main ways of introduction of prestress. First, tension is introduced on the boundary edges. Second, tension is introduced by applying a forced displacement by pushing up the main pole [KI99]. This period is so-called prestress introduction or drawing period. Generally, the stress state of final shape is different with the prescribed stress state of form finding period. So, the compensation process is essential to overcome this discrepancy by optimizing the cutting pattern strips. In summary, the curved surface fabrication of tensile membrane structure has five periods which are

described in Figure 1.2.

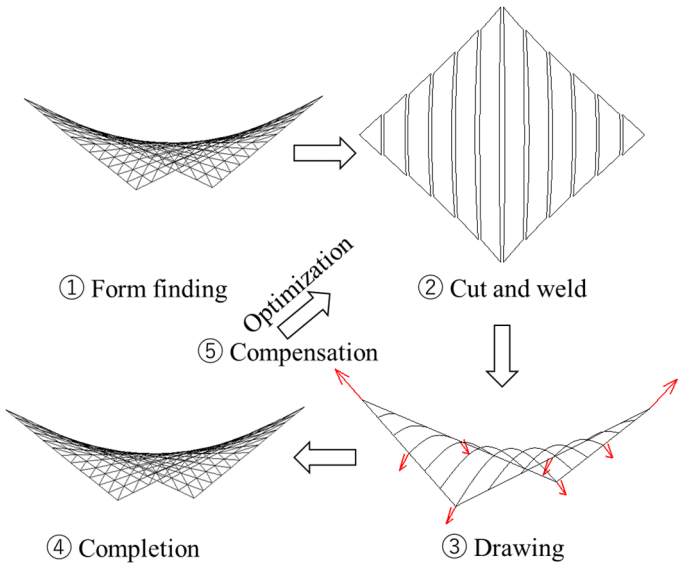

Figure 1.2 Curved surface fabrication of tensile membrane structure

When the shape of structure is complicated, or the curvature of curved surface is high, it is necessary to divide the curved surface finely in above method of curved surface fabrication. As a result, the weld lines increase. This increment will affect not only on the reduction of material strength but also on the aesthetic of the tensile structures. Besides, the ETFE film is widely used in membrane structures in recent years. Because this film has special properties, which will be introduced in section *1.1.2*, the possibility of fabrication of a low-rise panel with high yield strength or of a high-rise panel of smooth curved surface with a few of weld lines should be investigated.

1.1.2. Properties of ETFE film

The stress-strain curves of Ethylene tetrafluoroethylene (ETFE) film under uniaxial tensile tests indicated that this material had two yield points *[MW08], [MK08], [CG11]*. While the first yield point was observed at a very low level of strain of around *2%*, the second yield point occurred at around *13%* of strain. After the second yield point was reached, the film could be elongated up to *400%* before failing. Figure 1.3 shows the stress and strain curve of ETFE film under uniaxial tensile test *[MK08]*.

The yield strength of ETFE film was increased by drawing the film to its plastic region *[EJ14]*. However, drawing the film was coupled with the reduction of thickness, the decrease of tear resistance. Therefore, *10%* to *20%* of drawing was the optimal under uniaxial elongation *[MK08]*, while *5%* to *10%* was recommend in case of biaxial elongation *[EJ13]*.

Liked to other polymer materials, ETFE film possessed a complicated viso-elastic behavior

and a complex visco-plastic behavior. The constitutive equation of viso-elastic characteristics was investigated by Moriyama [FM06], while that equation for visco-plastic characteristics was obtained by Jeong [EJ13].

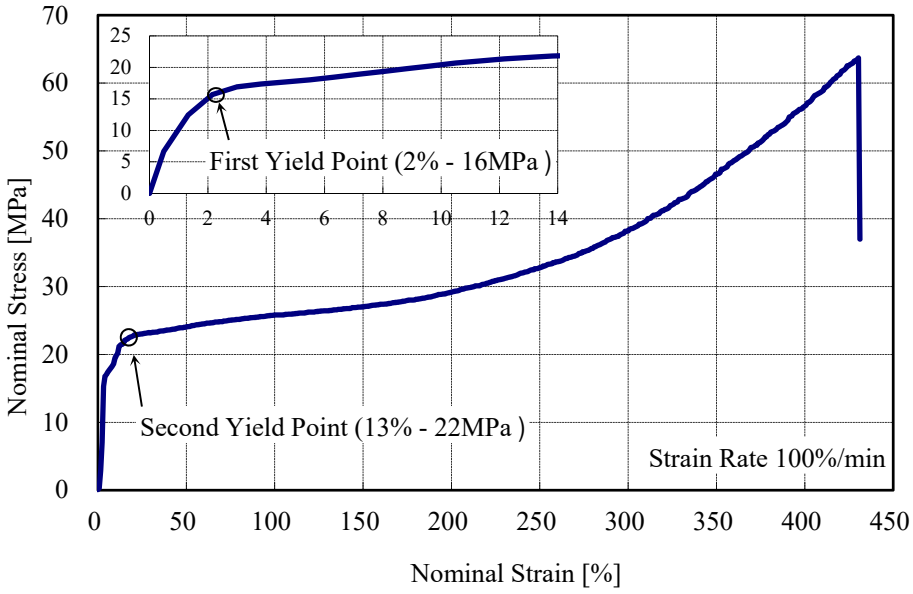

Figure 1.3 Stress strain curve of ETFE film under uniaxial loading

1.1.3. Proposed fabrication method for establishing curved surface of tensile membrane structures using ETFE film

The pre-tensile stress of tensile membrane structure is introduced by drawing the boundary edges or pushing up the main pole according to section *1.1.1*. In case of ETFE material, the film is recommended to draw into its plastic region because of the increment of yield strength and the reduction of tension due to the viscous characteristics. It is easy to draw uniaxial direction, however, there have been few cases that performed biaxial elongation, especially in three-dimensional (3D) shape. Jeong suggested a method of drawing the ETFE film from the plane strips, which was not draped, to 3D curved surface [EJ13]. Figure 1.4 shows the process of his method. First, the plane film was fixed with outside frame. Second, the arch was pushed to make the curved surface. However, this method was limited by the simple shapes of structures and the necessary of flat outside frame. Therefore, this thesis suggests a method in which the possibility of fabrication of curved surfaced from plane or drape strips can be checked. The process of proposed fabrication method is presented in Figure 1.5.

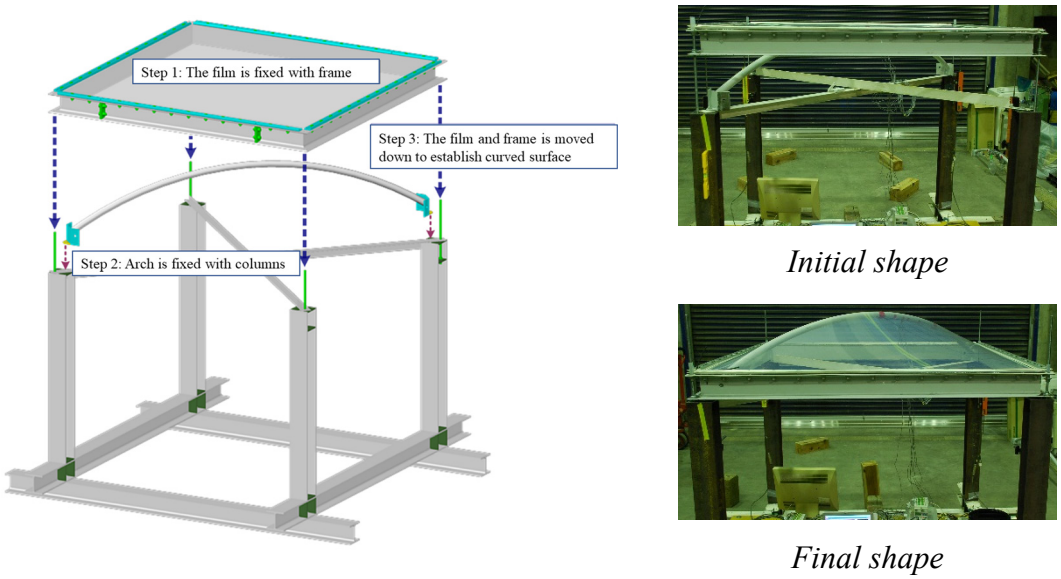

Figure 1.4 Process of E. Jeong method

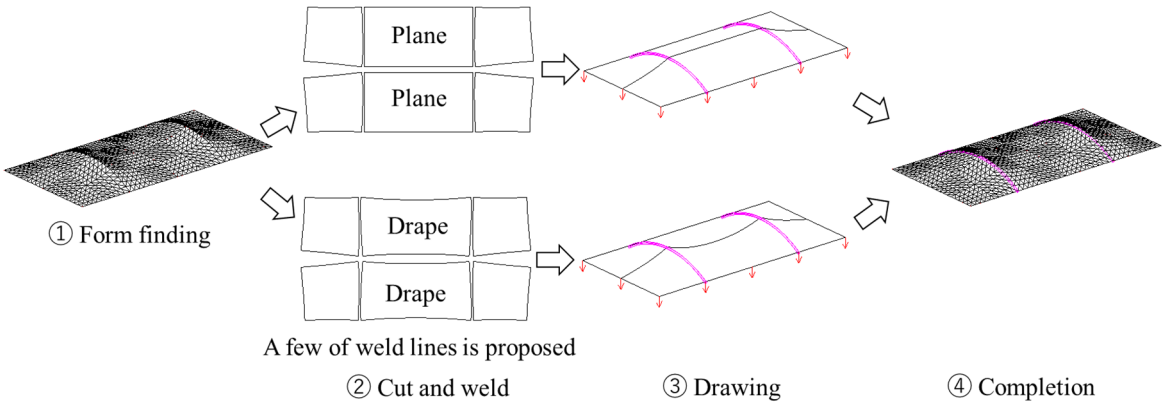

Figure 1.5 Proposed method for curved surface fabrication using ETFE film

In proposed fabrication method, the saddle type of tensile membrane structure is investigated. This structure comprises the outside frame, two supporting arches and ETFE film. The parts of the film between two arches are called middle parts, while the parts between arch and outside frame are called corner parts. First, the form finding analysis is carried out to find the ideal shapes with several prescribed stress ratios between the machine direction (MD) or long direction and transverse direction (TD) or short direction. Second, the cutting pattern analysis based on the mathematical approach produces the drape strips which correspond to the shape obtained from form finding. Specially, the plane strips, which are not draped, will be used for the middle parts of some specimens. Third, those strips are connected by weld lines into the specimens, and the boundaries of those specimens are drawn to introduce the tension.

Compared to the traditional method of section *1.1.1*, the advantages of proposed fabrication method are: (1) only a few of weld lines are necessary; (2) the compensation or optimization of

drape strips is not necessary. However, the problem in proposed fabrication method is that the values of drawing boundary must be determined by the absence of wrinkling and the sufficient pre-stress. When the boundary is drawn, the film slides on the supporting frames such as arches. This slide must be considered to determine the values of drawing boundary, because it affects to the distribution of prestress on the film and the occurrence of wrinkling. Therefore, both analytical and experimental methods are essential to investigate the slide or friction contact between ETFE film and supporting frames.

1.1.4. Previous works on analysis of membrane structure considering friction contact

(a) The computational contact mechanics has attracted a great number of researchers. Generally, the contact conditions can be divided into normal contact conditions and friction contact conditions. The normal contact conditions prevent the slave body from penetrating into the master body, while the friction contact conditions represent the frictional behavior on the contact surface [NK15]. Figure 1.6 shows the two elastic bodies come into contact.

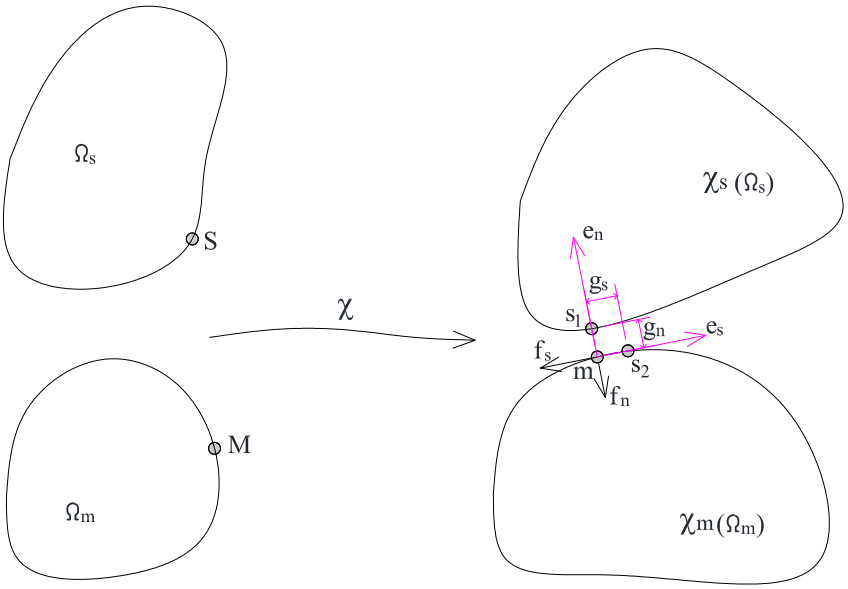

Figure 1.6 Contact conditions in two dimensions

Assuming that the motion χ brings the points *S* and *M* of the slave and master bodies, respectively come into contact. Once the contact point is found, the distance g_n between two points $\mathrm{m} = \chi(\mathrm{M})$ and $s_1 = \chi(\mathrm{S})$ has to be checked to determine whether the normal contact occurs or not. The constraint conditions for this case are presented in Kuhn-Tucker equation as shown in Eq. (1.1)

$$g_n \geq 0, \quad f_n \leq 0, \quad g_n f_n = 0 \tag{1.1}$$

When the normal contact occurs, the motion of slave point s_1 on master body can be

divided into two different actions. In the first, no tangential relative displacement occurs under a friction force f_s. This behavior is called stick. The second action, which denotes the so-called slip, dues to the force f_s is associated with a relative tangential movement g_s. The constraint conditions, which satisfy the dry friction Coulomb theory, for this period is represented in Eq. (1.2)

$$g_s \geq 0, \quad f_s - \mu f_n \leq 0, \quad g_s(f_s - \mu f_n) = 0 \tag{1.2}$$

where, μ is static friction coefficient between two body surfaces.

There are two basis constraint methods, the Lagrange multiplier method and the penalty method, can be used to impose above contact constraints conditions. In the Lagrange multiplier method, the contact forces are taken as primary unknowns, and the non-penetration condition is enforced exactly *[NK88, KB84]*. In the penalty method, penetration between two contacting boundaries is introduced, and the contact forces are related to the penetration by a penalty parameter *[JS86, SL93, DP92, SJ99]*. The two basic constraint methods can be combined into so-called augmented Lagrange method *[JO81]*.

(b) The membrane structure tends to adapt by undergoing large deflections under specified loads, so the analysis of membrane structure must consider the geometrical nonlinearity. In terms of contact analysis for membrane structures, Haber *[RH83, RH84]* suggested the Arbitrary Lagrangian-Eulerian (ALE) method to overcome the large deformation and contact problems. In this method, the Lagrangian displacements define the overall change in geometry of the structure, while the Eulerian terms describe the motion of the node points through the structural continuum due to slip. However, the linear elastic material and the theoretical choice of reference configuration were the limit points in this method. Noguchi *[HN01, HN04]* also suggested the combination between ALE method and meshfree method to overcome these problems. Again, the elastic-plastic material properties were ignored in his research. Sakai *[HS95]* proposed the energy minimization procedure for foldable membrane element to solve the problems of non-linear geometric and contact conditions. The limitation of his method was still the elastic range of material. The method of equivalent side tension of triangular element for foldable membrane element to solve the problem of non-linear geometric and contact conditions was reported by Ishida *[MI99]*. This method, however, was hardly applied in the existing FEM program.

(c) Generally, two types of nonlinearity, which are the geometrical nonlinearity and the material nonlinearity, exist in the solution of general contact problems. The incremental solution procedure is usually used to obtain the solution of these problems. It is important to observe that there is no guarantee that this procedure will always convergence *[ZZ92]*. As a result, when the shape of membrane structure is complicated, and the friction contact conditions is considered, the solutions for these problems are hardly obtained due to the convergence criteria.

1.2 Purpose of this thesis

The first purpose of this thesis is to develop the analytical method, which considers the geometrical nonlinearity, the material nonlinearity and the nonlinearity of friction contact conditions, for predicting the behavior of ETFE film and evaluating the effect of friction contact during the introduced prestress stage in tensile membrane structures. The elastic-plastic properties of ETFE film and the friction characteristics of contact surfaces are determined during the static loading process in this method. Within this work, while the static friction coefficient between ETFE film and steel pipes is carried out by the element experiments, the effect of friction contact on stress distribution of ETFE film is investigated by both this analytical method and the stretch fabrication experiments. The accuracy and applicability of the suggested analytical method are confirmed by both the experiments and the existing commercial software *ANSYS* [AN07].

The second purpose of this thesis is to check the possibility of fabrication of smooth three-dimensional (3D) curved surface using ETFE film by drawing plane and/or drape types of cutting strips. In this fabricate technique: (a) the form finding and cutting pattern analyses are carried out to find several types of cutting strips; (b) the proposed analytical method predicts the values of drawing boundary considering the friction between ETFE film and galvanized steel arches; (c) the stretch fabrication experiments are carried out to confirm the technique.

The purpose and flow chart of this thesis are presented in Figure 1.7

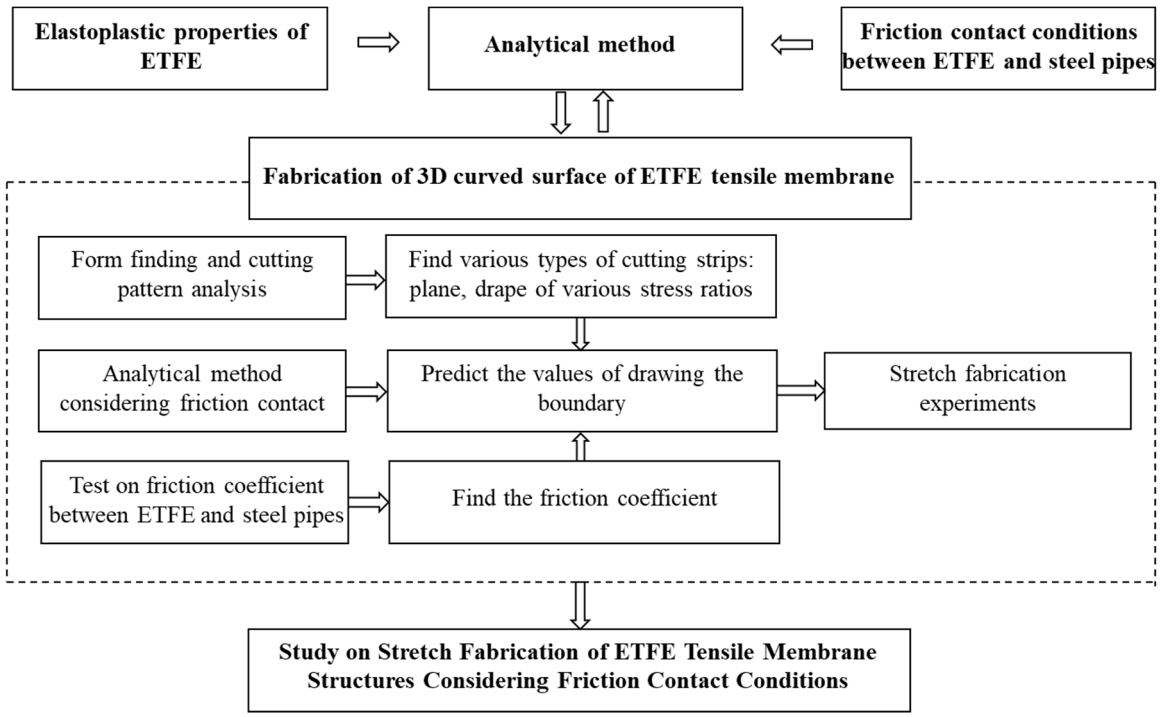

Figure 1.7 Purpose and flow chart of this thesis

1.3 Organization of this thesis

This thesis comprises six chapters which are described in Figure 1.8.

Chapter 1, "*Introduction*", presents the proposed stretch fabrication method and its problems for establishing the smooth curved surface of tensile membrane structures using ETFE film. The motivation, the background and the purposes of this thesis are also indicated in this chapter.

Chapter 2, "*Review on form finding and cutting pattern analysis*", describes a review on the form finding and cutting pattern analysis for tensile membrane structures. The saddle type of tensile membrane structure is investigated in this chapter. This structure comprises the outside frame, two supporting arches and ETFE film. The part of the film between two arches is called middle part, while the part between arch and outside frame is called corner part. First, the form finding analysis is carried out with several prescribed stress ratios between machine direction (MD) and transverse direction (TD) for both middle and corner parts. Second, the cutting pattern analysis based on the mathematical approach produces the drape strips which correspond to the shapes obtained from form finding. The effectiveness of weld and drawing works of those drape strips is also discussed in this chapter.

Chapter 3, "*Fabrication of three-dimensional (3D) curved surface using ETFE film by stretching plane strips*", presents the stretch fabrication experiments on the establishment of 3D curved surface of saddle type membrane structures using ETFE film by stretching the combination of plane strips, which was not draped, for the middle part and drape strips for the corner parts. The possibility of fabrication of low-rise 3D curved surface is confirmed, while the establishment of high-rise 3D smooth curved surface by drawing the plane strips still has problems because of the occurrence of wrinkling and insufficient prestress. The measurement method for pre-tensile strains and prestresses on ETFE film is also presented. In addition, the slide between ETFE film and the supporting galvanized steel arch is investigated.

Chapter 4, "*Total Lagrangian formulation for ETFE tensile membrane structure considering friction contact*", introduces the total Lagrangian formulations for both triangular membrane element and node-to-node contact element. The analytical procedure, which uses these elements, is suggested to solve the geometrical nonlinearity problem, the material nonlinearity problem and the nonlinearity problem of friction contact conditions. The suggested analytical method is in high agreement with commercial software ANSYS for the frictionless case. Moreover, this method indicates the effectiveness for friction contact case too. The results of the experiments in Chapter 3 partially confirm the suggested analytical method for the 0.3 of static friction coefficient between ETFE film and galvanized steel arch.

Chapter 5, "*Fabrication of three-dimensional (3D) ETFE curved surface by stretching drape strips considering friction contact*", shows the stretch fabrication technique on the establishment of 3D curved surface of saddle type of ETFE tensile membrane structures

considering the friction contact conditions. First, a test on static friction coefficient between ETFE film and steel pipes, which are black and galvanized types, is proposed. Second, the cutting pattern strips or drape strips, which are obtained in Chapter 2, are used to make the specimens. Third, the analytical method of Chapter 4 predicts the values of drawing boundary. This prediction will guarantee the absence of wrinkling and the sufficiency of introduced prestress. Finally, the stretch fabrication experiments will be carried out. The establishment of high-rise 3D smooth curved surface by drawing the drape strips for both middle and corner parts is confirmed by this fabrication technique. In addition, the pressurization test is carried out to confirm the strength of the structure after above construction stage.

Chapter 6, "*Conclusion*", describes a summary of suggested analytical method and its application on stretch fabrication method for saddle type of tensile membrane structure using ETFE film. The thesis concludes with a discussion, how and to which extent, the tools and results obtained can be used for the design and the construction of ETFE tensile membrane structure.

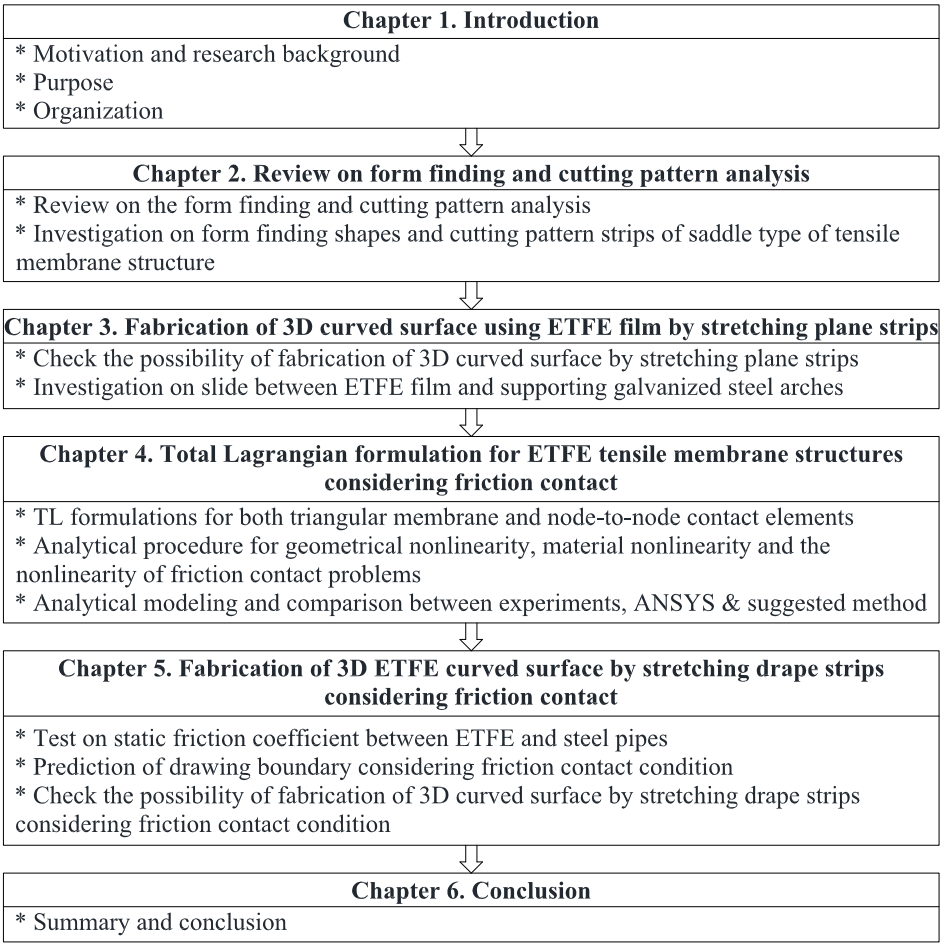

Figure 1.8 Organization of this thesis

Chapter 2.
Review on form finding and cutting pattern analysis

Chapter 2. Review on form finding and cutting pattern analysis

2.1 Introduction

Two important steps in the design of tensile membrane structures are form finding and cutting pattern. While the form finding is defined as "*finding a shape of equilibrium of forces in a given boundary with respect to a certain stress state*" [DV12], the cutting pattern is determined as "*finding the shape of fabric strips, in a plane, which when joined together will take the desired shape*" [BT93], [KI99]. This chapter introduces a review of the form finding and cutting pattern analysis for tensile membrane structures. In addition, the saddle type of tensile membrane structure is investigated. This structure comprises the outside frame, two supporting arches and ETFE film. The part of the film between two arches is called middle part, while the part between arch and outside frame is called corner part. First, the form finding analysis is carried out with several prescribed stress ratios between machine direction (*MD*) and transverse direction (*TD*) for both middle and corner parts. Second, the cutting pattern analysis based on the mathematical approach produces the drape strips which correspond to the shapes obtained from form finding. The effectiveness of weld and drawing works of those drape strips is also discussed in this chapter.

2.2 Form finding analysis

2.2.1. Methods in form finding analysis

Generally, the form finding method can be divided into three main approaches as stiffness matrix method, geometric stiffness method and dynamic equilibrium method [DV12], [KI89]. First, the stiffness matrix methods are based on using the standard elastic and geometric stiffness matrices. These methods are among the oldest form finding methods and are adapted from structural analysis. If a very small Young modulus of material is assumed, the isotropic stress surface can be obtained by this method [JA74], [BT92]. Second, the geometric stiffness methods are material independent, with only a geometric stiffness. The force density method is a representative method of those methods [RH82], [KB99], [RP08]. Third, the dynamic equilibrium methods solve the problem of dynamic equilibrium to arrive at a steady-state solution, equivalent to the static solution of static equilibrium [MB88], [MB99]. Each method has an advantage and disadvantage points. The common criticisms for each method can be found in the works of Veenendaal [DV12].

The next section makes a review of the formulations for triangular membrane element according to the stiffness matrix methods, which can be used in form finding procedure of

tensile membrane structures. A tool, which is named as *FF*, is developed and added to the existing *FEM* program to investigate the ideal shapes of saddle type of membrane structures with several stress ratios between MD and TD directions.

2.2.2. Isotropic stress surface approach

The triangular membrane element will be used in this section. The motions of these elements from the initial shape to the final shape are described in Figure 2.1.

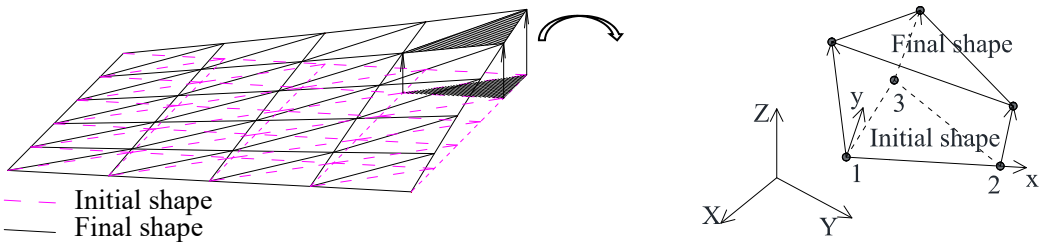

a. Sample of form finding *b. Local and global coordinates*

Figure 2.1 The motion of triangular membrane element in form finding procedure

The triangular membrane element has three nodes and nine degrees of freedom per element. The local coordinate of each element is determined as shown in Figure 2.1b. The coordinates of the initial shape and final shape, the displacements from the initial shape to the final shape are denoted in Eq. (2.1)

$_0x_i,\ _0y_i,\ _0z_i$: the local coordinates of node *i (i=1→3)* in the initial shape
x_i, y_i, z_i : the local coordinates of node *i (i=1→3)* in the final shape
u_i, v_i, w_i : the displacements of node *i (i=1→3)* in *x, y, z* axes, respectively
u, v, w : the displacements in element in *x, y, z* axes, respectively (2.1)

Assuming that the displacements u, v and w are linear over the element, the equation Eq. (2.2) can be obtained

$$\begin{aligned} u &= a_1 + a_2x + a_3y \\ v &= a_4 + a_5x + a_6y \\ w &= a_7 + a_8x + a_9y \end{aligned} \tag{2.2}$$

Evaluating the displacements at three nodes of element, and solving for a_i, the Eq. (2.3) can be determined as

$$\begin{aligned} a_2 &= (\ _0y_{23}u_1 + \ _0y_{31}u_2 + \ _0y_{12}u_3)/2S_0 \\ a_3 &= (\ _0x_{32}u_1 + \ _0x_{13}u_2 + \ _0x_{21}u_3)/2S_0 \\ a_5 &= (\ _0y_{23}v_1 + \ _0y_{31}v_2 + \ _0y_{12}v_3)/2S_0 \\ a_6 &= (\ _0x_{32}w_1 + \ _0x_{13}w_2 + \ _0x_{21}w_3)/2S_0 \\ a_8 &= (\ _0y_{23}w_1 + \ _0y_{31}w_2 + \ _0y_{12}w_3)/2S_0 \end{aligned} \tag{2.3}$$

$$a_9 = \left({}_0x_{32}w_1 + {}_0x_{13}w_2 + {}_0x_{21}w_3 \right)/2S_0$$

where, the values of ${}_0y_{ij}$, ${}_0x_{ij}$ and S_0 are calculated in Eq. (2.4)

$$\begin{aligned} {}_0x_{ij} &= {}_0x_i - {}_0x_j \\ {}_0y_{ij} &= {}_0y_i - {}_0y_j \\ 2S_0 &= \begin{vmatrix} 1 & {}_0x_1 & {}_0y_1 \\ 1 & {}_0x_2 & {}_0y_2 \\ 1 & {}_0x_3 & {}_0y_3 \end{vmatrix} \end{aligned} \tag{2.4}$$

The Green-Lagrange strains of the deformation from initial shape to the final shape are determined in equation Eq. (2.5)

$$\begin{aligned} \varepsilon_{xx} &= \frac{\partial u}{\partial x} + \frac{1}{2}\left[\left(\frac{\partial u}{\partial x}\right)^2 + \left(\frac{\partial v}{\partial x}\right)^2 + \left(\frac{\partial w}{\partial x}\right)^2\right] \\ \varepsilon_{yy} &= \frac{\partial v}{\partial y} + \frac{1}{2}\left[\left(\frac{\partial u}{\partial y}\right)^2 + \left(\frac{\partial v}{\partial y}\right)^2 + \left(\frac{\partial w}{\partial y}\right)^2\right] \\ \varepsilon_{xy} &= \frac{\partial u}{\partial y} + \frac{\partial v}{\partial x} + \left[\frac{\partial u}{\partial x}\frac{\partial u}{\partial y} + \frac{\partial v}{\partial x}\frac{\partial v}{\partial y} + \frac{\partial w}{\partial x}\frac{\partial w}{\partial y}\right] \end{aligned} \tag{2.5}$$

Substituting equation Eq. (2.2) into Eq. (2.5), and writing them in matrix form, Eq. (2.6) can be obtained

$$\boldsymbol{\varepsilon} = \begin{Bmatrix} \varepsilon_{xx} \\ \varepsilon_{yy} \\ \varepsilon_{xy} \end{Bmatrix} = \begin{Bmatrix} a_2 + 0.5({a_2}^2 + {a_5}^2 + {a_8}^2) \\ a_6 + 0.5({a_3}^2 + {a_6}^2 + {a_9}^2) \\ a_3 + a_5 + (a_2a_3 + a_5a_6 + a_8a_9) \end{Bmatrix} \tag{2.6}$$

The variations of these strains can be determined in Eq. (2.7)

$$\begin{aligned} \delta\boldsymbol{\varepsilon} &= \begin{Bmatrix} \delta\varepsilon_{xx} \\ \delta\varepsilon_{yy} \\ \delta\varepsilon_{xy} \end{Bmatrix} \\ &= \begin{Bmatrix} \delta a_2 + (\delta a_2 a_2 + \delta a_5 a_5 + \delta a_8 a_8) \\ \delta a_6 + (\delta a_3 a_3 + \delta a_6 a_6 + \delta a_9 a_9) \\ \delta a_3 + \delta a_5 + (a_2\delta a_3 + \delta a_2 a_3 + \delta a_5 a_6 + a_5\delta a_6 + \delta a_8 a_9 + a_8\delta a_9) \end{Bmatrix} \end{aligned} \tag{2.7}$$

Substituting equation Eq. (2.3) into Eq. (2.7), and writing them in matrix form, Eq. (2.8) can be obtained

$$\delta\boldsymbol{\varepsilon} = \begin{Bmatrix} \delta\varepsilon_{xx} \\ \delta\varepsilon_{yy} \\ \delta\varepsilon_{xy} \end{Bmatrix} = (\boldsymbol{B}_0 + \boldsymbol{B}_L) \cdot \delta\boldsymbol{u} \tag{2.8}$$

where, the values of $\boldsymbol{B}_0$, $\boldsymbol{B}_L$ and $\delta\boldsymbol{u}$ are calculated in Eq. (2.9)

$$\boldsymbol{B}_0 = \frac{1}{2S_0}\begin{bmatrix} {}_0y_{23} & 0 & 0 & {}_0y_{31} & 0 & 0 & {}_0y_{12} & 0 & 0 \\ 0 & {}_0x_{32} & 0 & 0 & {}_0x_{13} & 0 & 0 & {}_0x_{21} & 0 \\ {}_0x_{32} & {}_0y_{23} & 0 & {}_0x_{13} & {}_0y_{31} & 0 & {}_0x_{21} & {}_0y_{12} & 0 \end{bmatrix} \tag{2.9a}$$

$$\boldsymbol{B}_L = \frac{1}{2S_0}\begin{bmatrix} a_{2\ 0}y_{23} & a_{5\ 0}y_{23} & a_{8\ 0}y_{23} & a_{2\ 0}y_{31} & a_{5\ 0}y_{31} & a_{8\ 0}y_{31} & a_{2\ 0}y_{12} & a_{5\ 0}y_{12} & a_{8\ 0}y_{12} \\ a_{3\ 0}x_{32} & a_{6\ 0}x_{32} & a_{9\ 0}x_{32} & a_{3\ 0}x_{13} & a_{6\ 0}x_{13} & a_{9\ 0}x_{13} & a_{3\ 0}x_{21} & a_{6\ 0}x_{21} & a_{9\ 0}x_{21} \\ a_{3\ 0}y_{23} & a_{6\ 0}y_{23} & a_{9\ 0}y_{23} & a_{3\ 0}y_{31} & a_{6\ 0}y_{31} & a_{9\ 0}y_{31} & a_{3\ 0}y_{12} & a_{6\ 0}y_{12} & a_{9\ 0}y_{12} \\ +a_{2\ 0}x_{32} & +a_{5\ 0}x_{32} & +a_{8\ 0}x_{32} & +a_{2\ 0}x_{13} & +a_{5\ 0}x_{13} & +a_{8\ 0}x_{13} & +a_{2\ 0}x_{21} & +a_{5\ 0}x_{21} & +a_{8\ 0}x_{21} \end{bmatrix} \tag{2.9b}$$

$$\delta\boldsymbol{u} = [\delta u_1 \quad \delta v_1 \quad \delta w_1 \quad \delta u_2 \quad \delta v_2 \quad \delta w_2 \quad \delta u_3 \quad \delta v_3 \quad \delta w_3]^T \tag{2.9c}$$

The equilibrium equations for a single element in local coordinate system can be obtained via the principle of virtual work as shown in Eq. (2.10)

$$\int_{V_0} \delta\boldsymbol{\varepsilon}^T \cdot \boldsymbol{\sigma} dV - \delta\boldsymbol{u}^T \cdot \boldsymbol{p} = 0 \tag{2.10}$$

where, V_0 denotes the element volume of initial shape, and $\boldsymbol{p}$ is the external nodal force vector in local coordinate.

In the form finding process of tensile membrane structures, the forced displacement conditions are usually used at the boundary to obtain the solutions, so the external nodal force vector can be ignored. The constitutive relations for linear elastic plane stress analysis under the large displacements and small strains conditions may be used as shown in Eq. (2.11)

$$\boldsymbol{\sigma} = \begin{Bmatrix} \sigma_{xx} \\ \sigma_{yy} \\ \sigma_{xy} \end{Bmatrix} = \boldsymbol{D} \cdot \boldsymbol{\varepsilon} + \boldsymbol{\sigma}_0 = \boldsymbol{D} \cdot \boldsymbol{\varepsilon} + \begin{Bmatrix} \sigma_{x0} \\ \sigma_{y0} \\ 0 \end{Bmatrix} \tag{2.11}$$

where, $\boldsymbol{D}$ is material elastic tensor, and $\boldsymbol{\sigma}_0$ is the initial stress vector.

In isotropic stress surface approach, it is assumed that the membrane has a very small Young's modulus, so the stresses in the membrane will change very slightly even though large deformations are included. As a result, the stresses in the membrane are almost depended on the initial stress vector. Eq. (2.11) can be rewritten as shown in Eq. (2.12)

$$\boldsymbol{\sigma} = \boldsymbol{\sigma}_0 = \begin{Bmatrix} \sigma_{x0} \\ \sigma_{y0} \\ 0 \end{Bmatrix} \tag{2.12}$$

Substituting equation Eq. (2.8) and Eq. (2.12) into Eq. (2.10), Eq. (2.13) can be obtained

$$\int_{V_0} \delta\boldsymbol{u}^T \cdot (\boldsymbol{B}_0 + \boldsymbol{B}_L)^T \cdot \boldsymbol{\sigma}_0 dV = 0 \tag{2.13}$$

Eliminating the variation vector $\delta\boldsymbol{u}^T$, the equation Eq. (2.13) can be rewritten in Eq. (2.14)

$$\int_{V_0} (\boldsymbol{B}_0 + \boldsymbol{B}_L)^T \cdot \boldsymbol{\sigma}_0 dV = 0 \tag{2.14}$$

The Newton-Raphson method can be used to obtain the solution of Eq. (2.14). The residual term after the *ith* iteration of Eq. (2.14) is determined in Eq. (2.15)

$$\boldsymbol{\Phi}^{(i)} = \int_{V_0} \left(\boldsymbol{B}_0 + \boldsymbol{B}_L^{(i)}\right)^T \cdot \boldsymbol{\sigma}_0 dV \tag{2.15}$$

For the next step which is expected to yield the exact solution, the equation Eq. (2.16) can be obtained

$$\begin{aligned} \boldsymbol{\Phi}^{(i+1)} &= \boldsymbol{\Phi}^{(i)} + \frac{\partial \boldsymbol{\Phi}^{(i)}}{\partial \boldsymbol{u}} \Delta \boldsymbol{u}^{(i)} = 0 \\ \frac{\partial \boldsymbol{\Phi}^{(i)}}{\partial \boldsymbol{u}} \Delta \boldsymbol{u}^{(i)} &= -\boldsymbol{\Phi}^{(i)} \end{aligned} \tag{2.16}$$

The solution of $\Delta \boldsymbol{u}^{(i)}$ can be obtained by Eq. (2.16). The displacement nodal vector and the coordinate nodal vector at step *(i+1)* can be determined by Eq. (2.17)

$$\begin{aligned} \boldsymbol{u}^{(i+1)} &= \boldsymbol{u}^{(i)} + \Delta \boldsymbol{u}^{(i)} \\ \boldsymbol{x}^{(i+1)} &= {}_0\boldsymbol{x} + \boldsymbol{u}^{(i+1)} \end{aligned} \tag{2.17}$$

where, ${}_0\boldsymbol{x}$ and $\boldsymbol{x}^{(i+1)}$ are the coordinate nodal vectors of the initial shape and the shape of step *(i+1)*, respectively. Eq. (2.18) represents the determination of these vectors.

$$\begin{aligned} {}_0\boldsymbol{x} &= \begin{bmatrix} {}_0x_1 & {}_0y_1 & {}_0z_1 & {}_0x_2 & {}_0y_2 & {}_0z_2 & {}_0x_3 & {}_0y_3 & {}_0z_3 \end{bmatrix}^{\mathrm{T}} \\ \boldsymbol{x}^{(i+1)} &= \begin{bmatrix} x_1^{(i+1)} & y_1^{(i+1)} & z_1^{(i+1)} & x_2^{(i+1)} & y_2^{(i+1)} & z_2^{(i+1)} & x_3^{(i+1)} & y_3^{(i+1)} & z_3^{(i+1)} \end{bmatrix}^{\mathrm{T}} \end{aligned} \tag{2.18}$$

This process is repeated until the incremental nodal displacement vector $\Delta \boldsymbol{u}^{(i)}$ satisfies the convergence criteria. The derivation of $\frac{\partial \boldsymbol{\Phi}^{(i)}}{\partial \boldsymbol{u}}$ of Eq. (2.16) is shown in Eq. (2.19)

$$\frac{\partial \boldsymbol{\Phi}^{(i)}}{\partial \boldsymbol{u}} = \int_{V_0} \frac{\partial \left(\boldsymbol{B}_L^{(i)} \right)^T}{\partial \boldsymbol{u}} \cdot \boldsymbol{\sigma}_0 dV = \boldsymbol{k}_{mx} + \boldsymbol{k}_{my} \tag{2.19}$$

where, $\boldsymbol{k}_{mx}$ and $\boldsymbol{k}_{my}$ are defined in Eq. (2.20)

$$\boldsymbol{k}_{mx} = \frac{h \cdot \sigma_{x0}}{4S_0} \begin{bmatrix} {}_0y_{23}{}^2 & 0 & 0 & {}_0y_{23}\,{}_0y_{31} & 0 & 0 & {}_0y_{23}\,{}_0y_{12} & 0 & 0 \\ & {}_0y_{23}{}^2 & 0 & 0 & {}_0y_{23}\,{}_0y_{31} & 0 & 0 & {}_0y_{23}\,{}_0y_{12} & 0 \\ & & {}_0y_{23}{}^2 & 0 & 0 & {}_0y_{23}\,{}_0y_{31} & 0 & 0 & {}_0y_{23}\,{}_0y_{12} \\ & & & {}_0y_{31}{}^2 & 0 & 0 & {}_0y_{31}\,{}_0y_{12} & 0 & 0 \\ & & & & {}_0y_{31}{}^2 & 0 & 0 & {}_0y_{31}\,{}_0y_{12} & 0 \\ & & & & & {}_0y_{31}{}^2 & 0 & 0 & {}_0y_{31}\,{}_0y_{12} \\ & & sym & & & & {}_0y_{12}{}^2 & 0 & 0 \\ & & & & & & & {}_0y_{12}{}^2 & 0 \\ & & & & & & & & {}_0y_{12}{}^2 \end{bmatrix}$$

$$\boldsymbol{k}_{my} = \frac{h \cdot \sigma_{y0}}{4S_0} \begin{bmatrix} {}_0x_{32}{}^2 & 0 & 0 & {}_0x_{32}\,{}_0x_{13} & 0 & 0 & {}_0x_{32}\,{}_0x_{21} & 0 & 0 \\ & {}_0x_{32}{}^2 & 0 & 0 & {}_0x_{32}\,{}_0x_{13} & 0 & 0 & {}_0x_{32}\,{}_0x_{21} & 0 \\ & & {}_0x_{32}{}^2 & 0 & 0 & {}_0x_{32}\,{}_0x_{13} & 0 & 0 & {}_0x_{32}\,{}_0x_{21} \\ & & & {}_0x_{13}{}^2 & 0 & 0 & {}_0x_{13}\,{}_0x_{21} & 0 & 0 \\ & & & & {}_0x_{13}{}^2 & 0 & 0 & {}_0x_{13}\,{}_0x_{21} & 0 \\ & & & & & {}_0x_{13}{}^2 & 0 & 0 & {}_0x_{13}\,{}_0x_{21} \\ & & sym & & & & {}_0x_{21}{}^2 & 0 & 0 \\ & & & & & & & {}_0x_{21}{}^2 & 0 \\ & & & & & & & & {}_0x_{21}{}^2 \end{bmatrix} \tag{2.20}$$

where, h is the thickness of membrane, and S_0 is the area of the element at the initial shape.

It should be noted that the solution of Eq. (2.16) is carried out at element level. These equations must be transformed to the global coordinates and finally assembled to obtain the global equilibrium equations. The transformation matrix for triangular membrane element can be obtained in Eq. (2.21) [OZ05].

$$\boldsymbol{T} = \begin{bmatrix} \boldsymbol{T_e} & \boldsymbol{0} & \boldsymbol{0} \\ & \boldsymbol{T_e} & \boldsymbol{0} \\ sym & & \boldsymbol{T_e} \end{bmatrix}_{9x9}, \qquad \boldsymbol{T_e} = \begin{bmatrix} \boldsymbol{v}_{\bar{x}} \\ \boldsymbol{v}_{\bar{y}} \\ \boldsymbol{v}_{\bar{z}} \end{bmatrix}_{3x3}$$

$$\boldsymbol{v}_{\bar{x}} = \frac{1}{l_{21}}\begin{bmatrix} {}_0x_{21} & {}_0y_{21} & {}_0z_{21} \end{bmatrix}, \qquad l_{21} = \sqrt{{}_0x_{21}{}^2 + {}_0y_{21}{}^2 + {}_0z_{21}{}^2} \tag{2.21}$$

$$\boldsymbol{v}_{\bar{z}} = \frac{1}{2S_0}\begin{Bmatrix} {}_0y_{21}\,{}_0z_{31} - {}_0z_{21}\,{}_0y_{31} \\ {}_0z_{21}\,{}_0x_{31} - {}_0x_{21}\,{}_0z_{31} \\ {}_0x_{21}\,{}_0y_{31} - {}_0y_{21}\,{}_0x_{31} \end{Bmatrix}^T$$

$$\boldsymbol{v}_{\bar{y}} = \boldsymbol{v}_{\bar{z}} \times \boldsymbol{v}_{\bar{x}}$$

2.2.3. Procedure of the form finding tool *FF*

The procedure of the form finding tool *FF* is described in Figure 2.2. In this procedure, the convergence is checked at both residual forces and the increment of nodal displacements.

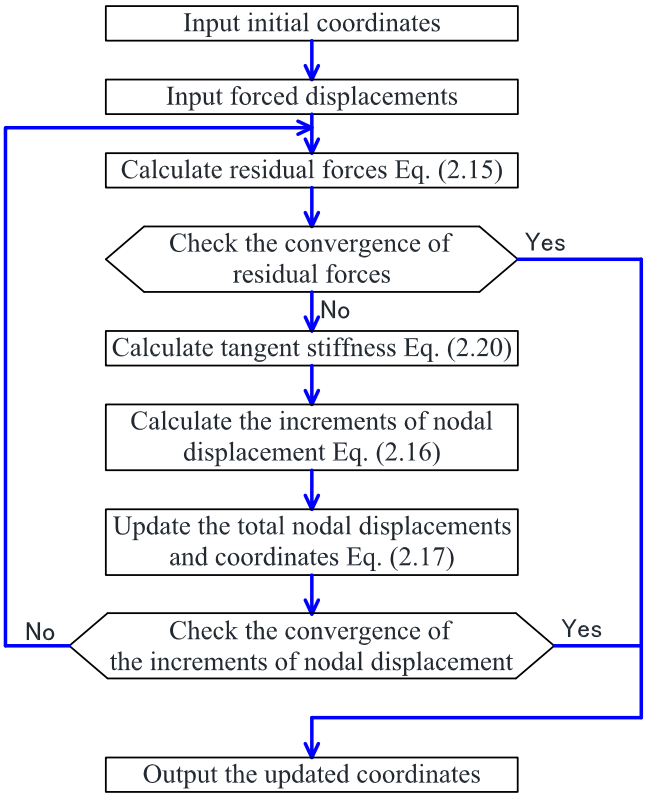

Figure 2.2 The procedure of the form finding tool FF

2.3 Cutting pattern analysis

2.3.1. Cutting pattern process

Generally, the cutting pattern involves three steps. First, the curved surface is divided into individual strips. In this step, the geodesic line, which will become a straight line upon the development of the curved surface, is utilized. The determination method of geodesic line on the curved surface can be referred in the method of Kazuo Ishii [KI99]. Second, the three-dimensional data for each strip are converted into usable plane form. This step is so-called the flattening step. Many research papers on this cutting pattern step have been reported [UH86], [NT93], [BM98], [TY98]. Third, the conversion or compensation step is necessary to optimize the cutting strips. The aim of the third step is to minimize the difference between the prescribed prestress state and the actual stress state. In this step, Tsubota introduced a new analytical method for producing a more accurate cutting pattern by utilizing an optimization technique [HT89], [HT93]. Ohsaki suggested shape-stress trade-off design method to optimize the cutting strips after moving the pretension force [MO00], while Linhard proposed the introducing the cutting patterns in form finding analysis to obtain the more accuracy cutting strips [JL08]. Generally, the third step took a number of work effort to obtain the accuracy of cutting strips. Even if the cutting strips are established with extreme accuracy, the discrepancy between the prescribed stress and actual stress states is still obvious because of the viscous characteristic of membrane material.

In the proposed fabrication method for establishing a smooth curved surface using ETFE film, the cutting strips which are established without the consideration of prestress, are obtained by flattening approach. After that, these strips will be joined together, and the ETFE film is drawn to its plastic region because of the increment of yield strength and the reduction of tension due to viscous characteristics. Therefore, the third step can be ignored in this method of fabrication. The flattening approach based on a least-squares minimization, which was suggested by Tabarrok [BT93], will be reviewed in this section. In addition, a tool, which is named as *CP*, is established according to this approach. This tool will be used to investigate the shapes of cutting strips of saddle type of membrane structures which correspond to the results of form finding analysis.

2.3.2. A least-squares minimization flattening approach

The process of a least-squares minimization flattening approach is presented in Figure 2.3. This method suggested the assumptions which are shown as below:

- ✧ The input three-dimensional data of nodes of each strip are obtained from the form finding analysis.
- ✧ The link element will connect two nodes in each side of triangular membrane element in form finding analysis.
- ✧ The boundary link elements will have the greater “weight” than that of the middle link

elements. This assumption will guarantee all cutting boundary lengths remain constant.

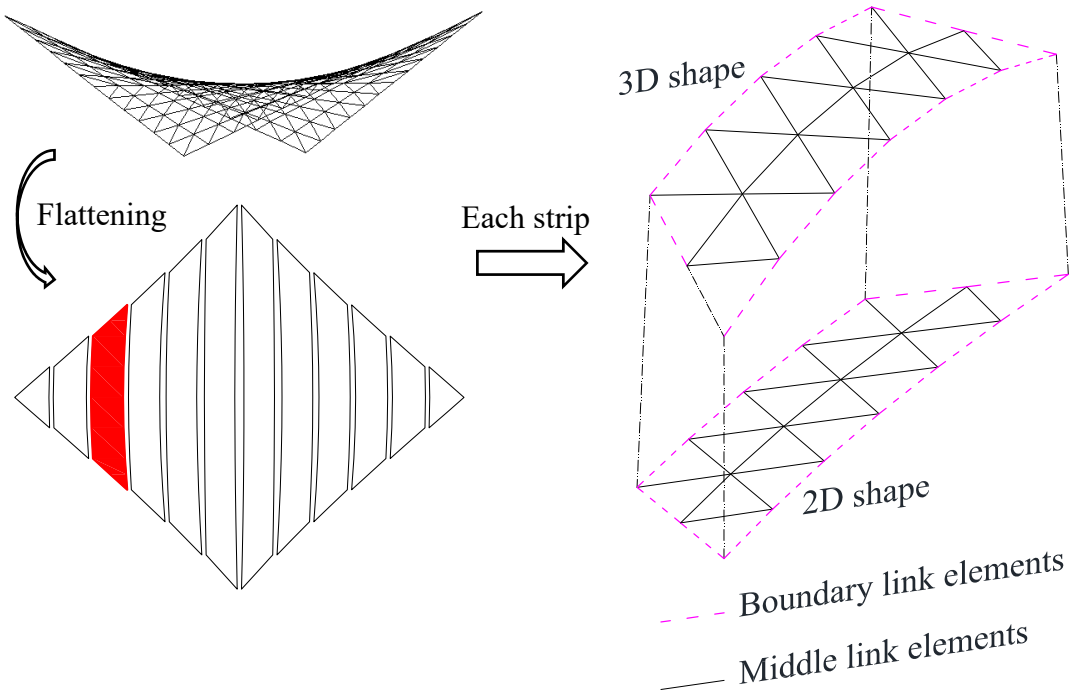

Figure 2.3 Process of a least-squares minimization method

The notations in this section are listed in Eq. (2.22)

$X_{i,1}, Y_{i,1}, Z_{i,1}$	The 3D coordinates of node *1* of link element *i*: known
$X_{i,2}, Y_{i,2}, Z_{i,2}$	The 3D coordinates of node *2* of link element *i*: known
$x_{i,1}, y_{i,1}$	The 2D coordinates of node *1* of link element *i*: unknown
$x_{i,2}, y_{i,2}$	The 2D coordinates of node *2* of link element *i*: unknown
x_j, y_j	The 2D coordinates of node *j*
m	The number of link elements in each strip
n	The number of nodes in each strip
$\emptyset_i$	The difference between the lengths in 2D and 3D of link element *i*
ω_i	The weight factor of link element *i*

(2.22)

The discrepancy between the general length of link elements in 3D coordinates and 2D coordinates is minimized by a least-squares approach as shown in Eq. (2.23)

$$\boldsymbol{S}(\boldsymbol{x}) = \sum_{i=1}^{m} \omega_i \, \emptyset_i^{\,2}(\mathbf{x}) \tag{2.23}$$

where, $\boldsymbol{x}$ is the coordinate vector of plane strip to be determined. The definitions of $\boldsymbol{x}$ and $\emptyset_i$

are shown in Eq. (2.24) and Eq. (2.25), respectively.

$$\boldsymbol{x} = [x_1 \quad y_1 \quad \dots \quad \dots \quad x_n \quad y_n] \tag{2.24}$$

$$\begin{aligned} \emptyset_i = &\sqrt{\left(x_{i,1} - x_{i,2}\right)^2 + \left(y_{i,1} - y_{i,2}\right)^2} \\ &- \sqrt{\left(X_{i,1} - X_{i,2}\right)^2 + \left(Y_{i,1} - Y_{i,2}\right)^2 + \left(Z_{i,1} - Z_{i,2}\right)^2} \end{aligned} \tag{2.25}$$

It should be noted that $\emptyset_i$ are the nonlinear functions of $\boldsymbol{x}$, so it is necessary to linearize $\emptyset_i$ in order to facilitate numerical calculation. Assuming an initial guess solution $\boldsymbol{x}_0$, the Taylor expansion of $\emptyset_i(\boldsymbol{x})$ can be obtained in Eq. (2.26) if the nonlinear terms are ignored.

$$\emptyset_i(\boldsymbol{x}) = \emptyset_i(\boldsymbol{x}_0) + \left.\frac{\partial \emptyset_i}{\partial \boldsymbol{x}}\right|_{\boldsymbol{x}_0} (\boldsymbol{x} - \boldsymbol{x}_0) \tag{2.26}$$

Substituting Eq. (2.26) into Eq. (2.23), Eq. (2.27) can be obtained

$$\boldsymbol{S}(\boldsymbol{x}) = \sum_{\mathrm{i}=1}^{\mathrm{m}} \omega_i \left[\emptyset_i(\boldsymbol{x}_0) + \left.\frac{\partial \emptyset_i}{\partial \boldsymbol{x}}\right|_{\boldsymbol{x}_0} (\boldsymbol{x} - \boldsymbol{x}_0)\right]^2 \tag{2.27}$$

The necessary condition for a minimum of $\boldsymbol{S}(\boldsymbol{x})$ is expressed in Eq. (2.28)

$$\frac{\partial \boldsymbol{S}(\boldsymbol{x})}{\partial \boldsymbol{x}} = 2\sum_{\mathrm{i}=1}^{\mathrm{m}} \omega_i \left[\emptyset_i(\boldsymbol{x}_0) + \left.\frac{\partial \emptyset_i}{\partial \boldsymbol{x}}\right|_{\boldsymbol{x}_0} (\boldsymbol{x} - \boldsymbol{x}_0)\right] \left.\frac{\partial \emptyset_i}{\partial \boldsymbol{x}}\right|_{\boldsymbol{x}_0} = 0 \tag{2.28}$$

The equation Eq. (2.28) can be written in matrix form as shown in Eq. (2.29)

$$\boldsymbol{A}^{\boldsymbol{T}}\boldsymbol{W}\boldsymbol{A}\Delta\boldsymbol{x} = -\boldsymbol{A}^{\boldsymbol{T}}\boldsymbol{W}\boldsymbol{C} \tag{2.29}$$

where, $\boldsymbol{A}$, $\boldsymbol{W}$ and $\boldsymbol{C}$ are defined in the equation Eq. (2.30)

$$\begin{aligned} \boldsymbol{A}(\boldsymbol{x}_0) &= \begin{bmatrix} \frac{\partial \emptyset_1}{\partial x_1} & \frac{\partial \emptyset_1}{\partial y_1} & \dots & \frac{\partial \emptyset_1}{\partial x_n} & \frac{\partial \emptyset_1}{\partial y_n} \\ \frac{\partial \emptyset_2}{\partial x_1} & \frac{\partial \emptyset_2}{\partial y_1} & \dots & \frac{\partial \emptyset_2}{\partial x_n} & \frac{\partial \emptyset_2}{\partial y_n} \\ \dots & \dots & \dots & \dots & \dots \\ \frac{\partial \emptyset_n}{\partial x_1} & \frac{\partial \emptyset_n}{\partial y_1} & \dots & \frac{\partial \emptyset_n}{\partial x_n} & \frac{\partial \emptyset_n}{\partial y_n} \end{bmatrix}_{mx2n} \\ \boldsymbol{W} &= \begin{bmatrix} \omega_1 & 0 & \dots & 0 \\ 0 & \omega_2 & \dots & 0 \\ \dots & \dots & \dots & \dots \\ 0 & 0 & \dots & \omega_m \end{bmatrix}_{mxm} \\ \boldsymbol{C}(\boldsymbol{x}_0) &= [\emptyset_1 \quad \emptyset_2 \quad \dots \quad \emptyset_n]_{mx1}{}^T \\ \Delta\boldsymbol{x} &= \boldsymbol{x} - \boldsymbol{x}_0 \end{aligned} \tag{2.30}$$

The solutions of Eq. (2.29) are the incremental of coordinates of plane nodes. The initial guess of solutions $\boldsymbol{x}_0$ will be added by those increments, and the process will be repeated until the convergence criteria are satisfied.

Eq. (2.29) can be written in the form which is similar to the finite element equation as shown in Eq. (2.31)

$$\boldsymbol{K}\Delta\boldsymbol{x} = \boldsymbol{R} \tag{2.31}$$

where, $\boldsymbol{K} = \boldsymbol{A}^{\boldsymbol{T}}\boldsymbol{W}\boldsymbol{A}$ is the "stiffness matrix", and $\boldsymbol{R} = -\boldsymbol{A}^{\boldsymbol{T}}\boldsymbol{W}\boldsymbol{C}$ is the "load matrix".

It is worth to note that a system of link elements is quite similar to a system of truss elements. Therefore, the matrices $\boldsymbol{K}$ and $\boldsymbol{R}$ can be obtained by assembling $\boldsymbol{K_i}$ and $\boldsymbol{R_i}$ of all link elements. The matrices $\boldsymbol{K_i}$ and $\boldsymbol{R_i}$ for link element *i* are determined in Eq. (2.32)

$$\boldsymbol{K_i} = \omega_i \boldsymbol{A_i}^T \boldsymbol{A_i} \tag{2.32a}$$

$$\boldsymbol{R_i} = -\omega_i \emptyset_i \boldsymbol{A_i}^T \tag{2.32b}$$

where, the matrix $\boldsymbol{A_i}$ is calculated in Eq. (2.33)

$$\boldsymbol{A_i} = \left[\frac{\partial \emptyset_i}{\partial x_{i,1}} \quad \frac{\partial \emptyset_i}{\partial y_{i,1}} \quad \frac{\partial \emptyset_i}{\partial x_{i,2}} \quad \frac{\partial \emptyset_i}{\partial x_{i,2}}\right] \tag{2.33a}$$

$$= \left[\frac{x_{i,1} - x_{i,2}}{l} \quad \frac{y_{i,1} - y_{i,2}}{l} \quad \frac{x_{i,2} - x_{i,1}}{l} \quad \frac{y_{i,2} - y_{i,1}}{l}\right]$$

$$l = \sqrt{\left(x_{i,1} - x_{i,2}\right)^2 + \left(y_{i,1} - y_{i,2}\right)^2} \tag{2.33b}$$

2.2.3. Procedure of the cutting pattern tool *CP*

The procedure of the cutting pattern tool *CP* is described in Figure 2.4.

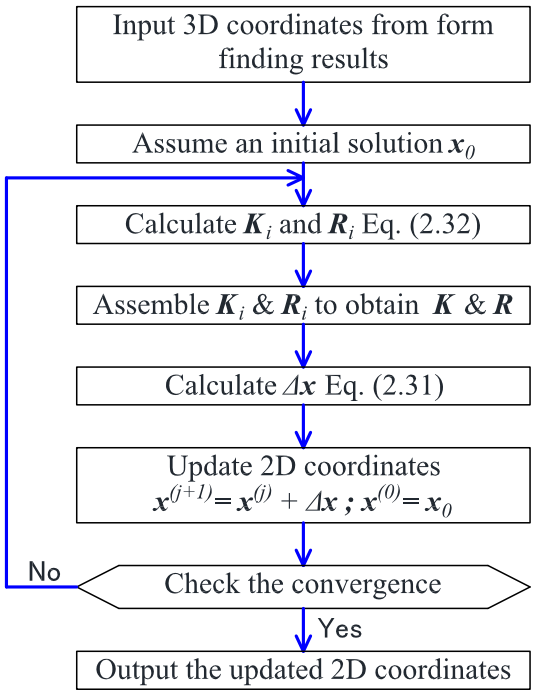

Figure 2.4 The procedure of the cutting pattern tool CP

2.4 Case study

2.4.1. Definition of case study

The saddle type of tensile membrane structure is investigated in this thesis. The dimensions and definitions of this structures are described in Figure 2.5. The film is fixed with the outside frames and is supported by two galvanized steel arches at the positions of arch. The long direction is named as machine direction or *MD* direction, while the short direction is named as transverse direction or *TD* direction.

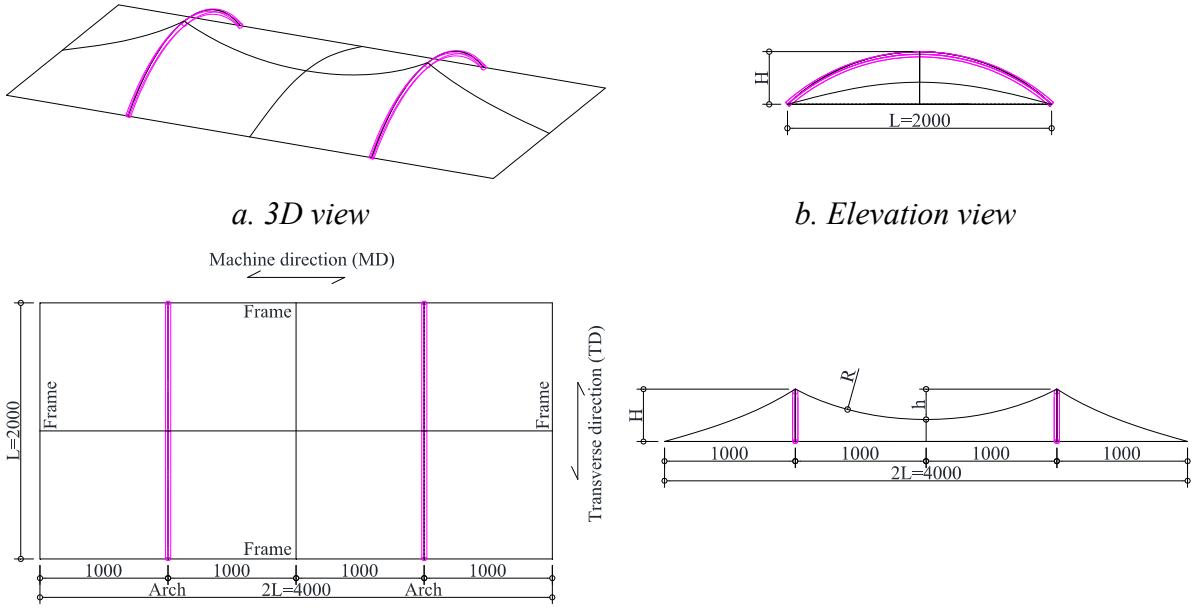

a. 3D view *b. Elevation view*

c. Plane view *d. Elevation view*

Figure 2.5 The dimensions and definitions of saddle tensile membrane structures (all dimensions are in millimeter)

The rise ratio r and the prescribed stress ratio s are defined in Eq. (2.34)

$$r = \frac{H}{L}, \qquad s = \frac{S_{MD}}{S_{TD}} \tag{2.34}$$

This section comprises six case studies which are categorized by the rise ratio and stress ratio as shown in Table 2.1.

Table 2.1 Definition of case study

	Case 1	**Case 2**	**Case 3**	**Case 4**	**Case 5**	**Case 6**
r	*10%*	*10%*	*15%*	*15%*	*20%*	*20%*
s	*1:1*	*3:1*	*1:1*	*3:1*	*1:1*	*3:1*

2.4.2. Models in form finding and cutting pattern analysis

A quarter of above structure is modeled in the form finding analysis. The boundary conditions and the forced displacement conditions are presented in Figure 2.6. The initial stresses in X and Y directions in Eq. (2.12) are chosen to satisfy the prescribed stress ratio in Table 2.1, while the forced displacement conditions at positions of arch are determined by the height of arch which is depended on the rise ratio.

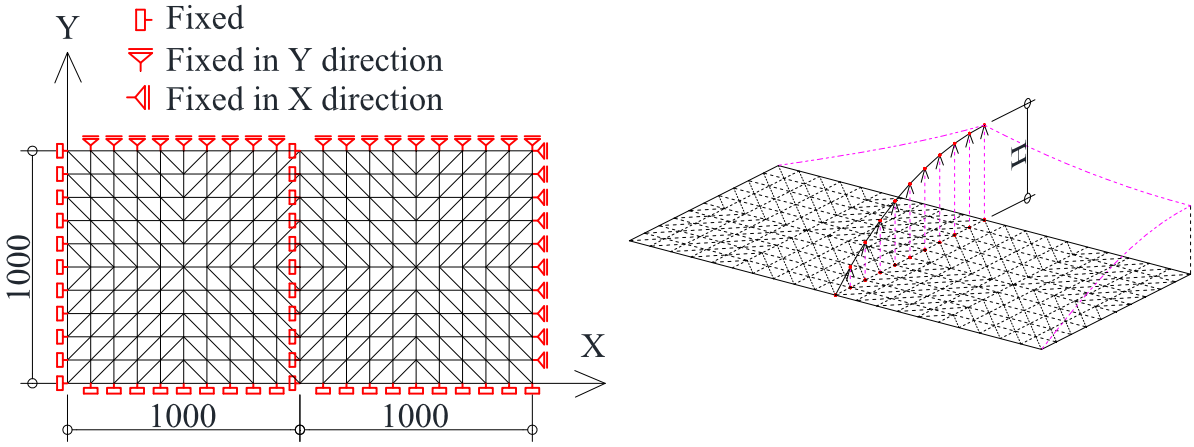

a. Boundary conditions *b. Forced displacement conditions*

Figure 2.6 A quarter model and essential boundary conditions in form finding analysis

The cutting lines and cutting strips are shown in Figure 2.7a. In the proposed method, a few of cutting lines are proposed, so there is only one cutting line which is chosen in the middle of this saddle membrane structure. The boundary link elements and middle link elements are indicated in Figure 2.7b&c. The weights of boundary link elements are chosen as 10^{12} unit as compared to *1* unit of the weights of middle link elements. Those selections are to guarantee that the lengths of boundary lines will remain constant during the cutting pattern analysis.

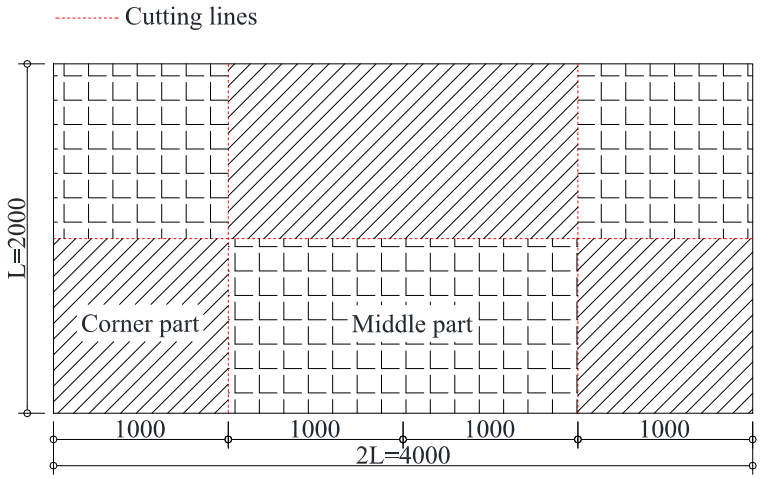

a. Cutting strips and cutting lines

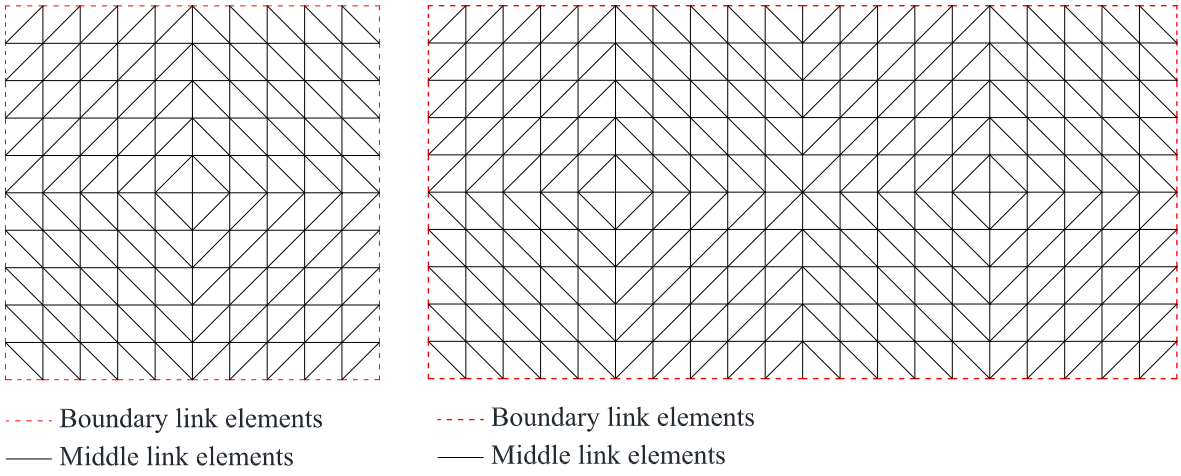

b. Link elements in corner part *c. Link elements in middle part*

Figure 2.7 Cutting strips and model of link elements for cutting pattern analysis

2.4.3. Results and discussions

The tool *FF* is used to obtain the ideal shapes of six case studies. The results are presented in Figure 2.8.

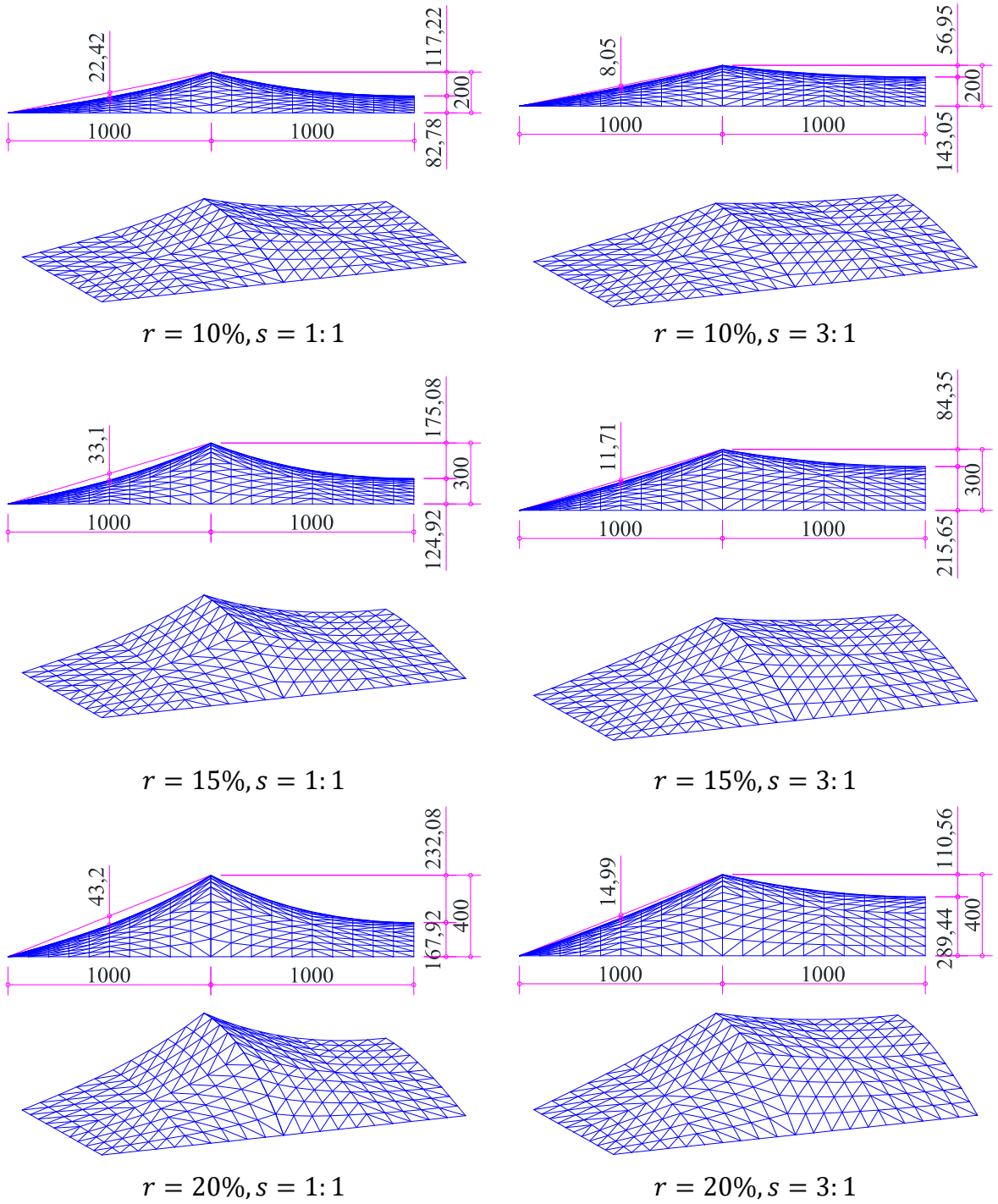

Figure 2.8 The form finding results
(All dimensions are in millimeter)

The curvature of the final curve of this saddle membrane structures in form finding analysis is defined in Eq. (2.35)

$$\kappa = \frac{1}{R} = \frac{8h}{L^2 + 4h} \tag{2.35}$$

where, h is the saddle height as shown in Figure 2.5d, L is short span of the structure.

Figure 2.9 shows the results of this curvature. The solid line with circle marker represents the results of prescribed stress ratio s of *1:1*, while the solid line with square marker indicates the results of *3:1* of s. According to Figure 2.9, when the rise ratio increases, the curvature of the final curve increases. The change of prescribed stress ratio from *1:1* to *3:1* can decrease the increments of the curvature.

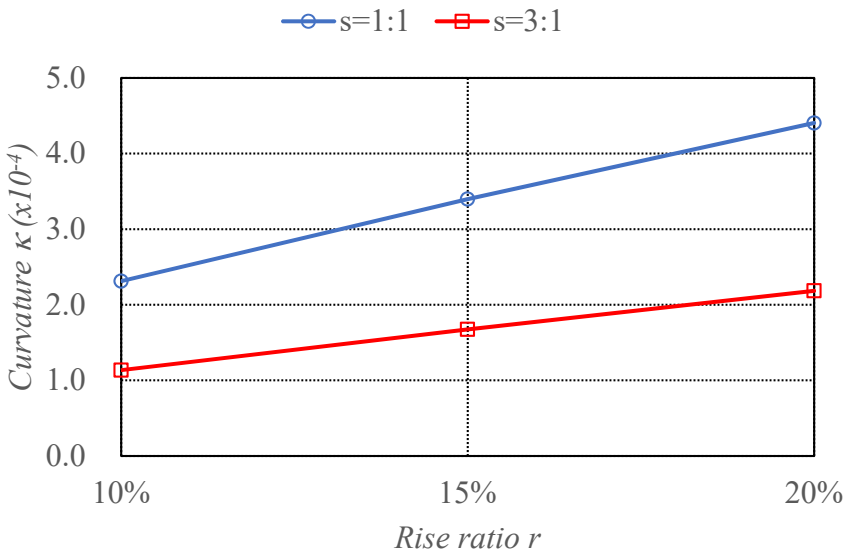

Figure 2.9 The curvature of the final curve in form finding analysis

The tool *CP* is used to obtain the cutting strips of corner and middle parts of six case studies. The results are presented in Figure 2.10. In Figure 2.10, the numbers show the lengths of boundary and cutting lines, while the percentage figures indicate the expansions of the lengths of drape strips and the corresponding lengths of the form finding shapes. It can be seen in Figure 2.10 that the increment of rise ratio makes the expansions increase. In the field of weld work, the increment of expansions will make the reduction of weld speed and the increasement of difficulty of connecting. The change of prescribed stress ratio from *1:1* to *3:1* can decrease those expansion. In addition, in the proposed fabrication method for establishing curved surface using ETFE film, we attempt to establish the curved surface from the non-tension state by stretching the composite of drape strips. Therefore, the effectiveness of selection of prescribed stress ratio should be checked by the experiments.

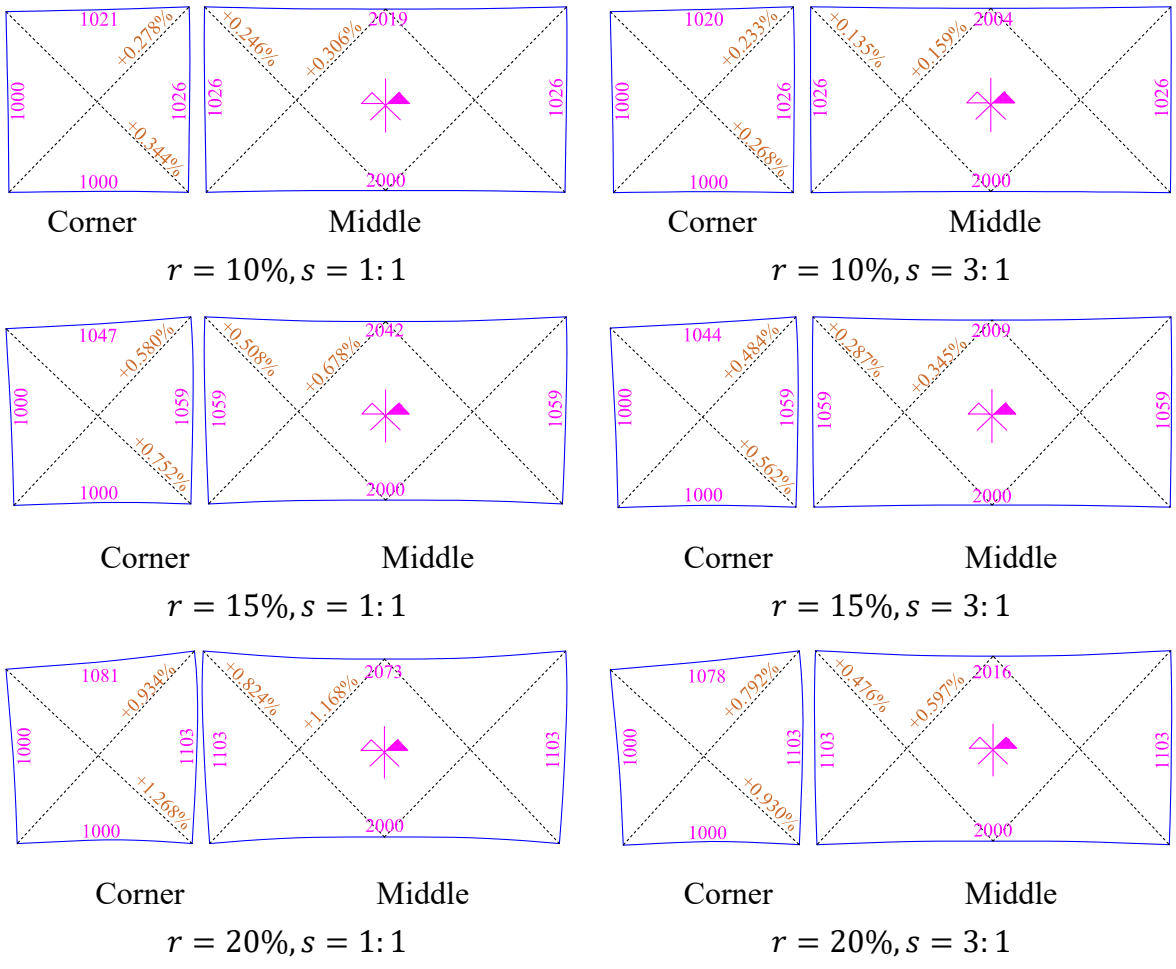

Figure 2.10 The cutting pattern results
(All dimensions are in millimeter)

2.5 Summary

(a) It should be noted that there is no guarantee that the form finding procedure in section 2.2 will always convergence. The convergence problems could be occurred by the shape of structures, the initial configuration of structures, the boundary conditions and the mesh generation.

(b) The accuracy of the suggested tools *FF* & *CP* was confirmed by the in-house software of Taiyo Kogyo Corp., for the case studies of the saddle type of tensile membrane structures.

(c) Saddle type of tensile membrane structures: the increment of rise ratio is accompanied with the increment of the curvature of ideal curved surface and the increment of expansion of drape strips. The selection of prescribed stress ratio can decrease those increments.

(d) The experiments are essential to investigate the possibility of establishment of the three-dimensional curved surface by stretching the combination of drape strips of several prescribed stress ratios and/or plane strips.

Chapter 3.
Fabrication of three-dimensional curved surface using ETFE film by stretching plane strips

Chapter 3. Fabrication of three-dimensional curved surface using ETFE film by stretching plane strips

3.1 Introduction

Generally, the ETFE film is manufactured in rolls of around *1.5* meter. The strips of film are cut and jointed together to procedure the desired curved surfaces. It should be noted that the smaller the width of the strip is, the closer the obtained curved surface approaches the real curved surface [KI99]. When strips are jointed, the heat welding techniques are generally used.

In the fabrication of relatively small area of curved surface using ETFE film, the fine division of curved surface into strips is difficult. The reasons can be explained as: (1) the difficulty of heat welding increases when the curvature of curved surface is large; (2) the strength of material decreases because of the weld lines; (3) the aesthetic of structures is affected by the increment of weld lines. Besides, the ETFE film can be elongated up to 400% of nominal strain under uniaxial test, and the yield strength of the film can be increased after the film is drawn to its plastic region due to the hardening characteristics. Therefore, the fabrication of ETFE curved surface with a few of weld lines and the high yield strength is pursued. Specially, if the possibility of fabrication of curved surface from plane strips is confirmed, the effectiveness of construction work will be increased sharply. The first reason is that the heat welding work of plane strips is simpler than that of drape strips of large curvature. The second reason is that the form finding and cutting pattern analysis are not necessary.

Therefore, this chapter will introduce the proposed fabrication method in which the possibility of establishment of the three-dimensional curved surfaced from plane strips can be checked. In this proposed fabrication method, the detail connections between the films and the outside frames are improved by the novel technique of Taiyo Kogyo Corp., in which the boundary of the films can be drawn freely. As a result, the possibility of fabrication of the curved surface is increased by the adjustment of drawing values. When the boundary of the film is drawn, the slide between the films and the supporting frames occurs. It means that the slide or the friction contact between the films and the supporting frames cannot be ignored in this fabrication method. In this chapter, therefore, the values of slide between the ETFE film and supporting galvanized steel arches are also investigated.

3.2 Overview of stretch fabrication experiments

3.2.1. The process of experiments

The saddle type of tensile membrane structure, which was introduced in Chapter 2, is investigated in these experiments. The parts of the film between supporting arches and outside frames are called corner parts, while the parts between two arches are called middle parts.

The process of stretch fabrication experiments is presented in Figure 3.1. First, the form finding analysis is carried out to find the ideal shapes of the corner parts with *3:1* of prescribed stress ratio between *X* (or *MD*) and *Y* (or *TD*) directions. The films are drawn at boundary positions, so the prescribed stress ratio of *3:1* is chosen for the corner parts in order to encourage that the pretension stress for the middle part can be introduced sufficiently (Figure 2.10). Second, the cutting pattern analysis is used to find the drape strips for the corner parts. It should be noted that the plane strips, which are not draped, are used for the middle parts. Third, those parts are jointed together into specimens by heat welding techniques, and these specimens are spread on the frames of experiments. Next, the boundaries of the specimens are drawn to introduce the pretension stress on the films. Finally, the final shapes are obtained and checked for the sufficiency of prestress and the absence of wrinkling.

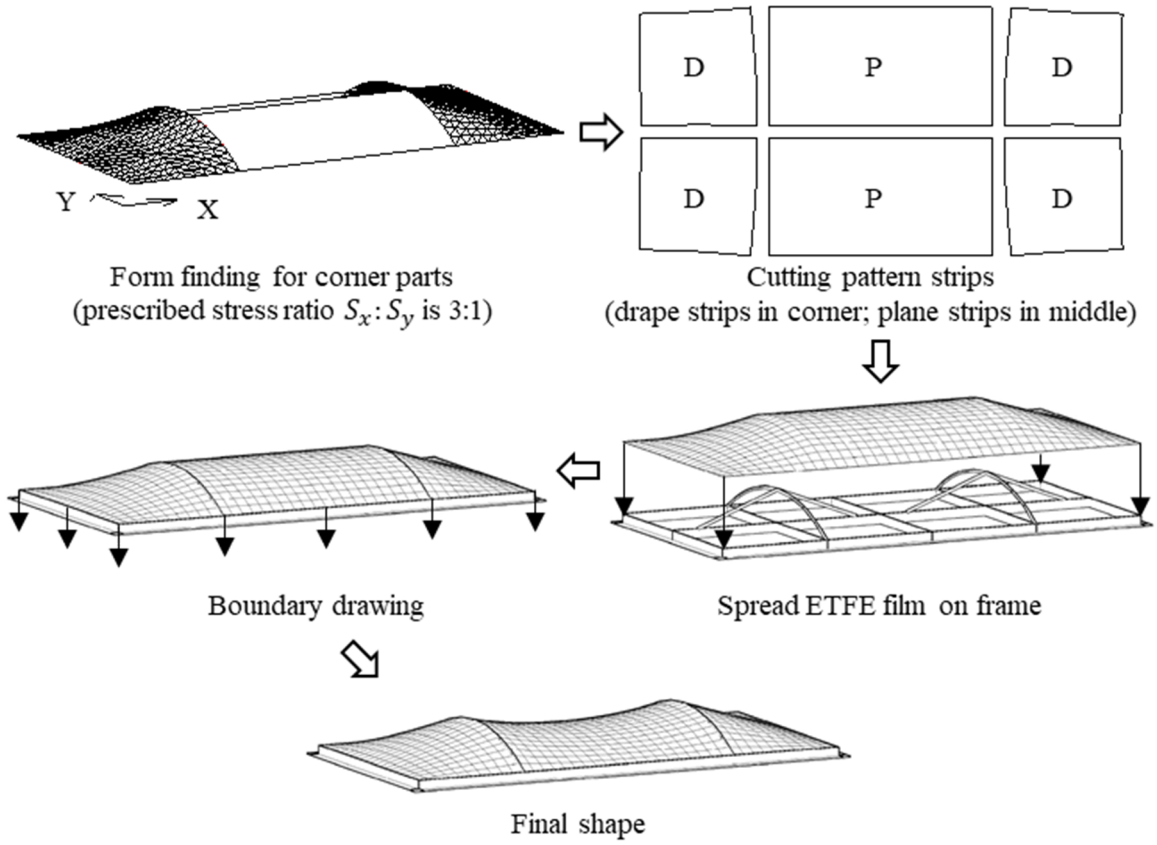

Figure 3.1 The process of stretch fabrication experiments, plane strips for middle part

The dimensions of the frames of experiments are shown in Figure 3.2. There are three types of the height of arch *H* as *200mm, 300mm* and *400mm* which correspond to *10%, 15%* and *20%* of rise ratios. The definition of rise ratio can be referred in section 2.4.

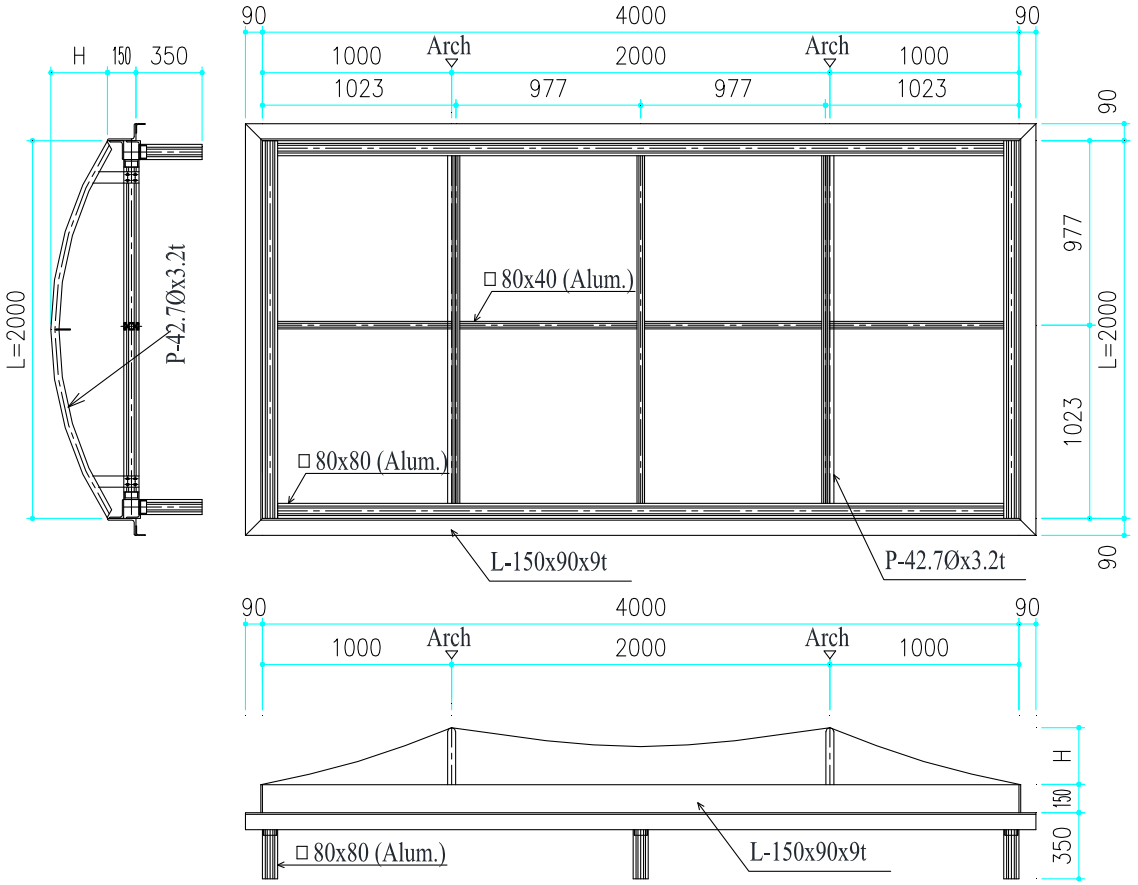

Figure 3.2 The frame of experiments (All dimensions are in millimeter)

3.2.2. Specimens

The thickness of ETFE film was *250μm* in these experiments. There are three types of specimens which are named as *PD10, PD15* and *PD20*. While the letter *"P"* denotes the plane type of strip for the middle part, the letter *"D"* indicates the drape type of strip for the corner part. The number *10, 15* and *20* present the rise ratios of *10%, 15%* and *20%*, respectively. The cutting strips of corner part and middle part in those types of specimens are shown in Figure 3.3. The numbers show the lengths of cutting lines, while the percentages indicate the expansions of the lengths in drape strips and the corresponding lengths of the form finding shapes in Figure 3.3.

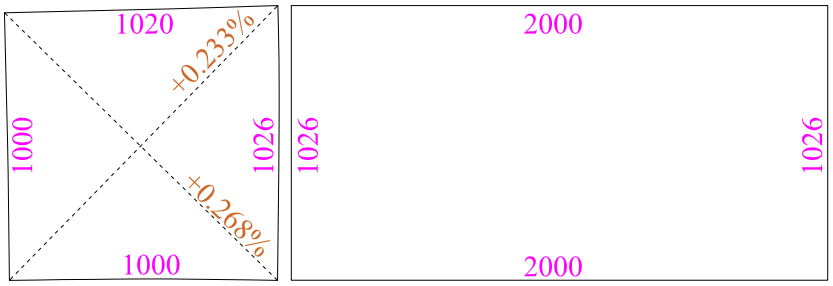

a. PD10 specimens

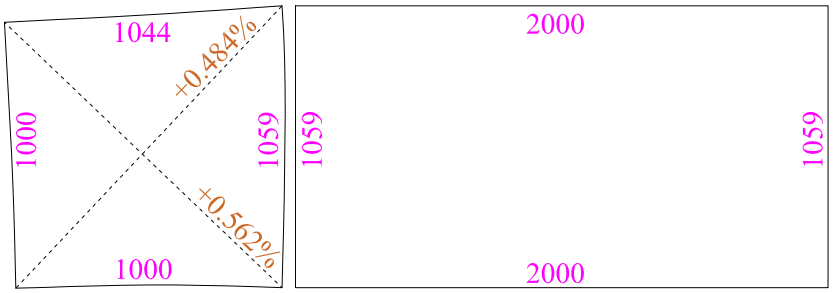

b. PD15 specimens

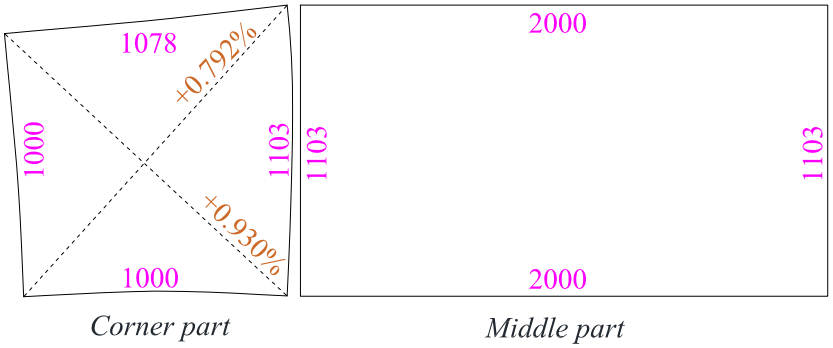

c. PD20 specimens

Figure 3.3 Types of cutting strips

Each type of cutting strips has two specimens named as *a* and *b*, so there are six specimens totally. Table 3.1 represents the information of specimens.

Table 3.1 Information of specimens

Specimens	Rise ratio	Types of cutting strip		ETFE properties	
		Corner	Middle	Thickness	Type
PD10a/b	*10%*	*Drape (3:1)*	*Plane*	*250 μm*	*Printed dot*
PD15a/b	*15%*	*Drape (3:1)*	*Plane*	*250 μm*	*Printed dot*
PD20a/b	*20%*	*Drape (3:1)*	*Plane*	*250 μm*	*Printed dot*

3.2.3. The process of drawing

The values of drawing at four special boundary positions are shown in Figure 3.4a, while those values at other positions are interpolated linearly as shown in Figure 3.4b. The values of *a*, *b*, *c* and *d* are input step by step to introduce the prestress on the film during the experiments. The target prestress is around the first yield points of ETFE film, so the values of *a, b, c* and *d* are determined to guarantee the sufficient prestress. In addition, the limited values of *a, b, c* and *d* are *80mm* due to the setup of experiments, and the relations between *a, b, c* and *d* are controlled by the absence of wrinkling.

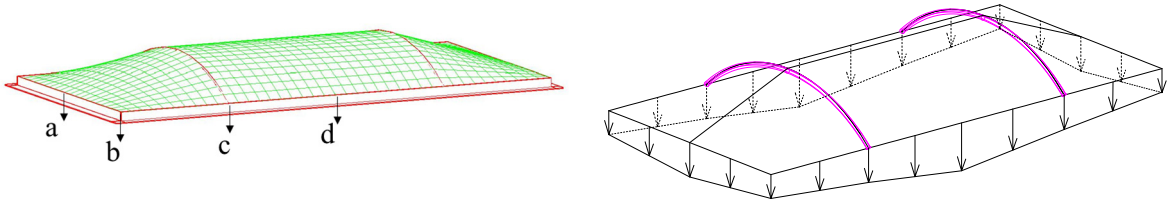

a. Values of drawing boundary at four special positions

b. The linear interpolation of drawing boundary at other positions

Figure 3.4 The values of drawing boundary

Figure 3.5 shows the process of drawing over six specimens. In this figure, the lines with circle, square, diamond and triangle makers show the drawing values of *a*, *b*, *c* and *d* during the process of experiments, respectively. Generally, the drawing values increased during the experiments. However, only the drawing value of *d* needed to input in some last steps for the high-rise ratio specimens (*PD15*, *PD20*). The reason can be explained that the prestress in *TD* direction or short direction need to be more introduced.

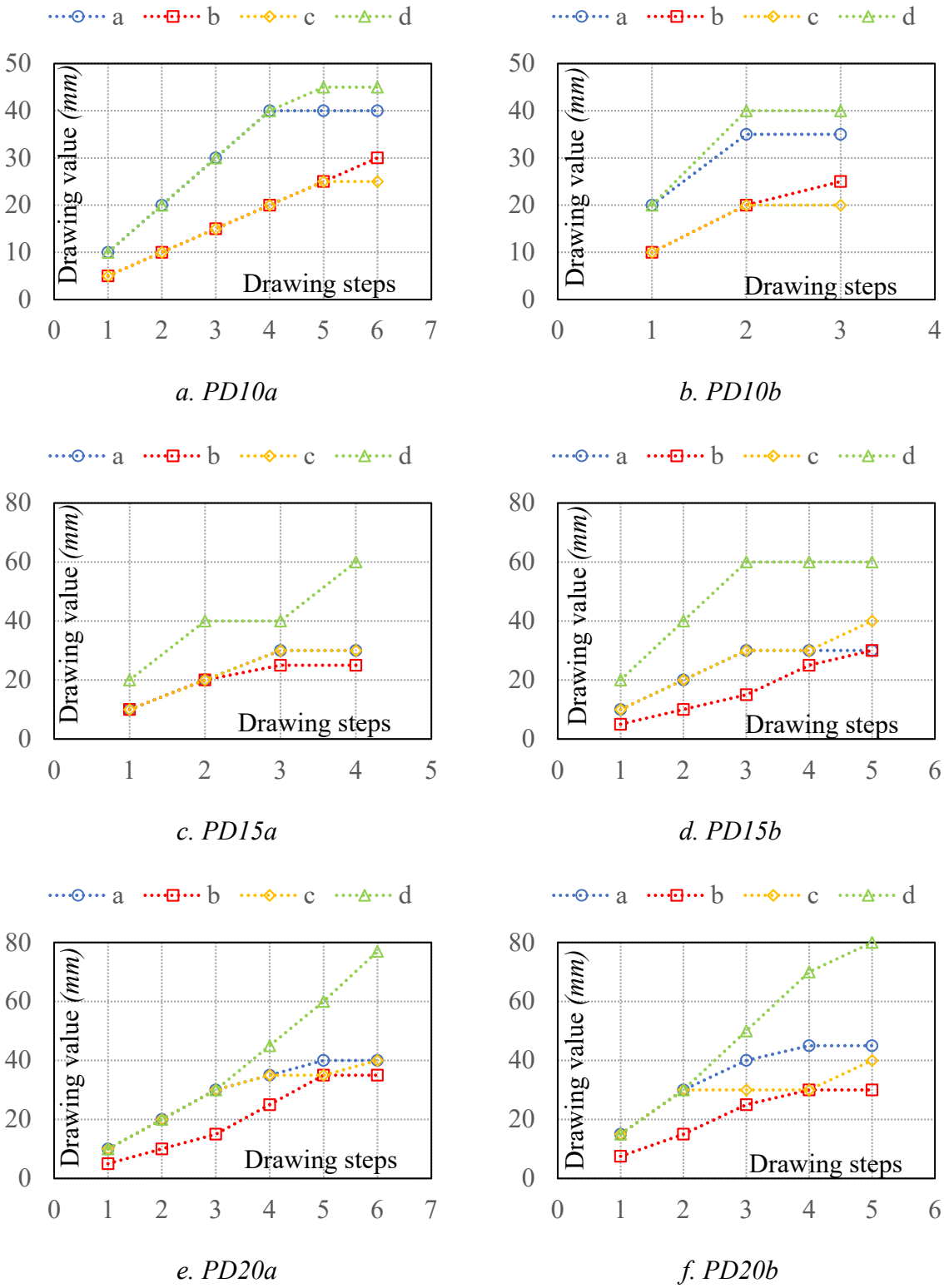

a. PD10a *b. PD10b*

c. PD15a *d. PD15b*

e. PD20a *f. PD20b*

Figure 3.5 The process of drawing

3.3 Observation methods, results and discussions

3.3.1. Observed engineering strains

The lengths of four segments ($l_1 \rightarrow l_4$) in Figure 3.6 were measured by tape measurement with precision of *0.5mm* during the process of drawing. The engineering strains can be obtained by these observations as shown in Eq. (3.1).

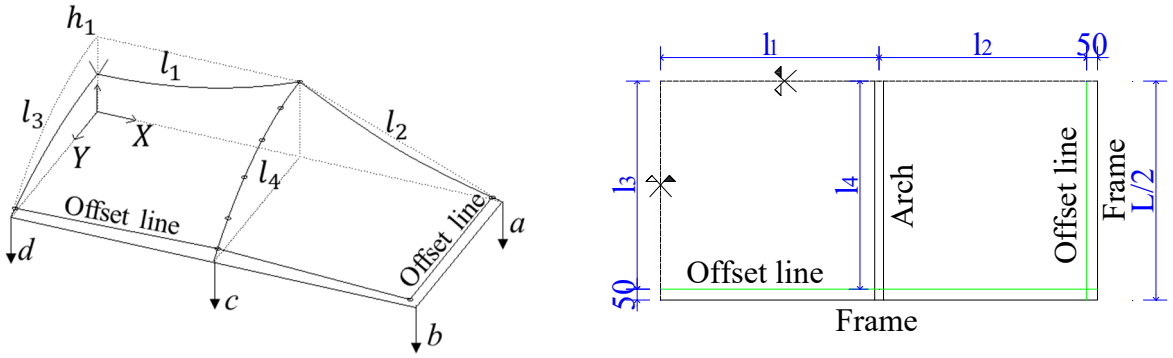

a. 3D view of a quarter of specimens *b. Plane view of a quarter of specimens*

Figure 3.6 The observed lengths of four segments

$$ {}_k\varepsilon_i = \frac{{}_kl_i - {}_0l_i}{{}_0l_i} \tag{3.1}$$

where, ${}_k\varepsilon_i$ is the engineering strain of segment *i* at step *k*, ${}_0l_i$ and ${}_kl_i$ are the lengths of segment *i* at the initial step and step *k*, respectively.

Figure 3.7 shows the results of the observed engineering strains throughout six specimens. In this figure, the lines with the circle, square and triangle markers show the results of specimens *PD10*, *PD15* and *PD20*, respectively. While the solid lines indicate the results of specimens *PD10a*, *PD15a*, *PD20a*, the dash lines represent the results of specimens *PD10b*, *PD15b*, *PD20b*.

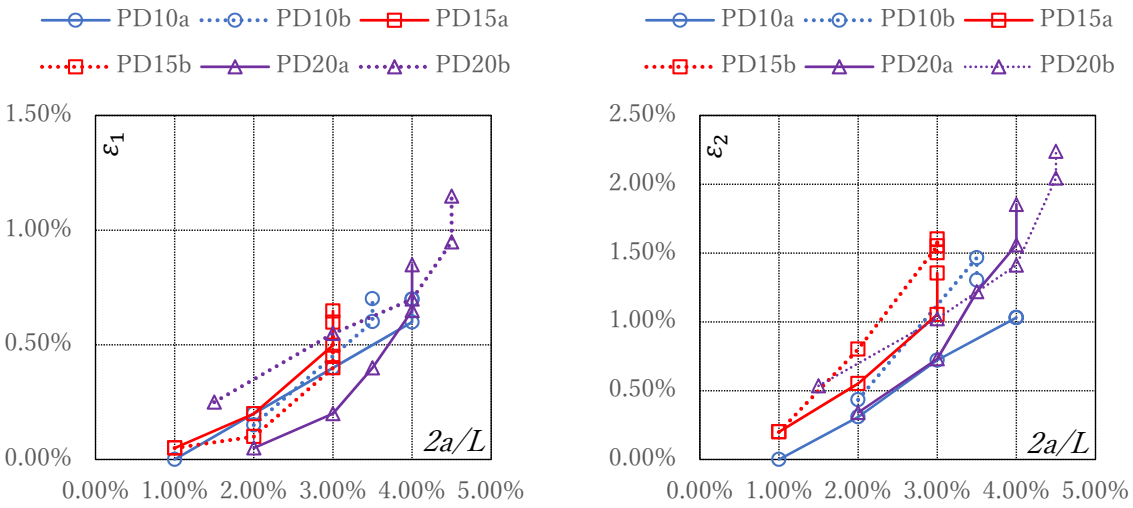

a. Engineering strain ε_1 *b. Engineering strain* ε_2

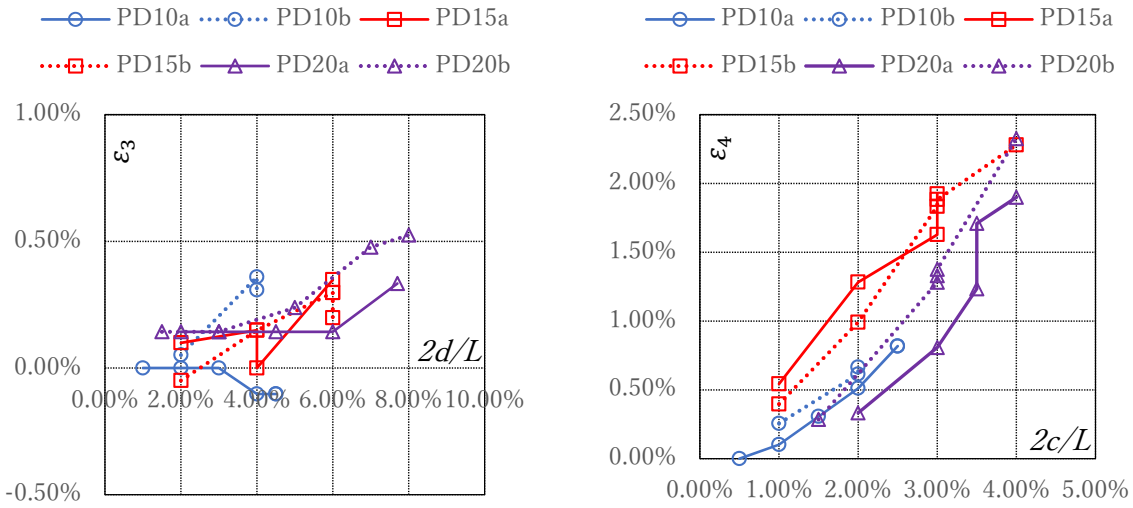

c. Engineering strain ε_3 *d. Engineering strain* ε_4

Figure 3.7 The results of engineering strains

In the middle part, the target input engineering strains in *MD* direction or long direction (ε_1) and in *TD* direction or short direction (ε_3) are around from *0.5%* to *1.0%*. The plane strips were used for this part, so the effect of saddle height, which is denoted as h_1 as shown in Figure 3.6a, was obvious, especially in *TD* direction. The higher the rise ratio was, the harder the input engineering strain for *TD* direction was. As it can be seen from Figure 3.7c, the input engineering strain reached to the target of around *0.5%* when the ratios between drawing value of *2d* and span of structure *L* were about *8%*, *6%* and *4%* for the specimens *PD20*, *PD15* and *PD10*, respectively. It means that the drawing value of *d* must increase with the increment of rise ratio. However, the increment of *d* accompanies with the occurrence of wrinkling. This

problem will be indicated in section 3.3.3.

In the corner part, the input engineering strain in *MD* direction (ε_2) reached the values of around *1.5%* when the drawing ratio *2a/L* was around *3%* to *4%* throughout three values of rise ratios. The input prestress was introduced for this part easily because the drawing could be carried out at three positions of *a*, *b* and *c*.

3.3.2. Observed Green-Lagrange strain and Mises stress

The lengths of four edges and two diagonals of part *A* and part *B* in Figure 3.8 were measured by tape measurement with precision of *0.5mm* during the experiments. The Green-Lagrange strains of those parts could be calculated depending on the assumption that: (1) The *x* direction of each part remained constant as *X* direction during the experiments; (2) all parts were assumed in plane stress condition. Figure 3.9 indicates the assumptions for this calculation.

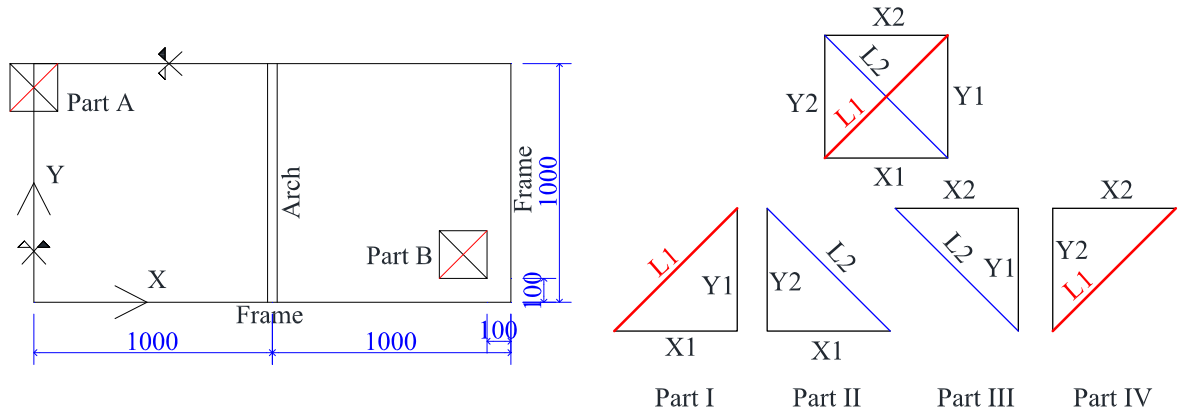

a. Positions of part A & part B *b. Observed lengths*

Figure 3.8 Observed lengths at part A & part B

The Green-Lagrange strains can be obtained by the equation Eq. (3.2)

$$\begin{Bmatrix}\varepsilon_{xx}\\ \varepsilon_{yy}\\ \varepsilon_{xy}\end{Bmatrix} = \frac{1}{2S}\begin{bmatrix} y_k - y_i & y_i - y_j & 0\\ 0 & 0 & x_j - x_i\\ x_i - x_k & x_i - x_j & y_i - y_j\end{bmatrix}\begin{Bmatrix}u_j\\ u_k\\ v_k\end{Bmatrix} \quad (3.2)$$

where, $x_i = 0$, $y_i = 0$, $x_j = {}^0L_k$, $y_j = 0$, $x_k = {}^0L_j\cos(\alpha_0)$, $y_k = {}^0L_j\sin(\alpha_0)$
$u_j = {}^nL_k - {}^0L_k$, $u_k = {}^nL_j\cos(\alpha_n) - {}^0L_j\cos(\alpha_0)$, $v_k = {}^nL_j\sin(\alpha_n) - {}^0L_j sin(\alpha_0)$, S is area of triangle *ijk* at the initial step, ${}^0L_j$, ${}^0L_j$, ${}^0L_k$ are the lengths of segments *i, j, k* at the initial step, ${}^nL_j$, ${}^nL_j$, ${}^nL_k$ are the lengths of segments *i, j, k* at step *n* and ${}^0L_j$, ${}^0L_j$, ${}^0L_k$, ${}^nL_j$, ${}^nL_j$, ${}^nL_k, \alpha_0, \alpha_n$ are described in Figure 3.9.

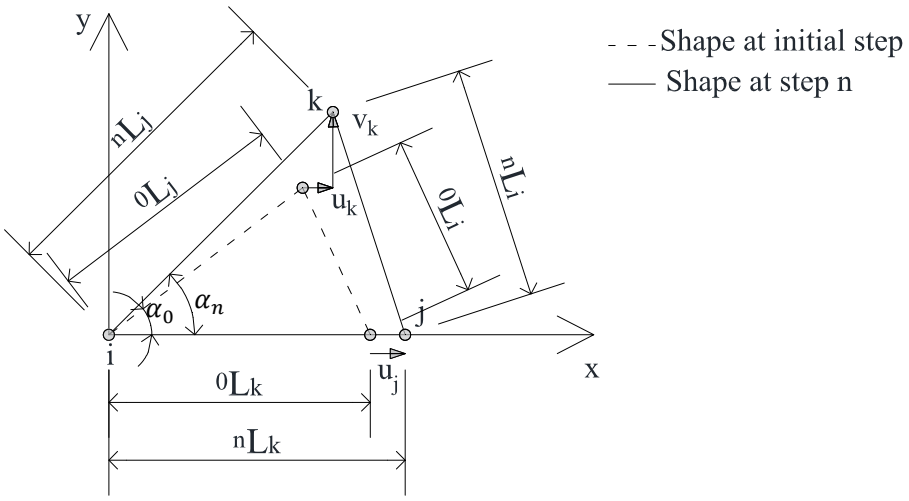

Figure 3.9 The assumptions of calculation of Green-Lagrange strains

The average values of Green-Lagrange strains in *MD* direction (ε_{xx}), *TD* direction (ε_{yy}) and shear strain (ε_{xy}) of part *A* and part *B* during the process of drawing are shown in Figure 3.10 and Figure 3.11, respectively. In these figures, lines with the circle, rectangle and triangle markers present the results of ε_{xx}, ε_{yy} and ε_{xy}, respectively. In addition, the Green-Lagrange strains are printed in the relationship with the ratio between the drawing value of *d* and span of structure *L* in Figure 3.10, while these strains are plot in the relationship with ratio between the drawing value of *b* and span *L* in Figure 3.11.

At part *A*, the strain of *TD* direction (ε_{yy}) was almost zeros in case of *PD15* and *PD20*, while the strain of *MD* direction (ε_{xx}) and the shear strain (ε_{xy}) were large. This made the wrinkling occurred at this part and smooth curved surface could not be obtained in case of high-rise ratio (*15% and 20%*).

In case of *PD10*, the decrements of Green-Lagrange strains were observed at part *A* at the final step. The reason can be explained that the drawing process at the final step occurred only at corner part (*b* position only). The same phenomenon was observed in case of *PD15b*. Therefore, it is recommended that the drawing process should be carried out all over of specimen at each step of fabrication.

At part *B*, the Green-Lagrange strains increased gradually with the increment of drawing value at *b* position. The limit value of drawing value *b* is around *30mm* because the damage of ETFE was observed at the corner of outside frame.

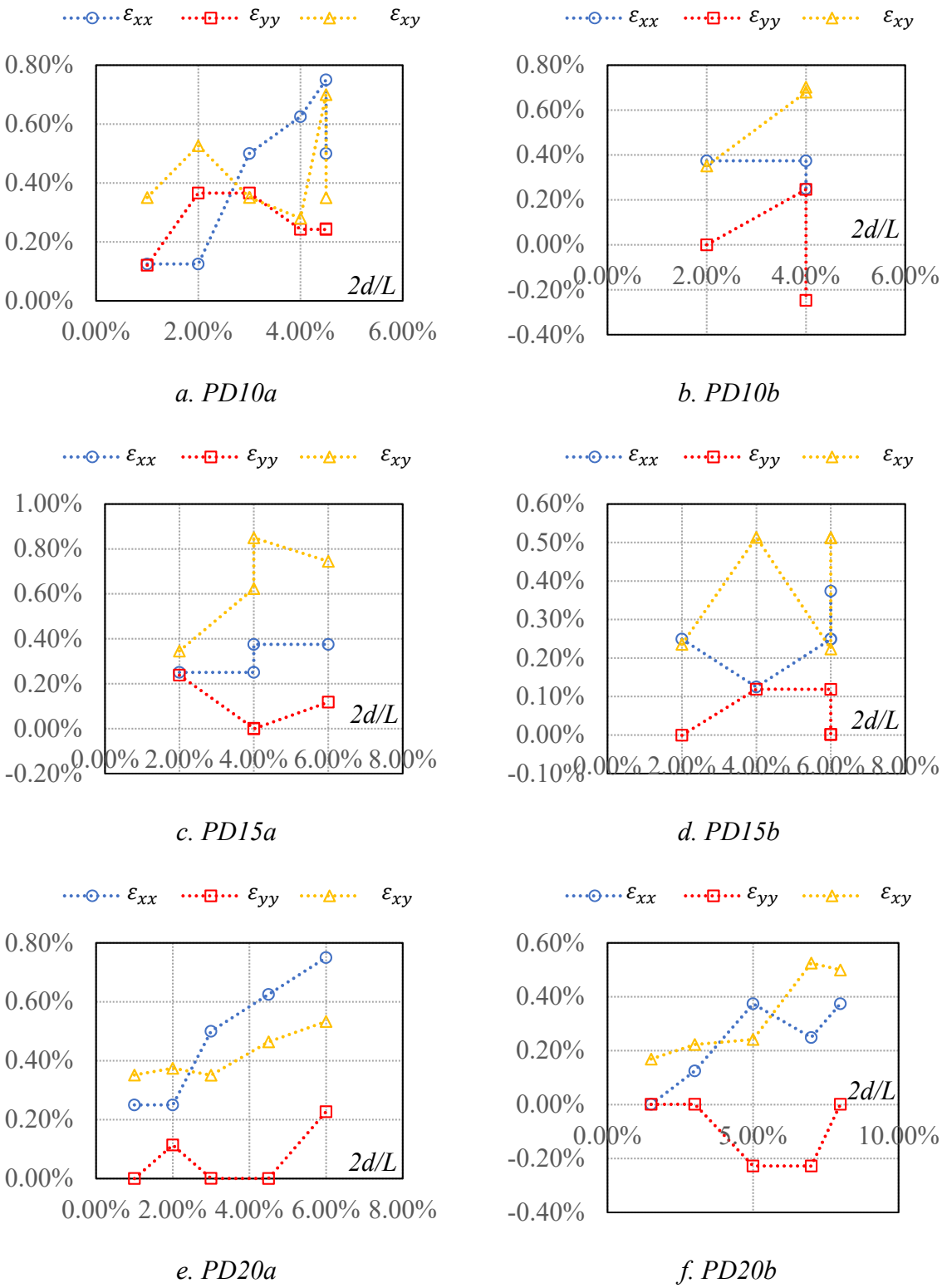

Figure 3.10 The Green-Lagrange strains of part A during the experiments

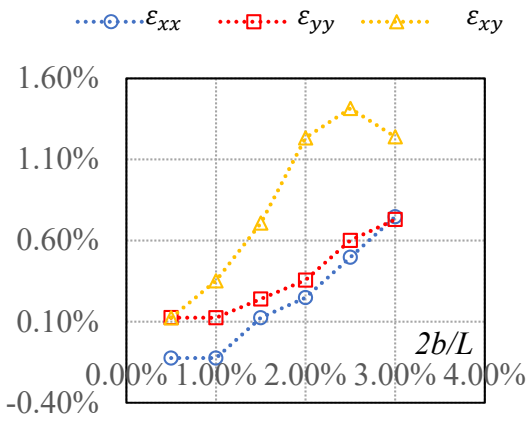

a. PD10a

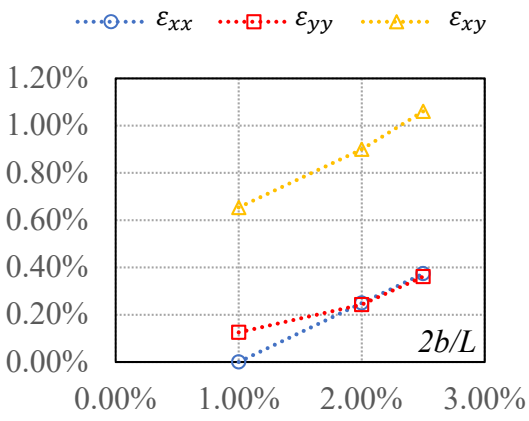

b. PD10b

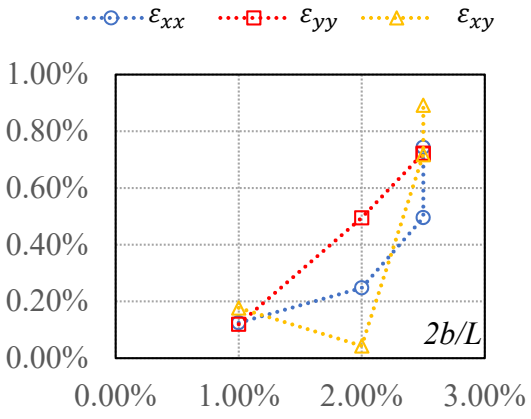

c. PD15a

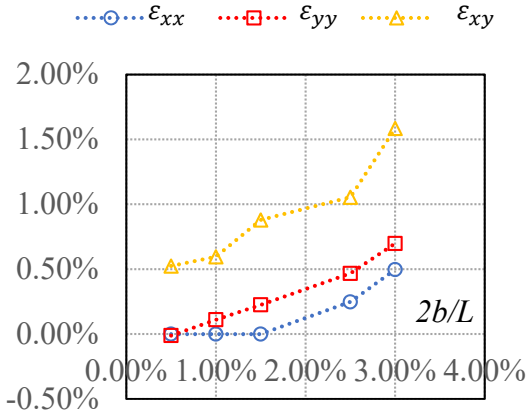

d. PD15b

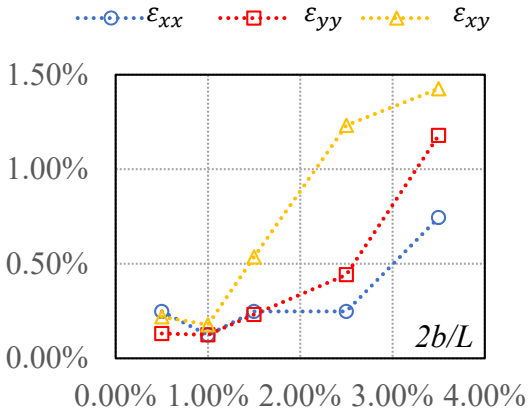

e. PD20a

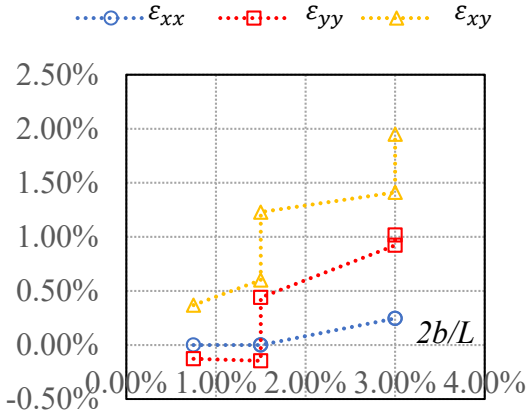

f. PD20b

Figure 3.11 The Green-Lagrange strains of part B during the experiments

The 2nd Piola-Kirchhoff stresses of part *A* and part *B* can be obtained by Eq. (3.3). Here, part *A* and *B* were assumed in plane stress condition.

$$\begin{Bmatrix} S_{xx} \\ S_{yy} \\ S_{xy} \end{Bmatrix} = \frac{E}{1-\nu^2} \begin{bmatrix} 1 & \nu & 0 \\ \nu & 1 & 0 \\ 0 & 0 & \dfrac{1-\nu}{2} \end{bmatrix} \begin{Bmatrix} \varepsilon_{xx} \\ \varepsilon_{yy} \\ \varepsilon_{xy} \end{Bmatrix} \tag{3.3}$$

where, *E* and ν are Young modulus and Poisson's ratio of ETFE film, respectively.

The Mises stress is determined by the Eq. (3.4)

$$S_{eq} = \sqrt{{S_{xx}}^2 + {S_{yy}}^2 - S_{xx}S_{yy} + 3{S_{xy}}^2} \tag{3.4}$$

The results of Mises stresses are shown in Figure 3.12. The dash lines with circle and rectangle markers show the average values of specimens *a* and *b*, respectively. The bar and error bar indicate the maximum and minimum values. The input Mises stress of part *A* was insufficient because the plane strips were used in the middle part. The Mises stress almost reached the target stress of the first yield point of ETFE film at part *B*. The drape strips with prescribed stress ratio of *3:1* were used for the corner part. The drawing values of around *3%* to *4%* of span were input at the boundary. Those fabrication process can be accepted for the corner part throughout three values of rise ratios.

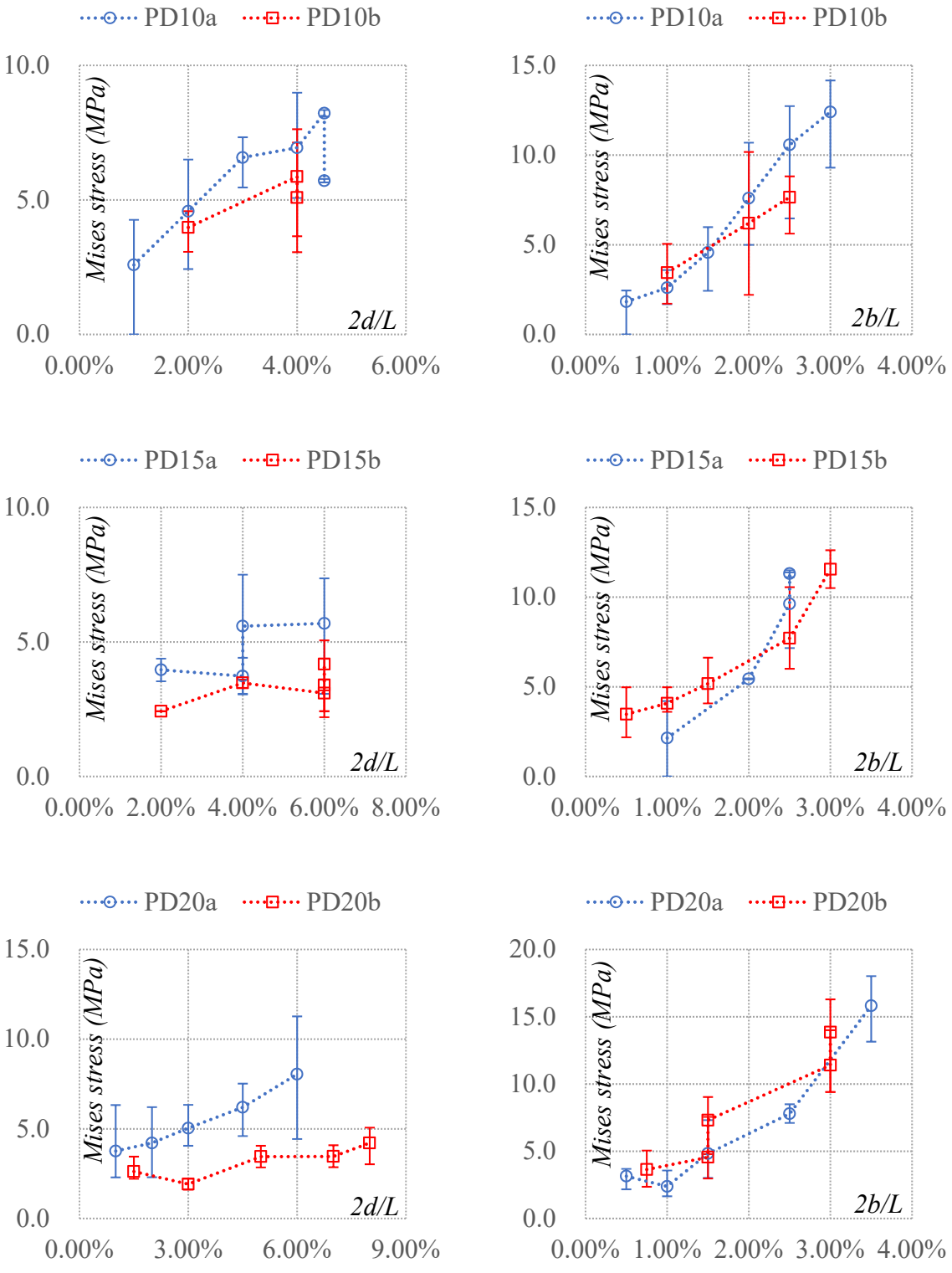

a. Part A *b. Part B*

Figure 3.12 The results of Mises stress during the experiments

3.3.3. Smooth curved surface

The smooth curved surface, which is the curved surface without the wrinkling, could be only obtained for the low-rise ratio case of *10%* (*PD10*). Figure 3.13 shows the initial and final shapes of *PD10a* and *PD10b*.

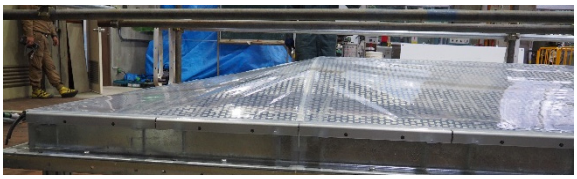

a. PD10a, Initial shape

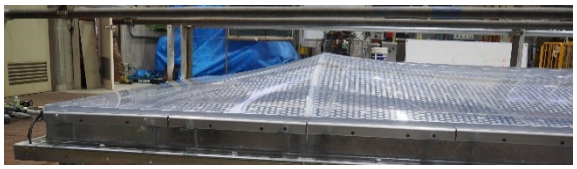

b. PD10a, Final shape

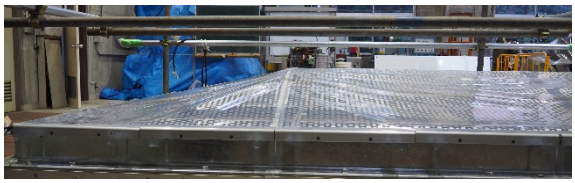

c. PD10b, Initial shape

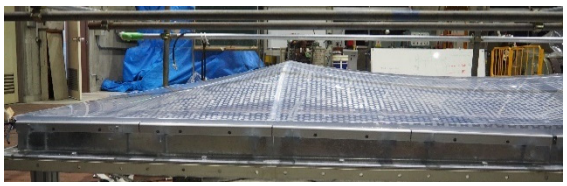

d. PD10b, Final shape

Figure 3.13 Smooth curved surfaces in case of rise ratio of 10%

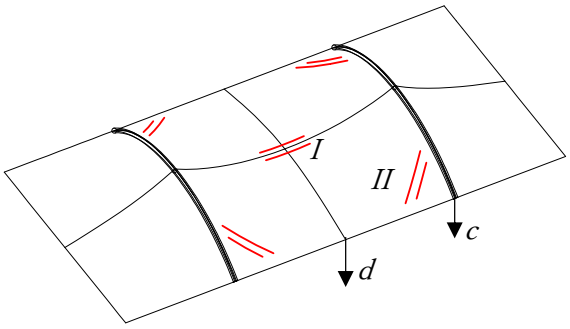

a. Positions of wrinkling in 3D view

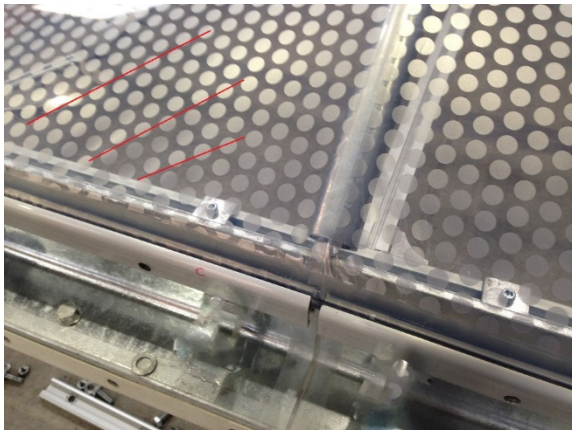

b. PD15a

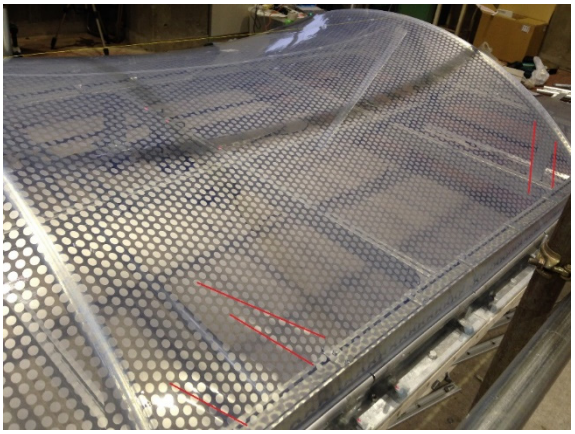

c. PD20a

Figure 3.14 Positions of occurred wrinkling in case of PD15 & PD20

The wrinkling could not be erased at the final step of drawing process for the high-rise ratio of *15%* and *20%* (*PD15* & *PD20*). The positions of occurred wrinkling are shown in Figure 3.14. The occurrence of wrinkling at position *I* (Figure 3.14a) can be explained by: (1) the stress of this position was mainly introduced in *MD* direction or long direction; (2) the shear stress was large. As a result, the minimum principal stress of this position was almost smaller than zeros, and the wrinkling occurred. The minimum principal stress of part *A* can be used as the representative sample of this reason. This stress can be obtained by Eq. (3.5) and are shown in Figure 3.15. The circle markers show the average values of minimum principal stress, while the error bars indicate the maximum and minimum values of this stress at part *A* in Figure 3.15.

$$S_{min} = \frac{S_x + S_y}{2} - \sqrt{\frac{(S_x - S_y)^2}{4} + {S_{xy}}^2} \tag{3.5}$$

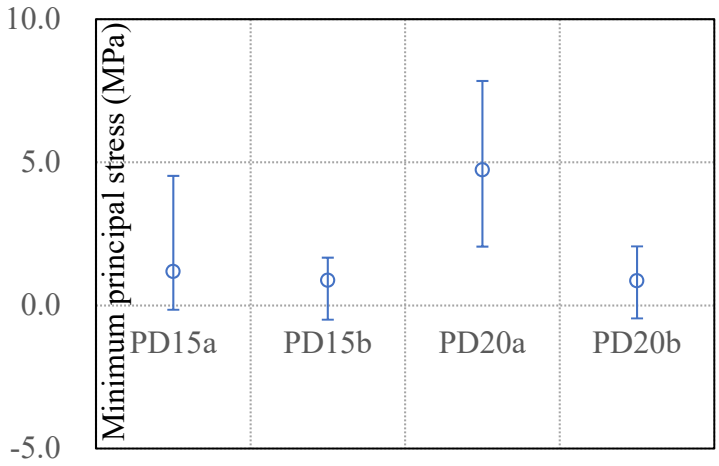

Figure 3.15 Minimum principal stress of part A

The occurrence of wrinkling at position *II* can be explained by the discrepancy between the drawing values at *d* and *c* positions. The drawing value of *d* position has to introduce dramatically to reach the target prestress for the high-rise ratio cases. However, the increment of *d* is accompanied with the decrement of minimum principal stress at position *II* (Figure 5.12b). Consequently, the wrinkling occurred at position *II* in case of high-rise ratios of *15%* and *20%*.

3.3.4. Motions of offset points

The motions of offset points on the ETFE film versus the fix points of outside frame were observed by the carpenter's square with precision of *0.5mm* during the drawing process of experiments. Those movements can be used as the forced displacement conditions in the analysis of predictions behaviors of ETFE film for the stretch fabrication experiments in the next chapters. The positions of offset points are shown in Figure 3.16.

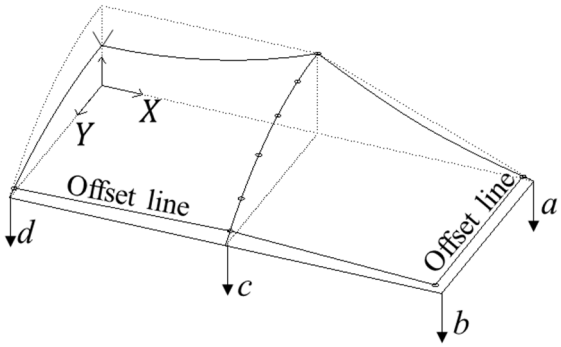

a. Positions of offset point in 3D view

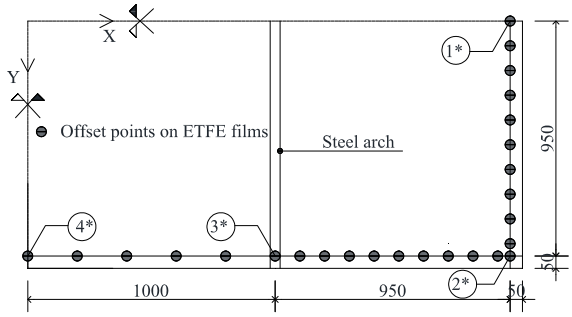

b. Positions of offset point in 2D view

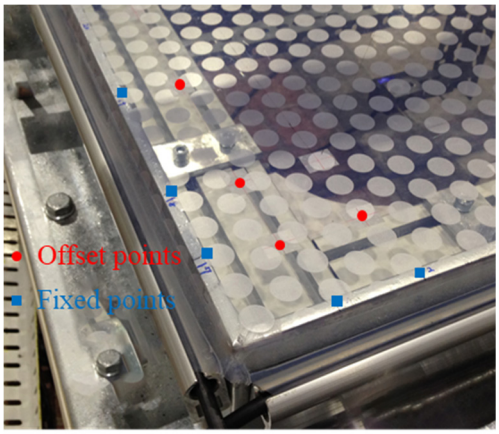

c. Photo of the corner part, PD10a

Figure 3.16 Positions of offset points

The relations between the drawing values of *a*, *b*, *c* and *d* and the movements of special offset points *1**, *2**, *3** and *4** are shown in Figure 3.17. In this figure, the circle, square, diamond, triangle, minus and star markers show the results of *PD10a*, *PD10b*, *PD15a*, *PD15b*, *PD20a* and *PD20b*, respectively. The dash lines present the linear regression lines [RB09] between the drawing values and the motions of offset points. The linear functions of these regression lines are also presented, and these functions can be used to predict the movements of offset points during the process of experiments.

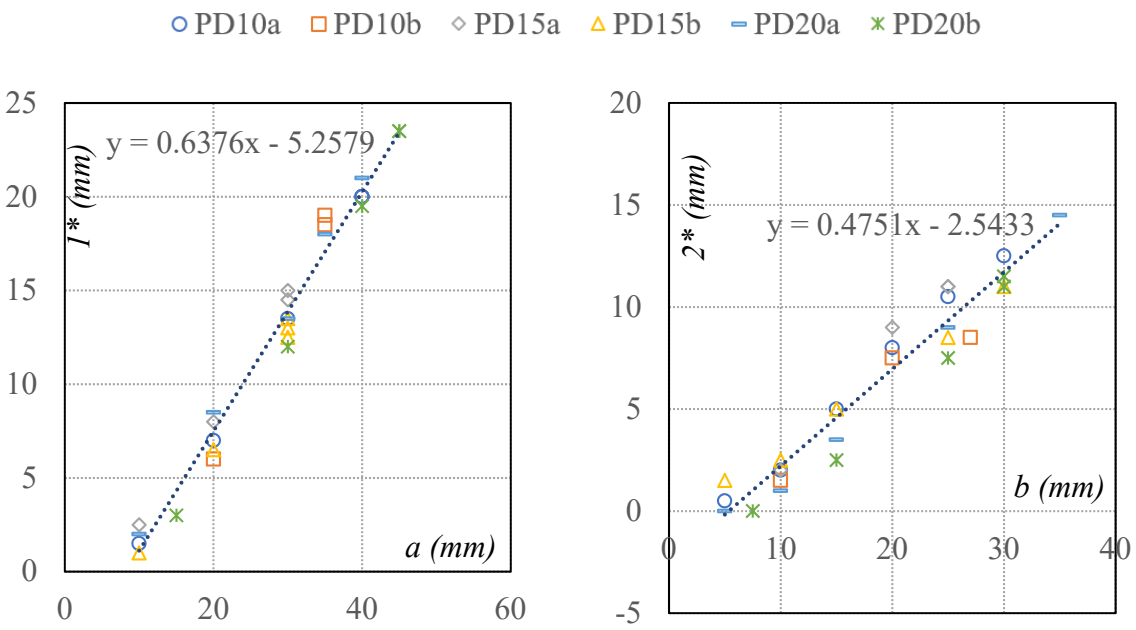

a. a and movement of 1 in X direction*

b. b and movement of 2 in X direction*

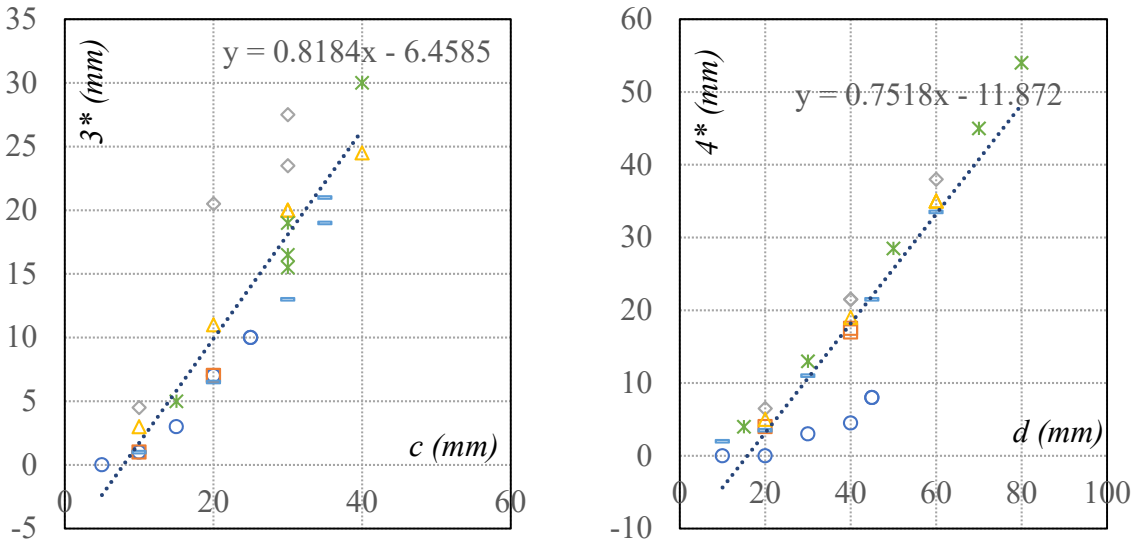

c. c and movement of 3 in Y direction*

d. d and movement of 4 in Y direction*

Figure 3.17 The relations between drawing values and movements of offset points

3.4 Observed slide between ETFE film and supporting arches

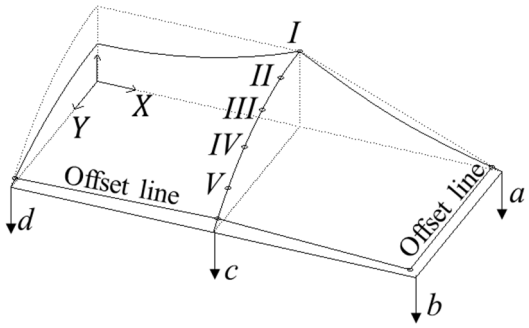

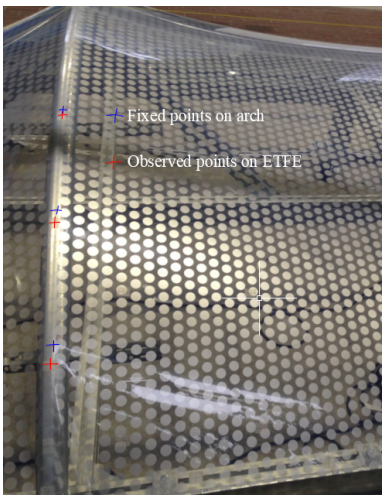

a. 3D view of a quarter of specimens *b. Photo of specimen PD20a, final state*

Figure 3.18 The observed slide at five positions

The slide between the red marked points of ETFE film and the fixed blue marked points of arches (Figure 3.18b) were measured by the carpenter's square with precision of *0.5mm* at five positions (Figure 3.18a) during the process of drawing. Those measurements were carried out in both *X* and *Y* directions. The results of these slides will be used to confirm the suggested analytical method which will be introduced in the next chapter. Figure 3.19 shows the photos of those movements during the experiments. In this figure, the blue marked points indicate the fixed points of galvanized steel arches, while the red marked points present the corresponding observed slide points of ETFE film.

The relations between slide values in *X* and *Y* directions are shown in Figure 3.20. In this figure, the dash lines with circle, square, diamond, triangle and minus makers present the results of slide at *I*, *II*, *III*, *IV* and *V* positions, respectively. Generally, the slide in *Y* direction increased with the increment of drawing value of *c*. The slide in *X* direction at point *II* and *III* changed the direction when drawing process occurred only at *d* position. This phenomenon could be seen in case of *PD15a*, *PD15b*, *PD20b* specimens. The slide at point *I* occurred mainly in X direction because of the symmetry of specimens.

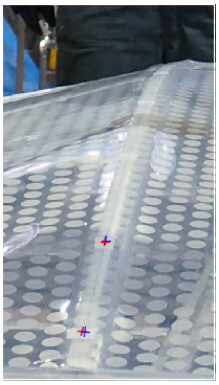

Initial

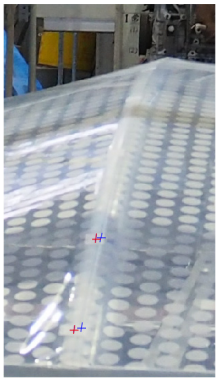

Step 4

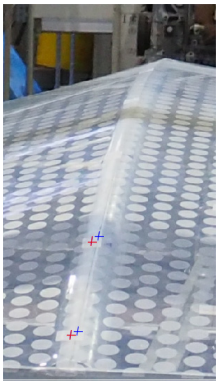

Final step

a. PD10a

Initial

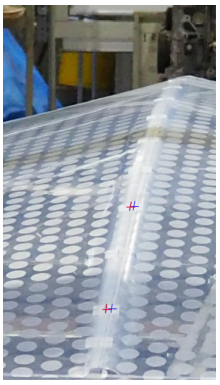

Step 2

Final step

b. PD10b

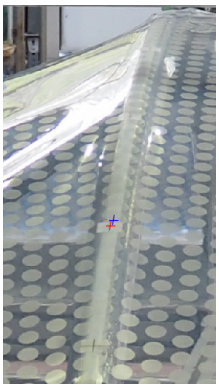

Initial

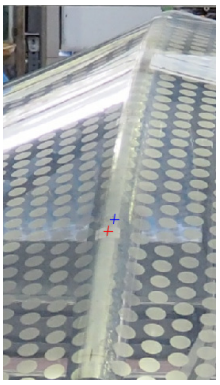

Step 2

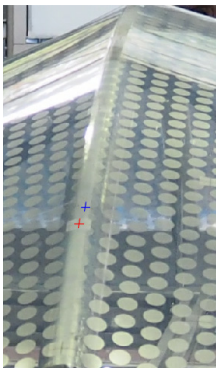

Final step

c. PD15a

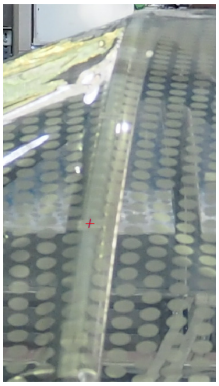

Initial

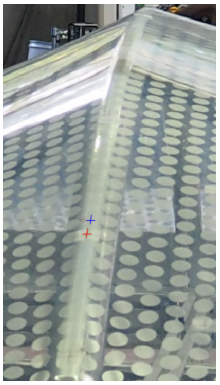

Step 3

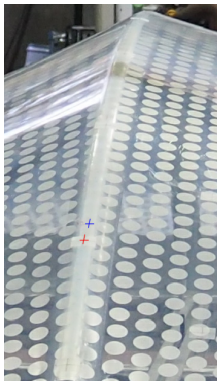

Final step

d. PD15b

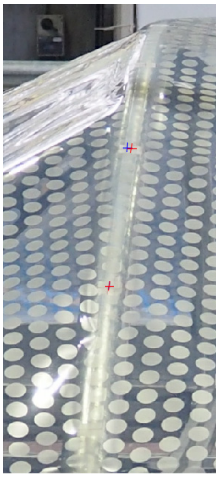

Initial

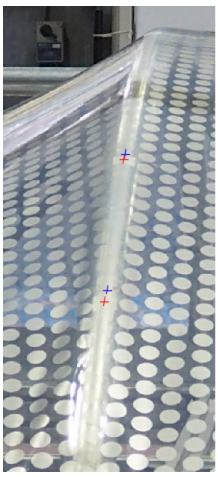

Step 3

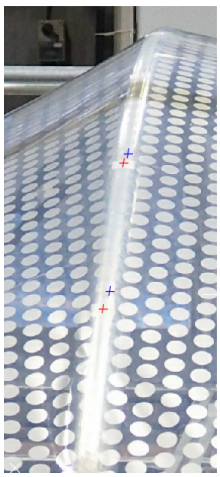

Final step

e. PD20a

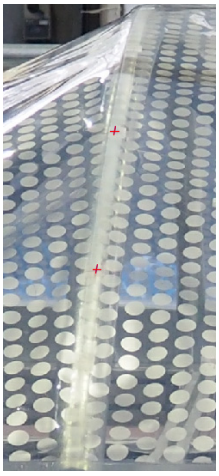

Initial

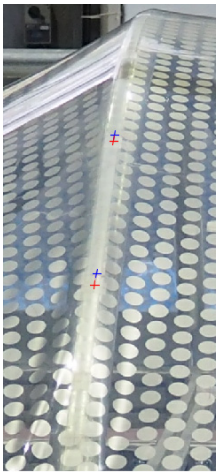

Step 3

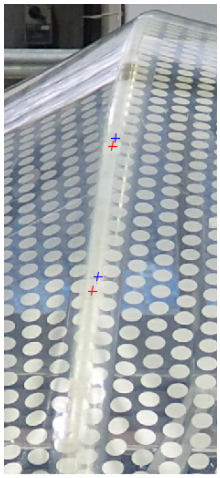

Final step

f. PD20b

Figure 3.19 The photos of observed slide over six specimens

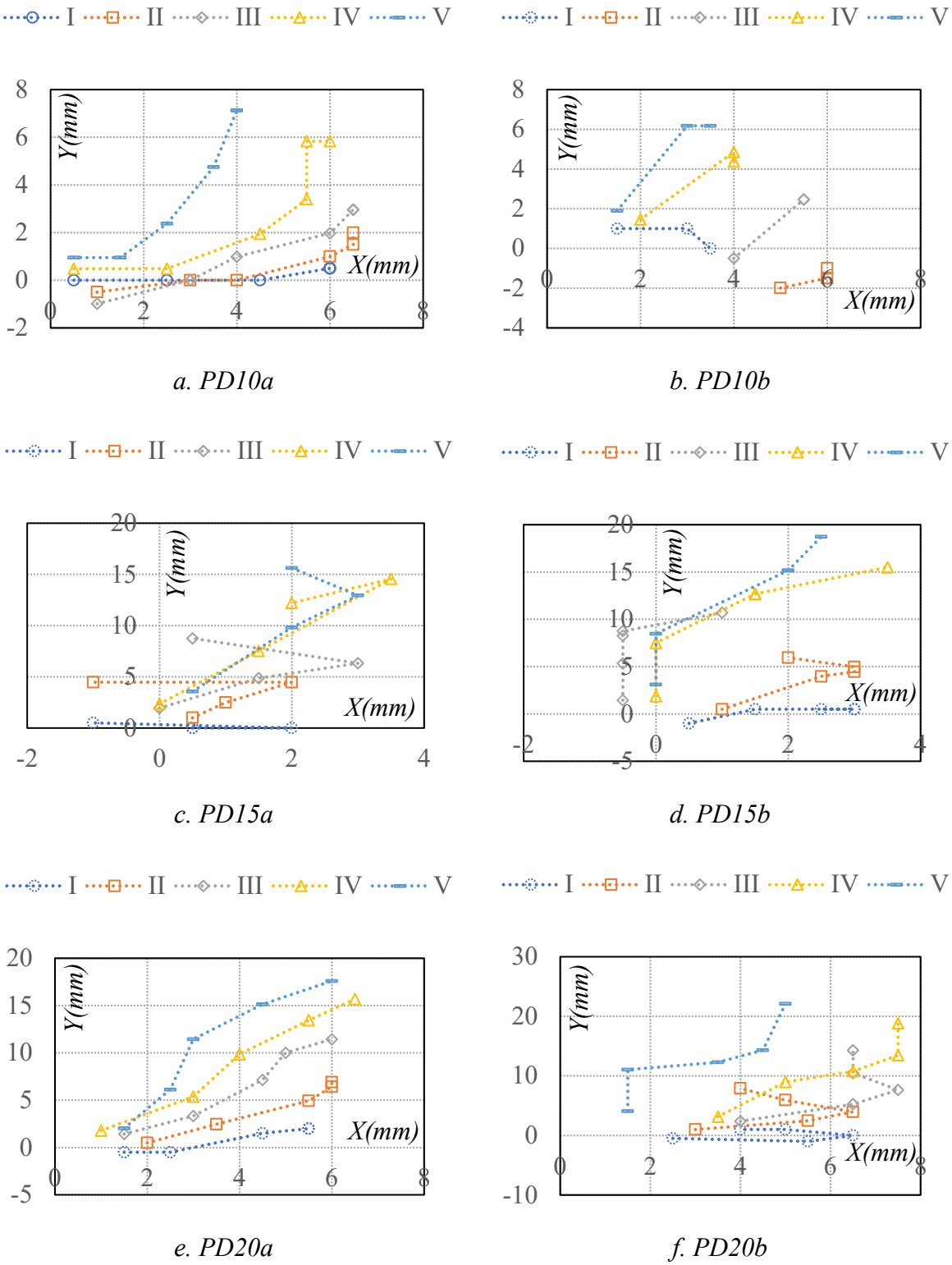

a. PD10a

b. PD10b

c. PD15a

d. PD15b

e. PD20a

f. PD20b

Figure 3.20 The history of slide in X and Y directions over six specimens

3.5 Summary

(a) The fabrication of low-rise 3D smooth curved surface by drawing the plane strips was confirmed. However, the establishment of high-rise 3D smooth curved surface by drawing the plane strips still had problem because of the occurrence of the wrinkling and the insufficient prestress.

(b) The slide between ETFE film and supporting galvanized steel arches was observed obviously. Therefore, the friction contact between them cannot be ignored.

(c) The relationship between the motion of offset point on ETFE film and the drawing values was established. This relationship can be used to predict the behaviors of ETFE film and determine the drawing values in the practical construction.

(d) The analytical method, which can solve the geometrical nonlinearity, the material nonlinearity and the nonlinearity of contact, is necessarily proposed. In addition, the static friction coefficient between the ETFE film and supporting frames such as galvanized steel arch is also essential to investigate.

Chapter 4.
Total Lagrangian formulation for ETFE tensile membrane structures considering friction contact

Chapter 4. Total Lagrangian formulation for ETFE tensile membrane structures considering friction contact

4.1 Introduction

First, the ETFE film is thin and flexible, so tensile membrane structures using ETFE film have relatively large deformation under specified loads. Thus, the geometrical nonlinearity analysis is essentially important. Second, the ETFE film is produced partial plastic elongation during the drawing process in the proposed fabrication method in Chapter 3. As a result, the elastic-plastic characteristics of ETFE film are necessarily considered. Third, the slide between ETFE film and supporting frames such as galvanized steel arches was observed obviously. It means that the friction contacts between ETFE film and supporting arches cannot be ignored. In summary, the analytical method, which can solve the geometrical nonlinearity, the material nonlinearity and the nonlinearity of contact, is necessarily proposed to predict the behaviors of ETFE film and determine the drawing values in the proposed stretch fabrication method.

The elastic-plastic large deformation analysis could be found in the work of Bathe [KB76]. In this work, Bathe suggested both total Lagrangian (TL) formulation, in which all kinematic variables are referred to the initial configuration and updated Lagrangian (UL) formulation, in which all kinematic variables are referred to the current configuration. Moreover, they indicated that if the constitutive relations are defined directly for each formulation, the differences between two formulations will be relatively small in case of moderate deformation. Besides, drawing the ETFE film was coupled with the reduction of thickness and the decrease of tear resistance. As a result, 10% to 20% of drawing was the optimal condition under uniaxial elongation [MK08], while 5% to 10% was recommended for the biaxial elongation [EJ13]. Therefore, the theory of large displacements and small strains could be utilized for the analysis during the stretch fabrication experiments. As a result, the TL formulation is used in this chapter.

The slide or friction contact in tensile membrane structures has attracted a great number of researchers. The review of this problem can be referred in section 1.1. The main problem in previous researches of this problem was the assumption of elastic range of membrane material.

Therefore, this chapter proposes the total Lagrangian formulation for both triangular membrane element and node-to-node contact element as well as the analytical procedure to solve the problems of large deformation, elastic-plastic and contact conditions. The elastic-plastic properties of material and the friction characteristics of contact surfaces are determined during the static loading process. In addition, the suggested formulations are simple and easily incorporated into existing nonlinear finite element programs. The accuracy and applicability of

suggesting method are confirmed by both the experiments and existing commercial software *ANSYS* [AN07].

4.2 Total Lagrangian formulation

In the static analysis of geometrical nonlinearity of tensile membrane structures, it is preferable to use a dense mesh of primitive elements rather than a coarse mesh made up higher order elements [BT92]. Therefore, the work of this chapter focuses on triangular membrane elements with three nodes and nine degrees of freedom per element. In addition, the dimensions of supporting frames are usually much smaller than that of membrane. As a result, the node-to-node contact elements are used to model the contact between the membrane and supporting frame approximately.

4.2.1. Triangular membrane element

The TL formulation for triangular element can be referred in many previous studies [BT92], [KI90], [HN95]. This formulation is reviewed in combination with Return-Mapping method [JCS86], consistent tangent operators [JCS85] for ETFE material, which has two yield points on its stress-strain curve in this section. The motion of triangular element in local Cartesian coordinate system (${}_0x,\ {}_0y,\ {}_0z$) of the initial time t_0 as well as in the global coordinate (*X, Y, Z*) is shown in Figure 4.1.

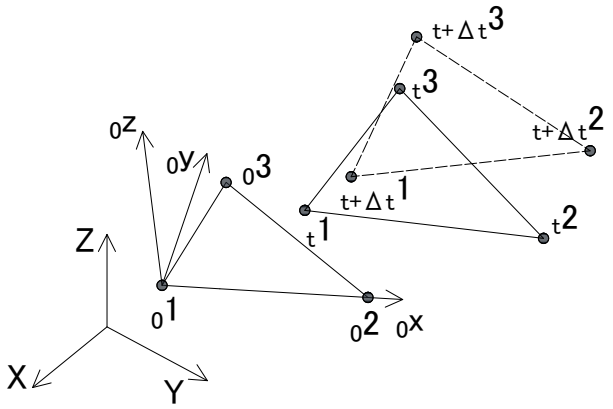

${}_0x,\ {}_0y,\ {}_0z$: the local coordinates of membrane element

X, Y, Z : the global coordinates of the whole structure

${}_0i,\ {}_ti,\ {}_{t+\Delta t}i$: the position of node *i* (*i=1→3*) at the pseudo time 0, t and $t+\Delta t$

Figure 4.1 The motion of triangular element in Cartesian coordinate system

The notations in this section are listed in Eq. (4.1)

${}^{t+\Delta t}_{0}u,\ {}^{t+\Delta t}_{0}v,\ {}^{t+\Delta t}_{0}w$	The displacements in membrane element from time t_0 to time $t+\Delta t$ in ${}_0x,\ {}_0y$ and ${}_0z$ coordinates.
${}^{t+\Delta t}_{0}u_i,\ {}^{t+\Delta t}_{0}v_i,\ {}^{t+\Delta t}_{0}w_i$	The displacements of node *i* (*i=1→3*) from time t_0 to time $t+\Delta t$ in ${}_0x,\ {}_0y$ and ${}_0z$ coordinates.
$\delta u_i, \delta v_i$ and δw_i	The variations of the current displacement components

(4.1)

	${}^{t+\Delta t}_{0}u_i$, ${}^{t+\Delta t}_{0}v_i$ and ${}^{t+\Delta t}_{0}w_i$
${}^{t+\Delta t}_{0}\varepsilon_{xx}$, ${}^{t+\Delta t}_{0}\varepsilon_{yy}$, ${}^{t+\Delta t}_{0}\varepsilon_{xy}$	The Green-Lagrange strains of membrane element from the initial time t_0 to the time $t+\Delta t$
${}^{t+\Delta t}_{0}S_{xx}$, ${}^{t+\Delta t}_{0}S_{yy}$, ${}^{t+\Delta t}_{0}S_{xy}$	The *2nd* Piola-Kirchhoff stresses of membrane element from the initial time t_0 to the time $t+\Delta t$
${}^{t}_{0}\bar{S}$, ${}^{t+\Delta t}_{0}\bar{S}$	The Mises stress of the time t and the time $t+\Delta t$
${}^{t}_{0}\boldsymbol{S}$, ${}^{t+\Delta t}_{0}\boldsymbol{S}$	The *2nd* Piola-Kirchhoff stress tensor of membrane element from time t_0 to time t and time $t+\Delta t$
${}^{t+\Delta t}_{0}\boldsymbol{S}^{trial}$	Trial values of *2nd* Piola-Kirchhoff stress tensor ${}^{t+\Delta t}_{0}\boldsymbol{S}$
${}^{t+\Delta t}_{0}\boldsymbol{S}^{true}$	True values of *2nd* Piola-Kirchhoff stress tensor ${}^{t+\Delta t}_{0}\boldsymbol{S}$
${}^{t+\Delta t}_{0}\boldsymbol{S}'$	The deviatoric values of *2nd* Piola-Kirchhoff stress tensor ${}^{t+\Delta t}_{0}\boldsymbol{S}$
$\boldsymbol{D}$	Elastic tensor of material
$\boldsymbol{D}^{ep*}$	Elastic-plastic tensor of material
$\Delta\bar{e}_P$	The increment of equivalent plastic strain from the time t to the time $t+\Delta t$
E, G, ν, H'	Young modulus, shear modulus, Poisson ratio, strain hardening ratio of material

The displacements ${}^{t+\Delta t}_{0}u$, ${}^{t+\Delta t}_{0}v$, ${}^{t+\Delta t}_{0}w$ are assumed to be linear over the element, so Eq. (4.2) can be determined as below:

$$\begin{aligned} {}^{t+\Delta t}_{0}u &= a_1 + a_2\,{}_0x + a_3\,{}_0y \\ {}^{t+\Delta t}_{0}v &= a_4 + a_5\,{}_0x + a_6\,{}_0y \\ {}^{t+\Delta t}_{0}w &= a_7 + a_8\,{}_0x + a_9\,{}_0y \end{aligned} \tag{4.2}$$

Evaluating the displacements of three nodes of element, and solving for a_i, Eq. (4.3) can be obtained:

$$\begin{aligned} a_2 &= \frac{{}_0y_{23}\,{}^{t+\Delta t}_{0}u_1 + {}_0y_{31}\,{}^{t+\Delta t}_{0}u_2 + {}_0y_{12}\,{}^{t+\Delta t}_{0}u_3}{2S_0} \\ a_3 &= \frac{{}_0x_{32}\,{}^{t+\Delta t}_{0}u_1 + {}_0x_{13}\,{}^{t+\Delta t}_{0}u_2 + {}_0x_{21}\,{}^{t+\Delta t}_{0}u_3}{2S_0} \\ a_5 &= \frac{{}_0y_{23}\,{}^{t+\Delta t}_{0}v_1 + {}_0y_{31}\,{}^{t+\Delta t}_{0}v_2 + {}_0y_{12}\,{}^{t+\Delta t}_{0}v_3}{2S_0} \\ a_6 &= \frac{{}_0x_{32}\,{}^{t+\Delta t}_{0}v_1 + {}_0x_{13}\,{}^{t+\Delta t}_{0}v_2 + {}_0x_{21}\,{}^{t+\Delta t}_{0}v_3}{2S_0} \\ a_8 &= \frac{{}_0y_{23}\,{}^{t+\Delta t}_{0}w_1 + {}_0y_{31}\,{}^{t+\Delta t}_{0}w_2 + {}_0y_{12}\,{}^{t+\Delta t}_{0}w_3}{2S_0} \end{aligned} \tag{4.3}$$

$$a_9 = \frac{{}_0x_{32}\,{}^{t+\Delta t}_{0}w_1 \;+\; {}_0x_{13}\,{}^{t+\Delta t}_{0}w_2 \;+\; {}_0x_{21}\,{}^{t+\Delta t}_{0}w_3}{2S_0}$$

where, the S_0 is the area of membrane element at the initial time t_0.

The values of S_0, ${}_0x_{ij}$ and ${}_0y_{ij}$ are determined in Eq. (4.4)

$$\begin{aligned} 2S_0 &= \begin{vmatrix} 1 & {}_0x_1 & {}_0y_1 \\ 1 & {}_0x_2 & {}_0y_2 \\ 1 & {}_0x_3 & {}_0y_3 \end{vmatrix} \\ {}_0x_{ij} &= {}_0x_i - {}_0x_j \quad (i,j = 1 \to 3) \\ {}_0y_{ij} &= {}_0y_i - {}_0y_j \quad (i,j = 1 \to 3) \end{aligned} \tag{4.4}$$

where, ${}_0x_i$ and ${}_0y_i$ are the coordinates of node i at time t_0 in ${}_0x$ and ${}_0y$ axes, respectively.

The Green-Lagrange strains from the initial time t_0 to the time $t+\Delta t$ can be expressed by Eq. (4.5)

$$\begin{aligned} {}^{t+\Delta t}_{0}\varepsilon_{xx} &= \frac{\partial\, {}^{t+\Delta t}_{0}u}{\partial\, {}_0x} + \frac{1}{2}\left[\left(\frac{\partial\, {}^{t+\Delta t}_{0}u}{\partial\, {}_0x}\right)^2 + \left(\frac{\partial\, {}^{t+\Delta t}_{0}v}{\partial\, {}_0x}\right)^2 + \left(\frac{\partial\, {}^{t+\Delta t}_{0}w}{\partial\, {}_0x}\right)^2\right] \\ {}^{t+\Delta t}_{0}\varepsilon_{yy} &= \frac{\partial\, {}^{t+\Delta t}_{0}v}{\partial\, {}_0y} + \frac{1}{2}\left[\left(\frac{\partial\, {}^{t+\Delta t}_{0}u}{\partial\, {}_0y}\right)^2 + \left(\frac{\partial\, {}^{t+\Delta t}_{0}v}{\partial\, {}_0y}\right)^2 + \left(\frac{\partial\, {}^{t+\Delta t}_{0}w}{\partial\, {}_0y}\right)^2\right] \\ {}^{t+\Delta t}_{0}\varepsilon_{xy} &= \frac{\partial\, {}^{t+\Delta t}_{0}u}{\partial\, {}_0y} + \frac{\partial\, {}^{t+\Delta t}_{0}v}{\partial\, {}_0x} + \left[\frac{\partial\, {}^{t+\Delta t}_{0}u}{\partial\, {}_0x}\frac{\partial\, {}^{t+\Delta t}_{0}u}{\partial\, {}_0y} + \frac{\partial\, {}^{t+\Delta t}_{0}v}{\partial\, {}_0x}\frac{\partial\, {}^{t+\Delta t}_{0}v}{\partial\, {}_0y} + \frac{\partial\, {}^{t+\Delta t}_{0}w}{\partial\, {}_0x}\frac{\partial\, {}^{t+\Delta t}_{0}w}{\partial\, {}_0y}\right] \end{aligned} \tag{4.5}$$

Substituting Eq. (4.2) and Eq. (4.3) into Eq. (4.5), and writing them in matrix form, Eq. (4.6) can be obtained:

$${}^{t+\Delta t}_{0}\boldsymbol{\varepsilon} = \begin{Bmatrix} {}^{t+\Delta t}_{0}\varepsilon_{xx} \\ {}^{t+\Delta t}_{0}\varepsilon_{yy} \\ {}^{t+\Delta t}_{0}\varepsilon_{xy} \end{Bmatrix} = \begin{Bmatrix} a_2 + \frac{1}{2}({a_2}^2 + {a_5}^2 + {a_8}^2) \\ a_6 + \frac{1}{2}({a_3}^2 + {a_6}^2 + {a_9}^2) \\ a_3 + a_5 + (a_2a_3 + a_5a_6 + a_8a_9) \end{Bmatrix} \tag{4.6}$$

The variations of these strains can be determined in Eq. (4.7):

$${}^{t+\Delta t}_{0}\delta\boldsymbol{\varepsilon} = \begin{Bmatrix} {}^{t+\Delta t}_{0}\delta\varepsilon_{xx} \\ {}^{t+\Delta t}_{0}\delta\varepsilon_{yy} \\ {}^{t+\Delta t}_{0}\delta\varepsilon_{xy} \end{Bmatrix} = (\boldsymbol{B}_0 + \boldsymbol{B}_L)\cdot\delta\boldsymbol{u} \tag{4.7}$$

where, the matrices $\boldsymbol{B}_0$, $\boldsymbol{B}_L$ and vector $\delta\boldsymbol{u}$ are determined in Eq. (4.8)

$$\boldsymbol{B}_0 = \frac{1}{2S_0}\begin{bmatrix} {}_0y_{23} & 0 & 0 & {}_0y_{31} & 0 & 0 & {}_0y_{12} & 0 & 0 \\ 0 & {}_0x_{32} & 0 & 0 & {}_0x_{13} & 0 & 0 & {}_0x_{21} & 0 \\ {}_0x_{32} & {}_0y_{23} & 0 & {}_0x_{13} & {}_0y_{31} & 0 & {}_0x_{21} & {}_0y_{12} & 0 \end{bmatrix} \tag{4.8}$$

$$\boldsymbol{B}_L = \frac{1}{2S_0}\begin{bmatrix} a_{2\ 0}y_{23} & a_{5\ 0}y_{23} & a_{8\ 0}y_{23} & a_{2\ 0}y_{31} & a_{5\ 0}y_{31} & a_{8\ 0}y_{31} & a_{2\ 0}y_{12} & a_{5\ 0}y_{12} & a_{8\ 0}y_{12} \\ a_{3\ 0}x_{32} & a_{6\ 0}x_{32} & a_{9\ 0}x_{32} & a_{3\ 0}x_{13} & a_{6\ 0}x_{13} & a_{9\ 0}x_{13} & a_{3\ 0}x_{21} & a_{6\ 0}x_{21} & a_{9\ 0}x_{21} \\ a_{3\ 0}y_{23} & a_{6\ 0}y_{23} & a_{9\ 0}y_{23} & a_{3\ 0}y_{31} & a_{6\ 0}y_{31} & a_{9\ 0}y_{31} & a_{3\ 0}y_{12} & a_{6\ 0}y_{12} & a_{9\ 0}y_{12} \\ +a_{2\ 0}x_{32} & +a_{5\ 0}x_{32} & +a_{8\ 0}x_{32} & +a_{2\ 0}x_{13} & +a_{5\ 0}x_{13} & +a_{8\ 0}x_{13} & +a_{2\ 0}x_{21} & +a_{5\ 0}x_{21} & +a_{8\ 0}x_{21} \end{bmatrix}$$

$$\boldsymbol{\delta u} = [\delta u_1\ \delta v_1\ \delta w_1\ \delta u_2\ \delta v_2\ \delta w_2\ \delta u_3\ \delta v_2\ \delta w_3]^T$$

where, $\delta u_i, \delta v_i$ and δw_i are the variations of the current displacements ${}^{t+\Delta t}_{0}u_i$, ${}^{t+\Delta t}_{0}v_i$ and ${}^{t+\Delta t}_{0}w_i$, respectively. It should be noted that these variations are also the variations of the increment of displacements from the time t to the time $t+\Delta t$.

For an elastic-plastic material, the constitutive equations depend on the complete stress and strain history. In this section work, von Mises yield criterion is used, and the equivalent stress or Mises stress at the time t is determined in Eq. (4.9)

$${}^{t}_{0}\bar{S} = \sqrt{({}^{t}_{0}S_{xx})^2 + \left({}^{t}_{0}S_{yy}\right)^2 - {}^{t}_{0}S_{xx}\,{}^{t}_{0}S_{yy} + 3\left({}^{t}_{0}S_{xy}\right)^2} \tag{4.9}$$

The elastic-plastic status of material at any time between discrete time points t and $t+\Delta t$ is defined by this equivalent stress and yield stresses of material in uniaxial tension test. As a result, the constitutive equations for elastic-plastic material in *TL* formulation are written in Eq. (4.10)

$$\begin{gathered} {}^{t+\Delta t}_{0}\boldsymbol{S} = {}^{t}_{0}\boldsymbol{S} + \bar{\boldsymbol{D}} \cdot \Delta\boldsymbol{\varepsilon} \\ \Delta\boldsymbol{\varepsilon} = {}^{t+\Delta t}_{0}\boldsymbol{\varepsilon} - {}^{t}_{0}\boldsymbol{\varepsilon} \\ \bar{\boldsymbol{D}} = \boldsymbol{D} = \frac{E}{1-\nu^2}\begin{bmatrix} 1 & \nu & 0 \\ \nu & 1 & 0 \\ 0 & 0 & \frac{1-\nu}{2} \end{bmatrix} \text{ : elastic zone} \\ \bar{\boldsymbol{D}} = \boldsymbol{D}^{ep*} \qquad\qquad \text{: plastic zone} \end{gathered} \tag{4.10}$$

where, $\Delta\boldsymbol{\varepsilon}$ are the increments of Green-Lagrange strains from the time t to the time $t+\Delta t$, $\boldsymbol{D}$ is elastic tensor of material, $\boldsymbol{D}^{ep*}$ is elastic-plastic tensor of material.

The von Mises yield criterion, the associated flow rule and the isotropic hardening rule are used to determine $\boldsymbol{D}^{ep*}$. The Return-Mapping method and consistent tangent operators could be used to obtain $\boldsymbol{D}^{ep*}$ for the assumption of plane stress analysis in this chapter. The derivation of $\boldsymbol{D}^{ep*}$ for triangular element is given in the next part.

Derivation of $\boldsymbol{D}^{ep*}$:

When the material shows the plastic behavior at any time between discrete time points t and $t+\Delta t$, the *2nd* Piola-Kirchhoff stress tensor at time $t+\Delta t$ is obtained by Eq. (4.11)

$${}^{t+\Delta t}_{0}\mathbf{S} = {}^{t}_{0}\boldsymbol{S} + \boldsymbol{D} \cdot (\Delta\boldsymbol{\varepsilon} - \Delta\boldsymbol{\varepsilon}^P) \tag{4.11}$$

where, $\Delta\boldsymbol{\varepsilon}^p$ are the increments of plastic strains from time t to time $t+\Delta t$.

Based on the associated flow rule and the yield condition, $\Delta\boldsymbol{\varepsilon}^p$ are determined in Eq. (4.12)

$$\Delta\boldsymbol{\varepsilon}^P = \Delta\lambda \cdot {}^{t+\Delta t}_{0}\boldsymbol{S}' \tag{4.12}$$

$$\Delta\lambda = \frac{3}{2}\frac{\Delta\bar{e}_P}{{}^{t+\Delta t}_{0}\bar{S}}$$

where, $\Delta\bar{e}_P$ is the increment of equivalent plastic strain from time t to time $t+\Delta t$, ${}^{t+\Delta t}_{0}\bar{S}$ is the equivalent stress or Mises stress at the time $t+\Delta t$, and ${}^{t+\Delta t}_{0}\boldsymbol{S}'$ is the deviatoric stress tensor of *2nd* Piola-Kirchhoff stress tensor.

Substituting Eq. (4.12) into Eq. (4.11), the equation Eq. (4.13) can be obtained

$${}^{t+\Delta t}_{0}\boldsymbol{S} = {}^{t}_{0}\boldsymbol{S} + \boldsymbol{D}\cdot\Delta\boldsymbol{\varepsilon} - \frac{3}{2}\frac{\Delta\bar{e}_P}{{}^{t+\Delta t}_{0}\bar{S}}\boldsymbol{D}\cdot{}^{t+\Delta t}_{0}\boldsymbol{S}' \tag{4.13}$$

The trial values of *2nd* Piola-Kirchhoff stress tensor at time $t+\Delta t$ are determined in Eq. (4.14), and the true values of *2nd* Piola-Kirchhoff stress tensor at time $t+\Delta t$ are rewritten in Eq. (4.15) from Eq. (4.13).

$${}^{t+\Delta t}_{0}\boldsymbol{S}^{trial} = {}^{t}_{0}\boldsymbol{S} + \boldsymbol{D}\cdot\Delta\boldsymbol{\varepsilon} \tag{4.14}$$

$${}^{t+\Delta t}_{0}\boldsymbol{S}^{true} = {}^{t+\Delta t}_{0}\boldsymbol{S}^{trial} - \frac{3}{2}\frac{\Delta\bar{e}_P}{{}^{t+\Delta t}_{0}\bar{S}}\boldsymbol{D}\cdot{}^{t+\Delta t}_{0}\boldsymbol{S}'^{true} \tag{4.15}$$

The deviatoric values of *2nd* Piola-Kirchhoff stress tensor ${}^{t+\Delta t}_{0}\boldsymbol{S}'^{true}$ are defined in Eq. (4.16) for the plane stress analysis

$${}^{t+\Delta t}_{0}\boldsymbol{S}'^{true} = \boldsymbol{P}\cdot{}^{t+\Delta t}_{0}\boldsymbol{S}^{true} \tag{4.16}$$

where, $\boldsymbol{P} = \begin{bmatrix} \frac{2}{3} & -\frac{1}{3} & 0 \\ -\frac{1}{3} & \frac{2}{3} & 0 \\ 0 & 0 & 2 \end{bmatrix}$.

Introducing matrix $\boldsymbol{Q}$ as $\boldsymbol{Q} = \frac{1}{\sqrt{2}}\begin{bmatrix} 1 & -1 & 0 \\ 1 & 1 & 0 \\ 0 & 0 & \sqrt{2} \end{bmatrix}$ and multiplying $\boldsymbol{Q}^T$ in the left side of Eq. (4.15), the equation Eq. (4.17) can be obtained

$$\begin{aligned} {}^{t+\Delta t}_{0}\widehat{\boldsymbol{S}}^{true} &= {}^{t+\Delta t}_{0}\widehat{\boldsymbol{S}}^{trial} - \frac{3}{2}\frac{\Delta\bar{e}_P}{{}^{t+\Delta t}_{0}\bar{S}}\boldsymbol{Q}^T\cdot\boldsymbol{D}\cdot\boldsymbol{P}\cdot{}^{t+\Delta t}_{0}\boldsymbol{S}^{true} \\ {}^{t+\Delta t}_{0}\widehat{\boldsymbol{S}}^{true} &= {}^{t+\Delta t}_{0}\widehat{\boldsymbol{S}}^{trial} - \frac{3}{2}\frac{\Delta\bar{e}_P}{{}^{t+\Delta t}_{0}\bar{S}}\boldsymbol{Q}^T\cdot\boldsymbol{D}\cdot\boldsymbol{Q}\cdot\boldsymbol{Q}^T\cdot\boldsymbol{P}\cdot\boldsymbol{Q}\cdot\boldsymbol{Q}^T\cdot{}^{t+\Delta t}_{0}\boldsymbol{S}^{true} \\ {}^{t+\Delta t}_{0}\widehat{\boldsymbol{S}}^{true} &= {}^{t+\Delta t}_{0}\widehat{\boldsymbol{S}}^{trial} - \frac{3}{2}\frac{\Delta\bar{e}_P}{{}^{t+\Delta t}_{0}\bar{S}}\widehat{\boldsymbol{D}}\cdot{}^{t+\Delta t}_{0}\widehat{\boldsymbol{S}}^{true} \end{aligned} \tag{4.17}$$

where, ${}^{t+\Delta t}_{0}\widehat{\boldsymbol{S}} = \boldsymbol{Q}^T\cdot{}^{t+\Delta t}_{0}\boldsymbol{S}$, $\widehat{\boldsymbol{D}} = \boldsymbol{Q}^T\cdot\boldsymbol{D}\cdot\boldsymbol{Q}\cdot\boldsymbol{Q}^T\cdot\boldsymbol{P}\cdot\boldsymbol{Q} = \begin{bmatrix} \frac{E}{3(1-\nu)} & 0 & 0 \\ 0 & 2G & 0 \\ 0 & 0 & 2G \end{bmatrix}$, and $G = \frac{E}{2(1+\nu)}$

Eq. (4.17) can be written in scalar forms in Eq. (4.18)

$$\left(1+\frac{1}{2}\frac{\Delta\bar{e}_P}{{}^{t+\Delta t}_{0}\bar{S}}\frac{E}{(1-\nu)}\right){}^{t+\Delta t}_{0}\hat{S}^{true}_{xx} = {}^{t+\Delta t}_{0}\hat{S}^{trial}_{xx}$$
$$\left(1+3\frac{\Delta\bar{e}_P}{{}^{t+\Delta t}_{0}\bar{S}}G\right){}^{t+\Delta t}_{0}\hat{S}^{true}_{yy} = {}^{t+\Delta t}_{0}\hat{S}^{trial}_{yy} \tag{4.18}$$
$$\left(1+3\frac{\Delta\bar{e}_P}{{}^{t+\Delta t}_{0}\bar{S}}G\right){}^{t+\Delta t}_{0}\hat{S}^{true}_{xy} = {}^{t+\Delta t}_{0}\hat{S}^{trial}_{xy}$$

The von Mises yield criterion is used to obtain Eq. (4.19)

$$\frac{1}{2}\left(\frac{{}^{t+\Delta t}_{0}\hat{S}^{trial}_{xx}}{1+\frac{1}{2}\frac{\Delta\bar{e}_P}{{}^{t+\Delta t}_{0}\bar{S}}\frac{E}{(1-\nu)}}\right)^2+\frac{3}{2}\left(\frac{{}^{t+\Delta t}_{0}\hat{S}^{trial}_{yy}}{1+3\frac{\Delta\bar{e}_P}{{}^{t+\Delta t}_{0}\bar{S}}G}\right)^2+3\left(\frac{{}^{t+\Delta t}_{0}\hat{S}^{trial}_{xy}}{1+3\frac{\Delta\bar{e}_P}{{}^{t+\Delta t}_{0}\bar{S}}G}\right)^2 \tag{4.19}$$
$$=\left({}^{t+\Delta t}_{0}\bar{S}_y\right)^2$$

where, ${}^{t+\Delta t}_{0}\bar{S}_y$ is the yield stress at the time $t+\Delta t$ and is defined by the hardening rule in Eq. (4.20)

$${}^{t+\Delta t}_{0}\bar{S}_y = {}^{t}_{0}\bar{S}_y + H'\Delta\bar{e}_P \tag{4.20}$$

where, H' is strain hardening ratio of material.

The Newton-Raphson method is used to obtain the solutions of $\Delta\bar{e}_P$ and ${}^{t+\Delta t}_{0}\bar{S}$ in Eq. (4.19). The consistent stiffness matrix can be determined in Eq. (4.21)

$$\boldsymbol{D}^{ep*} = \boldsymbol{D}^{*} - \frac{\left(\boldsymbol{D}^{*}:{}^{t+\Delta t}_{0}\boldsymbol{S}'^{true}\right)\otimes\left(\boldsymbol{D}^{*}:{}^{t+\Delta t}_{0}\boldsymbol{S}'^{true}\right)}{{}^{t+\Delta t}_{0}\boldsymbol{S}'^{true}:\left(\boldsymbol{D}^{*}:{}^{t+\Delta t}_{0}\boldsymbol{S}'^{true}\right)+\frac{4}{9}\gamma H'({}^{t+\Delta t}_{0}\bar{S})^2} \tag{4.21}$$

where, $\boldsymbol{D}^{*} = (\boldsymbol{D}^{-1}+\Delta\lambda\boldsymbol{P})^{-1}$ and $\gamma = \left(1-\frac{2}{3}H'\Delta\lambda\right)^{-1}$

4.2.2. Node-to-node contact element

Figure 4.2 describes node-to-node contact element in its local coordinate $({}_0x,\ {}_0y,\ {}_0z)$ at the initial time t_0. The system of three springs are used to model this element. The k_n is the stiffness of normal spring, while k_t is the stiffness of two horizontal springs. Node *M* shows the rigid body as a master body, while node *S* indicates the flexible body as slave body. In this work, the normal contact direction is assumed from node *M* to node *S* as ${}_0z$ axis.

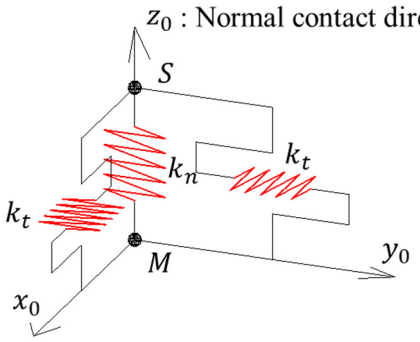

Figure 4.2 The description of node-to-node contact element

Assumption 1: *The normal contact direction remains constant during the motion of slave body.*

The advantage of this assumption is to reduce the variation of the change of normal direction in analysis of large deformation. However, this assumption can only consider the small slide between two contact bodies.

Assumption 2: *At the initial time t_0 the normal contact conditions as shown in Eq. (1.1) are satisfied, and the TL formulation in this section will be established to solve the friction contact conditions.*

At the initial time t_0, the contact status between two bodies can be defined by the normal gap function in Eq. (4.22)

$$g_n = {}_0z_S - {}_0z_M \geq 0 \tag{4.22}$$

where, ${}_0z_S$ and ${}_0z_M$ are the coordinates of nodes *S* and *M* in ${}_0z$ axis, respectively, g_n is the distance between two bodies in normal direction.

When g_n is larger than zeros, two bodies are not in contact, and it is not necessary to have further discussion about this status. In contrast, the normal contact occurs, and the next *TL* formulations are established for this case.

The incremental step-by-step solution is used to deal with the analysis includes nonlinear geometric, elastic-plastic material and boundary contact conditions. The basic approach in this solution is to assume that the solution for the discrete time t is known and the solution for discrete time $t + \Delta t$ is required. Therefore, the next *TL* formulations for node-to-node contact

elements are constructed to find the solution at time $t + \Delta t$.

The notations in this section are listed in Eq. (4.23)

${}^{t}_{0}f_{gx}, {}^{t}_{0}f_{gy}, {}^{t}_{0}f_{gz}$	The internal contact forces of node-to-node contact element at the time t in ${}_0x, {}_0y, {}_0z$ coordinates.
${}^{t+\Delta t}_{0}f_{gx}, {}^{t+\Delta t}_{0}f_{gy}, {}^{t+\Delta t}_{0}f_{gz}$	The internal contact forces of node-to-node contact element at the time $t + \Delta t$ in ${}_0x, {}_0y, {}_0z$ coordinates.
${}^{t}_{0}u_{g}, {}^{t}_{0}v_{g}, {}^{t}_{0}w_{g}$	The deformations of node-to-node contact element at the time t in ${}_0x, {}_0y, {}_0z$ coordinates.
${}^{t+\Delta t}_{0}u_{g}, {}^{t+\Delta t}_{0}v_{g}, {}^{t+\Delta t}_{0}w_{g}$	The deformations of node-to-node contact element at the time $t + \Delta t$ in ${}_0x, {}_0y, {}_0z$ coordinates.
$\Delta u_g, \Delta v_g, \Delta w_g$	The increments of deformations of node-to-node contact element from the time t to time $t + \Delta t$
${}^{t}_{0}u_{i}, {}^{t}_{0}v_{i}, {}^{t}_{0}w_{i}$	The displacements of node *i (i=S, M)* from time t_0 to time t in ${}_0x, {}_0y, {}_0z$ coordinates.
${}^{t+\Delta t}_{0}u_{i}, {}^{t+\Delta t}_{0}v_{i}, {}^{t+\Delta t}_{0}w_{i}$	The displacements of node *i (i=S, M)* from time t_0 to time $t + \Delta t$ in ${}_0x, {}_0y, {}_0z$ coordinates.

(4.23)

The relations between the deformations of node-to-node contact element and the displacements of nodes of this element are shown in Eq. (4.24)

$$\begin{aligned} {}^{t+\Delta t}_{0}u_g &= {}^{t+\Delta t}_{0}u_S - {}^{t+\Delta t}_{0}u_M = {}^{t}_{0}u_g + \Delta u_g \\ {}^{t+\Delta t}_{0}v_g &= {}^{t+\Delta t}_{0}v_S - {}^{t+\Delta t}_{0}v_M = {}^{t}_{0}v_g + \Delta v_g \\ {}^{t+\Delta t}_{0}w_g &= {}^{t+\Delta t}_{0}w_S - {}^{t+\Delta t}_{0}w_M = {}^{t}_{0}w_g + \Delta w_g \end{aligned} \tag{4.24}$$

It should be noted that the penalty method is used in this work. As a result, the small penetration in normal direction between two contact bodies are permitted during the static loading process. The *Assumption 1* guarantees that this penetration will be increased during the static loading process. Therefore, the condition in Eq. (4.25) must be satisfied during the loading process.

$$\Delta w_g \leq 0 \tag{4.25}$$

Assumption 3: *The stick-slide status of node-to-node contact element at any time between discrete time points t and $t + \Delta t$ is determined by the internal contact forces at time t.*

The Coulomb dry friction theory is used in this work, so the condition in Eq. (4.26) is checked during the static loading process

$$\sqrt{\left({}^{t}_{0}f_{gx}\right)^2 + \left({}^{t}_{0}f_{gy}\right)^2} < \mu \left| {}^{t}_{0}f_{gz} \right| \tag{4.26}$$

where, μ is the static friction coefficient between two contact bodies.

If the condition in Eq. (4.26) is satisfied, the stick condition is used to predict the behavior of node-to-node element at the time $t + \Delta t$. The internal contact forces of this element at time $t + \Delta t$ can be obtained via the penalty method as shown in Eq. (4.27)

$$\begin{aligned} {}^{t+\Delta t}_{0}f_{gx} &= {}^{t}_{0}f_{gx} + k_n \cdot \Delta u_g \\ {}^{t+\Delta t}_{0}f_{gy} &= {}^{t}_{0}f_{gy} + k_t \cdot \Delta v_g \\ {}^{t+\Delta t}_{0}f_{gz} &= {}^{t}_{0}f_{gz} + k_t \cdot \Delta w_g \end{aligned} \tag{4.27}$$

The large values of penalty parameters k_n and k_t will make the values of increments of deformation small enough to be ignored.

If the condition in Eq. (4.26) is violated, the slide condition is adapted to predict the behavior of node-to-node element at time $t + \Delta t$. Figure 4.3 presents the motion of slave node from the time t to the time $t + \Delta t$.

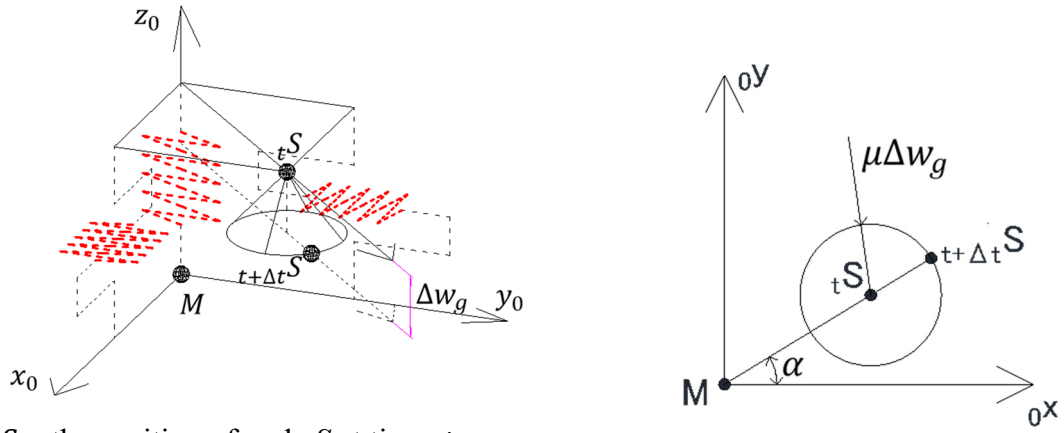

$_tS$: the position of node S at time t

$_{t+\Delta t}S$: the position of node S at time $t + \Delta t$

a. 3D view *b. Plane view*

Figure 4.3 The motion of slave node at time $t + \Delta t$

Assumption 4: *The motion of slave node at the time $t + \Delta t$ is determined by two criteria as shown in Figure 4.3. The first is that the sliding direction is defined by the friction forces at time t. The second criterion is that the Coulomb dry friction theory will be guaranteed. It means that node S will be in the circle with radius of $\mu\Delta w_g$.*

The sliding direction is determined in Eq. (4.28)

$$cos\alpha = \frac{{}^{t}_{0}f_{gx}}{\sqrt{\left({}^{t}_{0}f_{gx}\right)^2 + \left({}^{t}_{0}f_{gy}\right)^2}}, \quad sin\alpha = \frac{{}^{t}_{0}f_{gy}}{\sqrt{\left({}^{t}_{0}f_{gx}\right)^2 + \left({}^{t}_{0}f_{gy}\right)^2}} \tag{4.28}$$

The internal contact forces of this element at time $t + \Delta t$ can be obtained in Eq. (4.29)

$$\begin{aligned} {}^{t+\Delta t}_{0}f_{gx} &= {}^{t}_{0}f_{gx} + \mu \cdot cos\alpha \cdot k_n \cdot \Delta w_g \\ {}^{t+\Delta t}_{0}f_{gy} &= {}^{t}_{0}f_{gy} + \mu \cdot sin\alpha \cdot k_n \cdot \Delta w_g \\ {}^{t+\Delta t}_{0}f_{gz} &= {}^{t}_{0}f_{gz} + k_n \cdot \Delta w_g \end{aligned} \tag{4.29}$$

The derivation of Eq. (4.29) is shown in Box 4.1

Box 4.1

The friction force at time $t+\Delta t$ is determined in Eq. (a) by the Coulomb dry friction theory

$$ {}^{t+\Delta t}_{0}f_{gs} = \mu\, {}^{t+\Delta t}_{0}f_{gz} \tag{a} $$

The normal contact force at time $t+\Delta t$ is determined via penalty method as

$$ {}^{t+\Delta t}_{0}f_{gz} = {}^{t}_{0}f_{gz} + k_n \cdot \Delta w_g \tag{b} $$

Substituting Eq. (b) into Eq. (a), Eq. (c) can be obtained

$$ {}^{t+\Delta t}_{0}f_{gs} = \mu\left({}^{t}_{0}f_{gz} + k_n \cdot \Delta w_g\right) \tag{c} $$

The distributions of ${}^{t+\Delta t}_{0}f_{gs}$ into ${}_0x$, ${}_0y$ directions are obtained via *Assumption 4*

$$ \begin{aligned} {}^{t+\Delta t}_{0}f_{gx} &= cos\alpha \cdot {}^{t+\Delta t}_{0}f_{gs} = cos\alpha \cdot \mu({}^{t}_{0}f_{gz} + k_n \cdot \Delta w_g) \\ {}^{t+\Delta t}_{0}f_{gy} &= sin\alpha \cdot {}^{t+\Delta t}_{0}f_{gs} = sin\alpha \cdot \mu\left({}^{t}_{0}f_{gz} + k_n \cdot \Delta w_g\right) \end{aligned} \tag{d} $$

Substituting Eq. (4.28) into Eq. (d), Eq. (e) can be determined

$$ \begin{aligned} {}^{t+\Delta t}_{0}f_{gx} &= \frac{{}^{t}_{0}f_{gx}}{\sqrt{\left({}^{t}_{0}f_{gx}\right)^2 + \left({}^{t}_{0}f_{gy}\right)^2}}\mu\, {}^{t}_{0}f_{gz} + \mu \cdot cos\alpha \cdot k_n \cdot \Delta w_g \\ {}^{t+\Delta t}_{0}f_{gy} &= \frac{{}^{t}_{0}f_{gy}}{\sqrt{\left({}^{t}_{0}f_{gx}\right)^2 + \left({}^{t}_{0}f_{gy}\right)^2}}\mu\, {}^{t}_{0}f_{gz} + \mu \cdot sin\alpha \cdot k_n \cdot \Delta w_g \end{aligned} \tag{e} $$

Eq. (e) can be obtained if and only if the condition in Eq. (4.26) is violated. Assuming Eq. (f) is obtained at the time t.

$$ \sqrt{\left({}^{t}_{0}f_{gx}\right)^2 + \left({}^{t}_{0}f_{gy}\right)^2} = \mu\left|{}^{t}_{0}f_{gz}\right| \tag{f} $$

Substituting Eq. (f) into Eq. (e), the equation Eq. (4.29) can be determined.

***Physical view point*:** The stick-slip phenomenon will occur during the static loading process within the assumptions of this work. The stick-slide phenomenon can be observed from the macro experiments *[MO73]* to the micro experiments of friction contact *[AS04]*.

***Mathematical view point*:** the solution of Eq. (4.29) will be the correction for the assumption of Eq. (f) in Box 4.1. The overview of this correction is shown in Figure 4.4. During the static loading process, the normal contact force f_{gz} increase gradually. At the time t_i when the friction force ${}^{t_i}_{0}f_{gs}$ is larger than $\mu\left|{}^{t_i}_{0}f_{gz}\right|$, the slide occurs. The next solution is to correct the values of ${}^{t_i}_{0}f_{gs}$ to the yield surface at time t_i. This correction will be stopped when the correction of friction force ${}^{t_j}_{0}f_{gs}$ at time $t_j > t_i$ is smaller than the yield of $\mu\left|{}^{t_j}_{0}f_{gz}\right|$. At this time t_j the stick status is adapted, and the friction forces will be updated via the penalty values as shown in Eq. (4.27). This procedure will be repeated until the static loading process finishes.

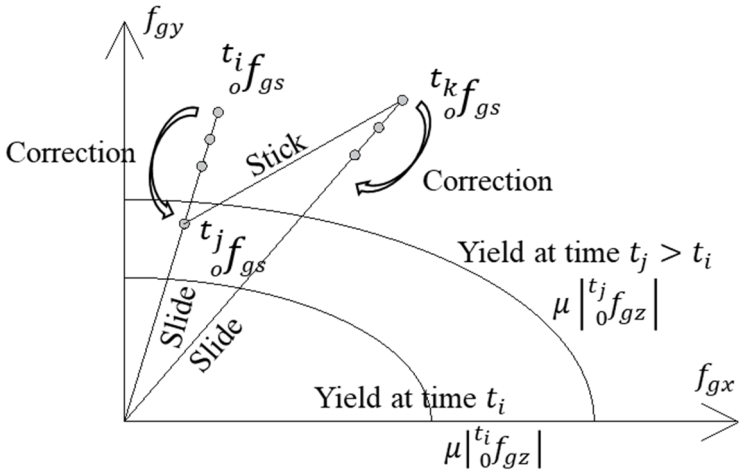

Figure 4.4 The overview of correction in slide status

Generally, writing Eq. (4.27) and Eq. (4.29) in matrix form, Eq. (4.30) can be obtained

$$ {}^{t+\Delta t}_{0}\boldsymbol{f}_g = {}^{t}_{0}\boldsymbol{f}_g + \boldsymbol{k}_g \cdot \Delta \boldsymbol{u}_g \tag{4.30}$$

where, ${}^{t+\Delta t}_{0}\boldsymbol{f}_g = \left[{}^{t+\Delta t}_{0}f_{gx} \;\; {}^{t+\Delta t}_{0}f_{gy} \;\; {}^{t+\Delta t}_{0}f_{gz} \right]^T$, ${}^{t}_{0}\boldsymbol{f}_g = \left[{}^{t}_{0}f_{gx} \;\; {}^{t}_{0}f_{gy} \;\; {}^{t}_{0}f_{gz} \right]^T$, $\Delta \boldsymbol{u}_g = [\Delta u_g \quad \Delta v_g \quad \Delta w_g]^T$, and $\boldsymbol{k}_g$ is defined in Eq. (4.31)

$$\begin{aligned} \boldsymbol{k}_g &= \begin{bmatrix} k_t & 0 & 0 \\ 0 & k_t & 0 \\ 0 & 0 & k_n \end{bmatrix} && \text{if } \sqrt{\left({}^{t}_{0}f_{gx}\right)^2 + \left({}^{t}_{0}f_{gy}\right)^2} < \mu \left| {}^{t}_{0}f_{gz} \right| \\ \boldsymbol{k}_g &= \boldsymbol{T}_g{}^T \cdot \begin{bmatrix} 0 & 0 & \mu k_n \\ 0 & 0 & 0 \\ 0 & 0 & k_n \end{bmatrix} \cdot \boldsymbol{T}_g && \text{if } \sqrt{\left({}^{t}_{0}f_{gx}\right)^2 + \left({}^{t}_{0}f_{gy}\right)^2} \geq \mu \left| {}^{t}_{0}f_{gz} \right| \end{aligned} \tag{4.31}$$

where, $\boldsymbol{T}_g = \begin{bmatrix} cos\alpha & sin\alpha & 0 \\ -sin\alpha & cos\alpha & 0 \\ 0 & 0 & 1 \end{bmatrix}$ is defined as the transformation matrix to coordinate at time t_0.

It should be noted that the increments of Δu_g, Δv_g, Δw_g will be determined in the equilibrium of the whole structure.

4.2.3. Structure includes triangular membrane and node-to-node contact elements

The principle of virtual work for structure which includes triangular element and node-to-node element at the time $t+\Delta t$ can be expressed generally as below

$$\int_{{}_0V} \delta {}^{t+\Delta t}_{0}\boldsymbol{\varepsilon}^T \cdot {}^{t+\Delta t}_{0}\boldsymbol{S} \cdot d\ {}_0V + \delta {}^{t+\Delta t}_{0}\boldsymbol{u}_g^{\ T} \cdot {}^{t+\Delta t}_{0}\boldsymbol{f}_g - \delta {}^{t+\Delta t}_{0}\boldsymbol{U}^T \cdot {}^{t+\Delta t}\boldsymbol{R} = 0 \tag{4.32}$$

where, ${}^{t+\Delta t}_{0}\boldsymbol{U}$ is the nodal displacements vector of the whole structure from the time t_0 to the time $t+\Delta t$, ${}^{t+\Delta t}\boldsymbol{R}$ is the external nodal forces vector at the time $t+\Delta t$, and ${}_0V$ is the volume of membrane element at the time t_0.

Substituting Eq. (4.7) into Eq. (4.32), and eliminating $\delta {}^{t+\Delta t}_{0}\boldsymbol{U}^T$, the equation Eq. (4.33) can be obtained below

$$\boldsymbol{M}^T \cdot \int_{{}_0V} (\boldsymbol{B}_0 + \boldsymbol{B}_L)^T \cdot {}^{t+\Delta t}_{0}\boldsymbol{S} \cdot d\ {}_0V + \boldsymbol{G}^T \cdot {}^{t+\Delta t}_{0}\boldsymbol{f}_g - {}^{t+\Delta t}\boldsymbol{R} = 0 \tag{4.33}$$

where, $\boldsymbol{M}$ or $\boldsymbol{G}$ matrices show the relation between nodal displacements vector of whole structure and nodal displacements vector of membrane elements or node-to-node elements. These matrices can be easily obtained in specific problem.

The Newton-Raphson method can be used to obtain the solution of Eq. (4.33). The residual forces after *i*th iteration are shown in Eq. (4.34)

$$\boldsymbol{\Phi}^i = \boldsymbol{M}^T \cdot \int_{{}_0V} (\boldsymbol{B}_0 + \boldsymbol{B}_L^i)^T \cdot {}^{t+\Delta t}_{0}\boldsymbol{S}^i \cdot d\ {}_0V + \boldsymbol{G}^T \cdot {}^{t+\Delta t}_{0}\boldsymbol{f}_g^i - {}^{t+\Delta t}\boldsymbol{R} \tag{4.34}$$

For the next step which is expected to yield the exact solution, Eq. (4.35) can be obtained

$$\boldsymbol{\Phi}^{i+1} \cong \boldsymbol{\Phi}^i + \frac{\partial \boldsymbol{\Phi}^i}{\partial {}^{t+\Delta t}_{0}\boldsymbol{U}} \cdot \Delta \boldsymbol{U}^i = \boldsymbol{0} \tag{4.35}$$

The solution of Eq. (4.35) is the incremental displacements $\Delta \boldsymbol{U}^i$, and the displacements at (i+1)*th* iteration can be determined in Eq. (4.36)

$$\begin{aligned} {}^{t+\Delta t}_{0}\boldsymbol{U}^{i+1} &= {}^{t+\Delta t}_{0}\boldsymbol{U}^i + \Delta \boldsymbol{U}^i \\ {}^{t+\Delta t}_{0}\boldsymbol{U}^0 &= {}^{t}_{0}\boldsymbol{U} \end{aligned} \tag{4.36}$$

where, ${}^{t}_{0}\boldsymbol{U}$ is the nodal displacements vector of the whole structure from the time t_0 to the time t. In Eq. (4.35), the tangent stiffness matrix $\frac{\partial \boldsymbol{\Phi}^i}{\partial {}^{t+\Delta t}_{0}\boldsymbol{U}}$ consists of three parts as follows

$$\begin{aligned} \boldsymbol{K}_{me}^i &= \boldsymbol{M}^T \cdot \left[\int_{{}_0V} \frac{\partial (\boldsymbol{B}_L)^T}{\partial {}^{t+\Delta t}_{0}\boldsymbol{U}} \cdot {}^{t+\Delta t}_{0}\boldsymbol{S}^i \cdot d\ {}_0V \right] \cdot \boldsymbol{M} \\ &= \boldsymbol{M}^T \cdot \left[\boldsymbol{K}_{mex}^i + \boldsymbol{K}_{mey}^i + \boldsymbol{K}_{mexy}^i \right] \cdot \boldsymbol{M} \end{aligned} \tag{4.37}$$

$$\boldsymbol{K}_{mg}^{i} = \boldsymbol{M}^{T} \cdot \left[\int_{{}_0V} (\boldsymbol{B}_0 + \boldsymbol{B}_L^i)^T \cdot \overline{\boldsymbol{D}} \cdot (\boldsymbol{B}_0 + \boldsymbol{B}_L^i) d\ {}_0V \right] \cdot \boldsymbol{M}$$

$$\boldsymbol{K}_{g}^{i} = \boldsymbol{G}^{T} \cdot \boldsymbol{k}_{g}^{i} \cdot \boldsymbol{G}$$

where, $\boldsymbol{K}_{me}^{i}$ and $\boldsymbol{K}_{mg}^{i}$ are the contributions of the elastic stiffness matrix and geometrical stiffness matrix of membrane element to the whole structure, respectively, $\overline{\boldsymbol{D}}$ is defined by Eq. (4.10) and depends on the elastic or plastic status of material at the time t, $\boldsymbol{K}_{g}^{i}$ is the contribution of the stiffness matrix of node-to-node element to the whole structure, and $\boldsymbol{k}_{g}^{i}$ is defined by Eq. (4.31) and depends on contact forces at time t. The nonlinear geometric problems, elastic-plastic problems and contact problems can be solved generally by these combinations.

The matrices $\boldsymbol{K}_{mex}^{i}, \boldsymbol{K}_{mey}^{i}$ and $\boldsymbol{K}_{mexy}^{i}$ are determined in Eq. (4.38)

$$
\boldsymbol{K}_{mex}^{i} = \frac{h \cdot {}^{t+\Delta t}_{0}S_{xx}^{i}}{4S_0}
\begin{bmatrix}
{}_0y_{23}^{\,2} & 0 & 0 & {}_0y_{23}\,{}_0y_{31} & 0 & 0 & {}_0y_{23}\,{}_0y_{12} & 0 & 0 \\
 & {}_0y_{23}^{\,2} & 0 & 0 & {}_0y_{23}\,{}_0y_{31} & 0 & 0 & {}_0y_{23}\,{}_0y_{12} & 0 \\
 & & {}_0y_{23}^{\,2} & 0 & 0 & {}_0y_{23}\,{}_0y_{31} & 0 & 0 & {}_0y_{23}\,{}_0y_{12} \\
 & & & {}_0y_{31}^{\,2} & 0 & 0 & {}_0y_{31}\,{}_0y_{12} & 0 & 0 \\
 & & & & {}_0y_{31}^{\,2} & 0 & 0 & {}_0y_{31}\,{}_0y_{12} & 0 \\
 & & & & & {}_0y_{31}^{\,2} & 0 & 0 & {}_0y_{31}\,{}_0y_{12} \\
 & & & & & & {}_0y_{12}^{\,2} & 0 & 0 \\
 & & & & & & & {}_0y_{12}^{\,2} & 0 \\
 & & & & & & & & {}_0y_{12}^{\,2}
\end{bmatrix}_{sym}
$$

$$
\boldsymbol{K}_{mey}^{i} = \frac{h \cdot {}^{t+\Delta t}_{0}S_{yy}^{i}}{4S_0}
\begin{bmatrix}
{}_0x_{32}^{\,2} & 0 & 0 & {}_0x_{32}\,{}_0x_{13} & 0 & 0 & {}_0x_{32}\,{}_0x_{21} & 0 & 0 \\
 & {}_0x_{32}^{\,2} & 0 & 0 & {}_0x_{32}\,{}_0x_{13} & 0 & 0 & {}_0x_{32}\,{}_0x_{21} & 0 \\
 & & {}_0x_{32}^{\,2} & 0 & 0 & {}_0x_{32}\,{}_0x_{13} & 0 & 0 & {}_0x_{32}\,{}_0x_{21} \\
 & & & {}_0x_{13}^{\,2} & 0 & 0 & {}_0x_{13}\,{}_0x_{21} & 0 & 0 \\
 & & & & {}_0x_{13}^{\,2} & 0 & 0 & {}_0x_{13}\,{}_0x_{21} & 0 \\
 & & & & & {}_0x_{13}^{\,2} & 0 & 0 & {}_0x_{13}\,{}_0x_{21} \\
 & & & & & & {}_0x_{21}^{\,2} & 0 & 0 \\
 & & & & & & & {}_0x_{21}^{\,2} & 0 \\
 & & & & & & & & {}_0x_{21}^{\,2}
\end{bmatrix}_{sym}
$$

$$
\boldsymbol{K}_{mexy}^{i} = \frac{h \cdot {}^{t+\Delta t}_{0}S_{xy}^{i}}{4S_0}
\begin{bmatrix}
2\,{}_0y_{23}\,{}_0x_{32} & 0 & 0 & {}_0y_{23}\,{}_0x_{13} + {}_0x_{32}\,{}_0y_{31} & 0 & 0 & {}_0y_{23}\,{}_0x_{21} + {}_0x_{32}\,{}_0y_{12} & 0 & 0 \\
 & 2\,{}_0y_{23}\,{}_0x_{32} & 0 & 0 & {}_0y_{23}\,{}_0x_{13} + {}_0x_{32}\,{}_0y_{31} & 0 & 0 & {}_0y_{23}\,{}_0x_{21} + {}_0x_{32}\,{}_0y_{12} & 0 \\
 & & 2\,{}_0y_{23}\,{}_0x_{32} & 0 & 0 & {}_0y_{23}\,{}_0x_{13} + {}_0x_{32}\,{}_0y_{31} & 0 & 0 & {}_0y_{23}\,{}_0x_{21} + {}_0x_{32}\,{}_0y_{12} \\
 & & & 2\,{}_0y_{31}\,{}_0x_{13} & 0 & 0 & {}_0y_{23}\,{}_0x_{13} + {}_0x_{32}\,{}_0y_{31} & 0 & 0 \\
 & & & & 2\,{}_0y_{31}\,{}_0x_{13} & 0 & 0 & {}_0y_{12}\,{}_0x_{13} + {}_0y_{31}\,{}_0x_{21} & 0 \\
 & & & & & 2\,{}_0y_{31}\,{}_0x_{13} & 0 & 0 & {}_0y_{12}\,{}_0x_{13} + {}_0y_{31}\,{}_0x_{21} \\
 & & & & & & 2\,{}_0y_{12}\,{}_0x_{21} & 0 & 0 \\
 & & & & & & & 2\,{}_0y_{12}\,{}_0x_{21} & 0 \\
 & & & & & & & & 2\,{}_0y_{12}\,{}_0x_{21}
\end{bmatrix}_{sym}
$$

(4.38)

where, h is the thickness of membrane element.

4.3 Analytical procedure

As mentioned above, the incremental step-by-step solution was used in this work. The status of node-to-node contact element from the discrete time t to the discrete time $t+\Delta t$ was assumed to be only in stick or slide condition. The analysis procedure which is described in Figure 4.5 is to find the solution at the time $t+\Delta t$.

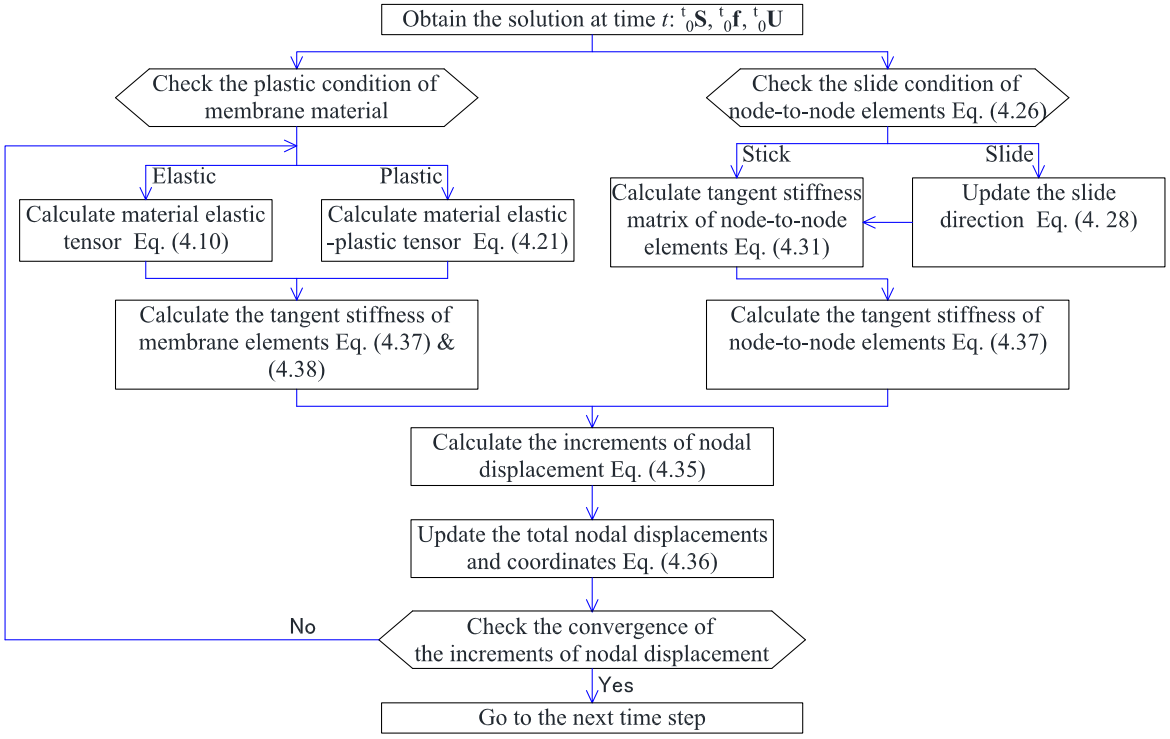

Figure 4.5 The analysis procedure from time t to time $t+\Delta t$

The tool *TLGAP* is established according to this analysis procedure. This tool is easily incorporated into existing nonlinear finite element programs, and the accuracy will be confirmed by the stretch fabrication experiments in Chapter 3 as well as the existing commercial program *ANSYS*.

4.4 Analytical examples and discussions

4.4.1. The analytical model of stretch fabrication experiments

The models of a quarter of specimens in stretch fabrication experiments of Chapter 3 are shown in Figure 4.6. Each model has *1482* triangular membrane elements and *19* node-to-node contact elements.

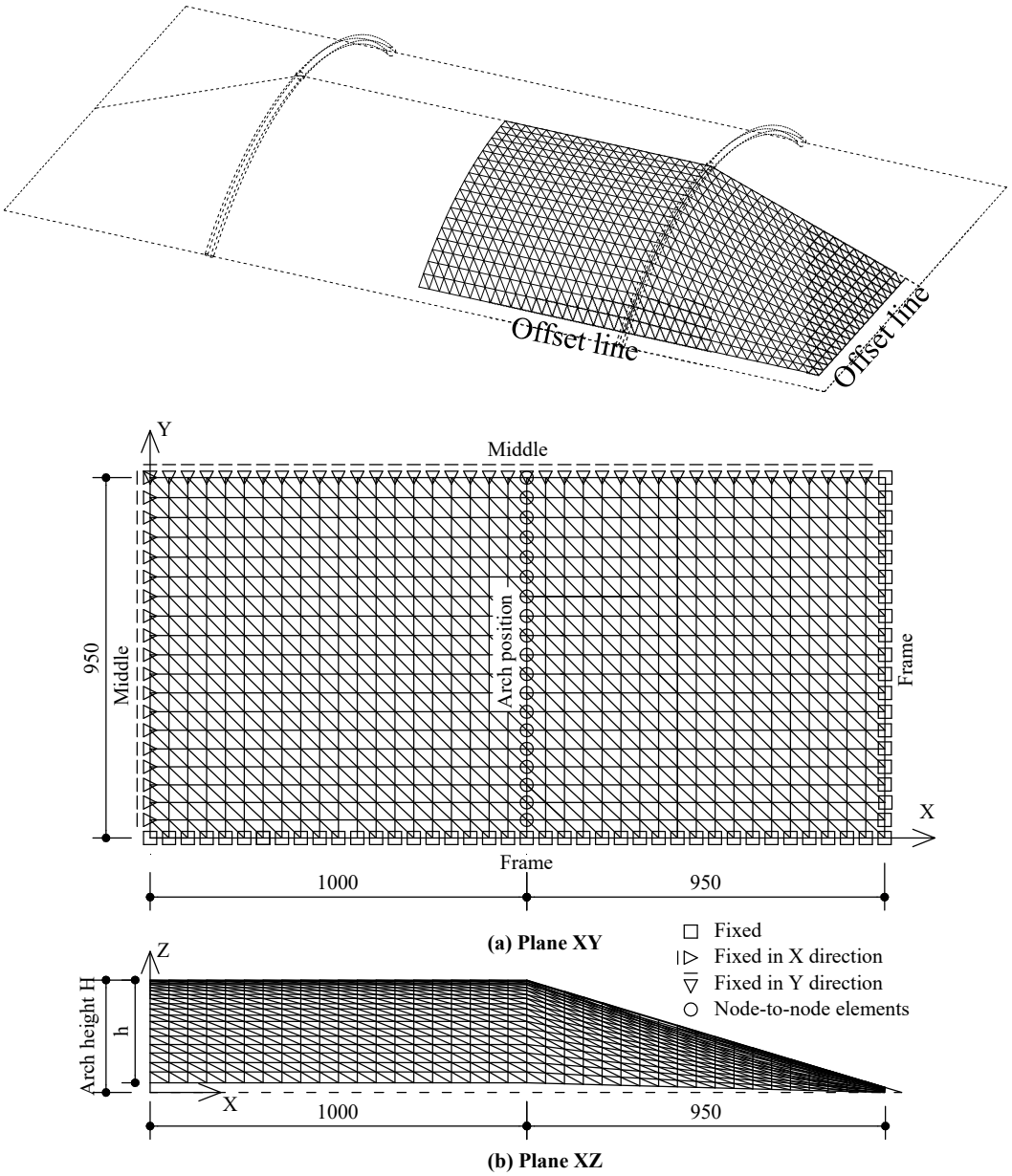

Figure 4.6 The models of a quarter of specimens

The initial shapes between two arches are assumed as a part of the cylinder, while the initial shapes between arches and outside frames are assumed to be straight from arches points to offset points. The offset points are assumed in fixed conditions, and the movements of these

points, which were observed in the experiments, are used as forced displacement conditions in these sample analyses. Totally, there are six analytical models which correspond to six specimens of stretch fabrication experiments. The motions of offset points are selected arbitrarily between the semifinal steps and the final steps as shown in Table 4.1.

Table 4.1 Forced displacement conditions at offset points in each specimen's model

PD10a	PD10b	PD15a	PD15b	PD20a	PD20b
Step 4	Step 3	Step 3	Step 5	Step 5	Step 5

The triangular membrane elements were used for ETFE film, and the contact between ETFE film and galvanized steel arches were modeled by node-to-node elements. The assumptions of local coordinated systems of node-to-node elements at the initial time t_0 are shown in Figure 4.7a. The normal contact directions z_0 were assumed from the center of arches to contact points, while the x_0 axes were defined as tangent directions of arches at contact points. The y_0 axes were determined from x_0 and z_0 axes. In these sample analyses, the y_0 axes coincide with the *X* axis of the global coordinate (Figure 4.6).

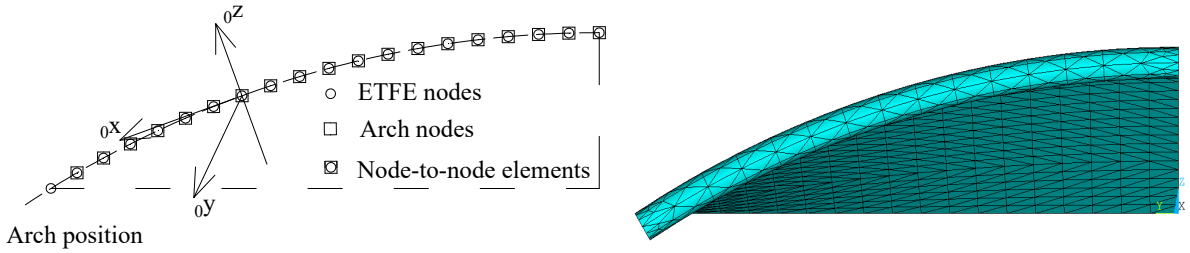

a. TLGAP tool *b. ANSYS*

Figure 4.7 Assumption of contact between ETFE films and galvanized steel arches

The existing commercial software *ANSYS* is used to confirm the suggested formulations and analytical procedure for the frictionless case. In *ANSYS* software, the *SHELL181* elements were used for ETFE film with the same mesh generation as shown in Figure 4.6. The *SOLID 187* elements modeled the steel arches, while *CONTA174* and *TARGE70* were used to model the contact between ETFE film and steel arches as shown in Figure 4.7b. In the next part, *TLGAP* indicates the results of suggested formulations, while *ANSYS* shows the results of *ANSYS*.

The material properties for ETFE film are determined based on uniaxial tension test [EJ13], [TY04] and shown in Table 4.2. It should be noted that the *2nd* Piola-Kirchhoff stress and Green-Lagrange strain are used in the suggested formulations, while the true stress and logarithm strain are used in *ANSYS* software [AN07]. However, the difference between two formulations are small in case of the "moderate" displacements [KB76] as these sample analyses.

Table 4.2 The properties of ETFE film

Young modulus	*800 MPa*
First yield point	*13.28 MPa*
Second yield point	*23.04 MPa*
First strain hardening ratio	*80.5 MPa*
Second strain hardening ratio	*3.0 MPa*

In these sample analyses, the penalty values of k_s and k_t in Eq. (4.31) are taken as three high order [SL93] than axial stiffness of ETFE film of $8*10^{15}$ N/m.

4.4.2. Frictionless contact case

This is an ideal case when there is no friction in the contact surface. The nodal Mises stresses, which are the average value of element Mises stresses concentrated at node, were calculated in both *TLGAP* and *ANSYS* programs. The results are compared over *4800* nodes of six analytical models and shown in Figure 4.8.

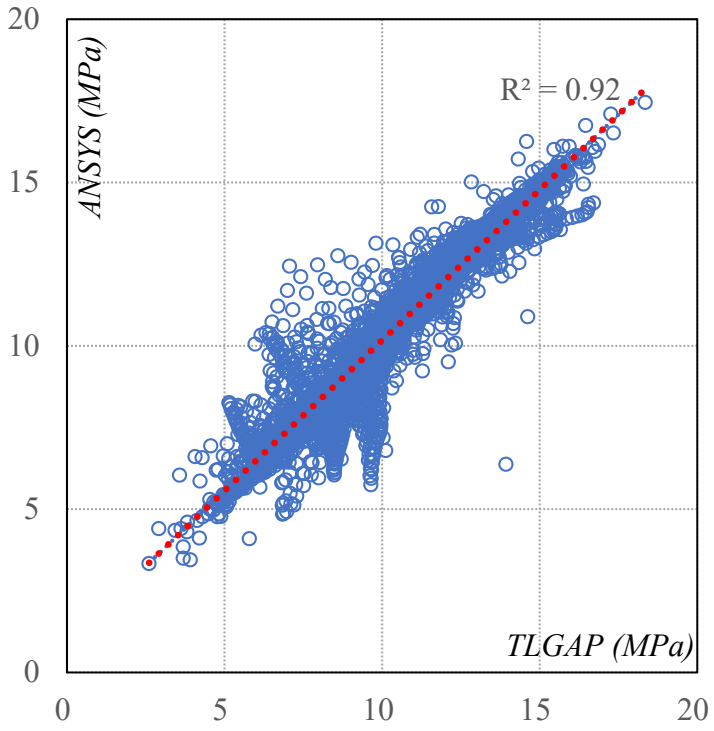

Figure 4.8 The nodal Mises stress in ANSYS and TLGAP

The correlation ratio between *ANSYS* and *TLGAP* is *0.92*. A good agreement is seen, and the results obtained by the proposed analytical method are validated. Figure 4.9 shows the analytical results of each specimen in both *ANSYS* software and the proposed analytical method.

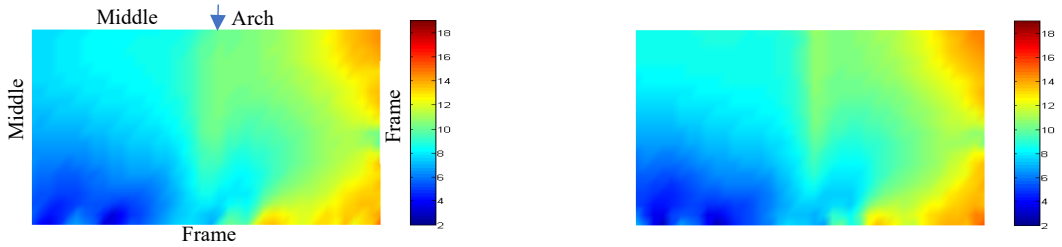

a1. PD10a, ANSYS *a2. PD10a, TLGAP*

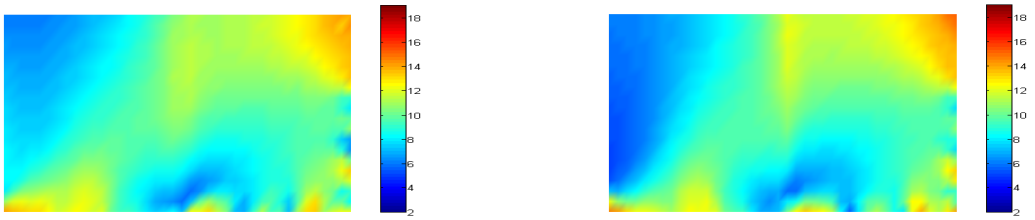

b1. PD10b, ANSYS *b2. PD10b, TLGAP*

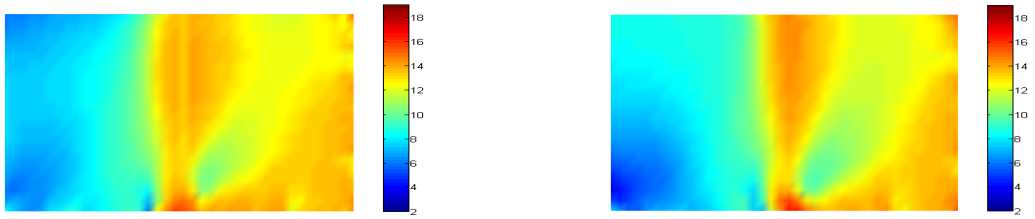

c1. PD15a, ANSYS *c2. PD15a, TLGAP*

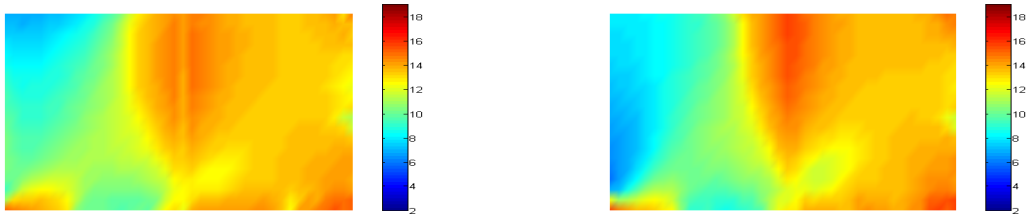

d1. PD15b, ANSYS *d2. PD15b, TLGAP*

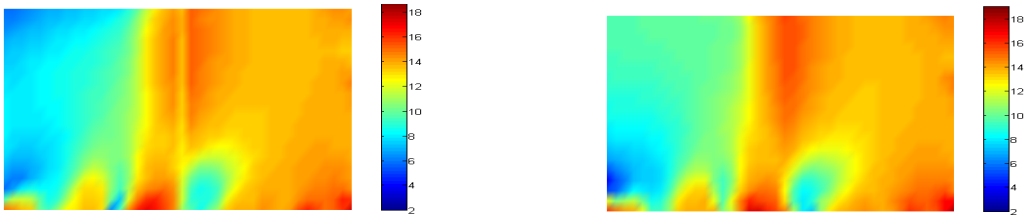

e1. PD20a, ANSYS *e2. PD20a, TLGAP*

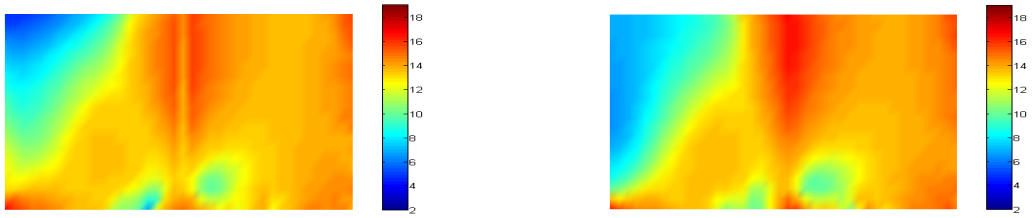

f1. PD20b, ANSYS *f2. PD20b, TLGAP*

Figure 4.9 The distribution of nodal Mises stress in ANSYS and TLGAP

4.4.3. Friction contact case

When friction exists on the contact interface, the solution of contact problem depends on the history of load applied to the structure. Therefore, the complexity of geometrical, elastic-plastic problems is increased when the friction contact is considered. Consequently, the results of above analytical examples could not be obtained by *ANSYS* due to the convergence criteria. However, the proposed analytical method still shows the effectiveness for the friction contact case.

(a) Effect of the number of load steps

In the proposed analytical procedure, the stick-slip phenomenon occurs during the static loading process. In order to observe the effect of the number of static load steps, the analysis was firstly repeated using *100*, *200* and *400* equal load steps. The friction coefficient of *0.3* is used to investigate the effect of load steps.

The equivalent friction force f_{gs} and the equivalent slide u_s in each of the node-to-node contact element are calculated in Eq. (4.39).

$$f_{gs} = \sqrt{{f_{gx}}^2 + {f_{gy}}^2}$$
$$u_s = \sqrt{{u_g}^2 + {v_g}^2} \tag{4.39}$$

where, f_{gx} and f_{gy} are the friction forces in the local coordinates x_0 and y_0, respectively, while u_g and v_g are the displacements in the local coordinates x_0 and y_0 or slide values between ETFE film and steel arch in x_0 and y_0 directions (Figure 4.7).

The relations between f_{gs} and u_s for the *PD15a* specimen at four specific node-to-node contact elements which correspond to the observed slide points in experiments (Figure 3.17a) are represented in Figure 4.10.

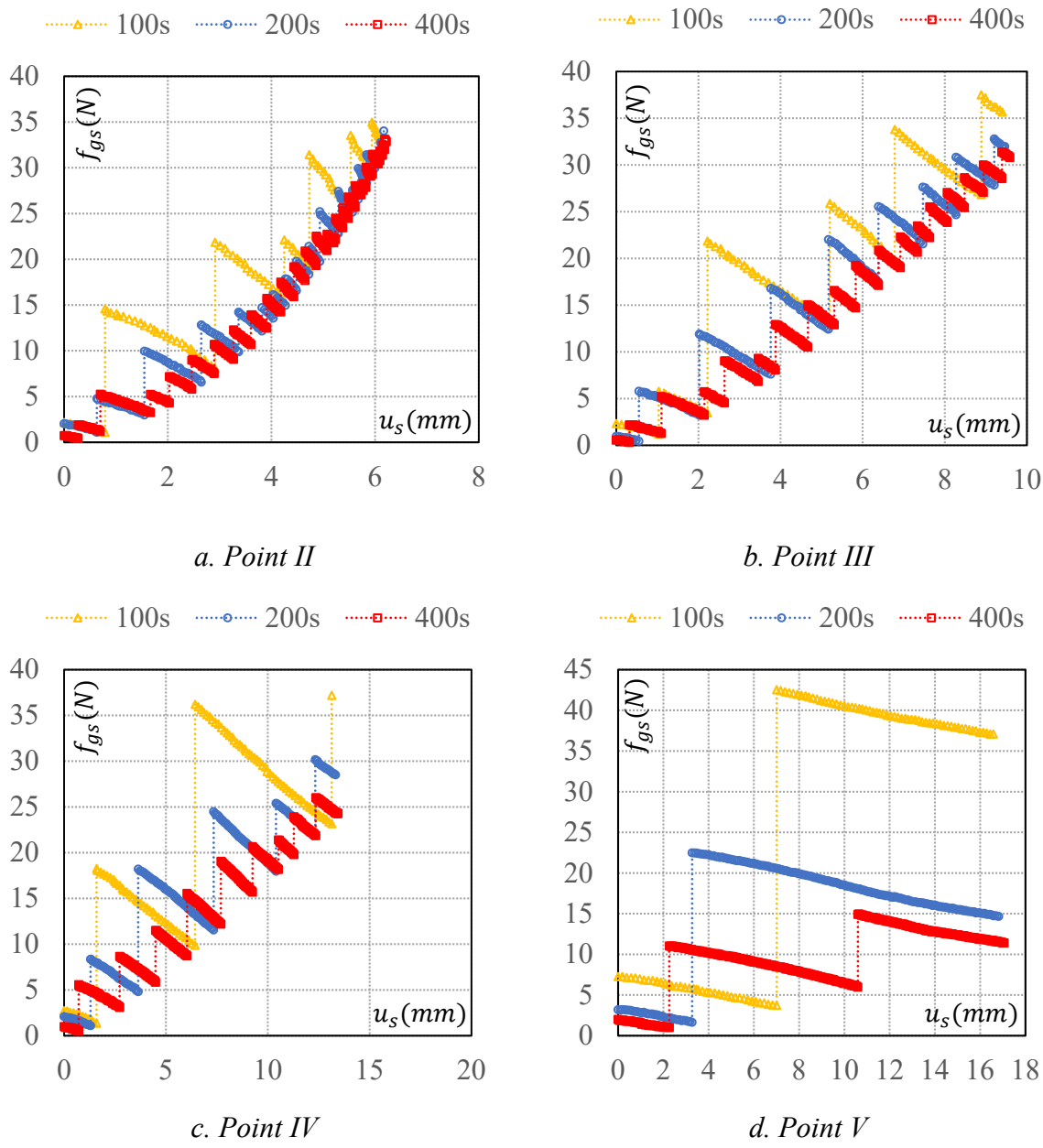

Figure 4.10 Relation between friction forces and slide values, $\mu = 0.3$, PD15a

In this figure, the dash lines with triangle, circle and square markers indicate the results of *TLGAP* for *100*, *200* and *400* equal load steps, respectively. It can be seen from Figure 4.10 that the stick-slip phenomenon occurs during the analysis. The higher the number of equal load steps is, the higher the frequency of occurrence of stick-slip phenomenon is, and the accuracy of the analysis will be improved dramatically. However, the increment of load steps accompanied with the increment of calculation time. In those sample analyses, the results obtained for *200* and *400* equal load steps are almost the same.

Figure 4.11 presents the distribution of nodal Mises stresses of *PD10a* and *PD15a* specimens for *100*, *200* and *400* equal load steps. It can be seen from Figure 4.11 that the nodal Mises stresses of ETFE film are almost the same for *100*, *200* and *400* equal load steps in both *PD10a* and *PD15a* specimens.

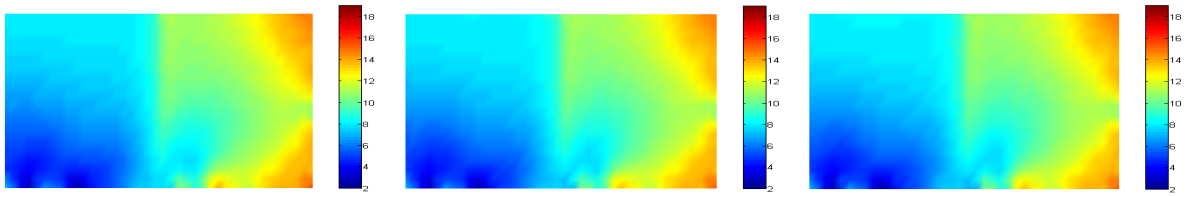

100 steps *200 steps* *400 steps*

a. Nodal Mises stress, $\mu = 0.3$, PD10a

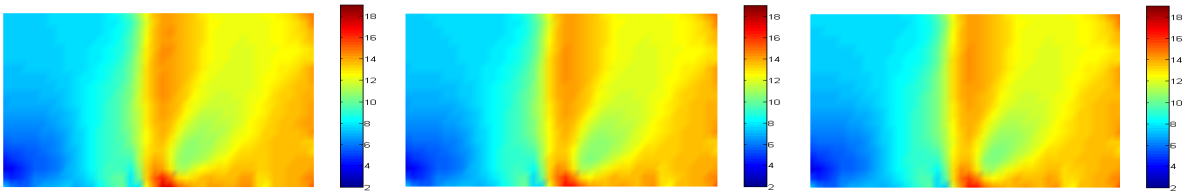

100 steps *200 steps* *400 steps*

b. Nodal Mises stress, $\mu = 0.3$, PD15a

Figure 4.11 The effect of load steps on Mises stress distribution of ETFE film

In conclusion, the *200* equal load steps are enough to evaluate both prestress on ETFE film and the friction characteristics at contact surfaces. Therefore, *200* equal load steps are chosen for the next investigations.

(b) Effect of friction coefficients on stress distribution of ETFE film

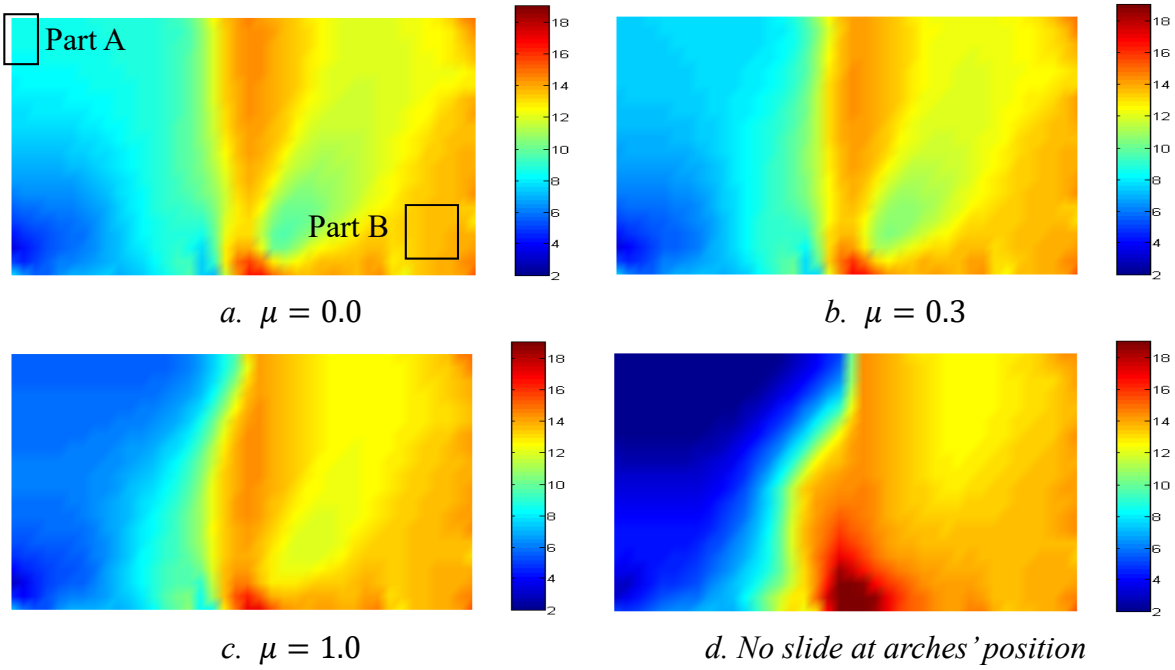

a. $\mu = 0.0$ *b.* $\mu = 0.3$

c. $\mu = 1.0$ *d. No slide at arches' position*

Figure 4.12 Distribution of nodal Mises stress in TLGAP results, PD15a

Figure 4.12 shows the distribution of nodal Mises stress for the specimen *PD15a*. When the slide between ETFE film and steel arch is ignored, the Mises stress of the middle part is small (Figure 4.12d). The increment of friction coefficient will decrease the slide values between the film and arch in the suggested formulation. As a result, the higher friction coefficient is, the smaller Mises stress of the middle part is.

The Mises stresses of part *A* and part *B* (Figure 3.8), which were observed in experiments, are used to compare with the results of the proposed analytical method throughout six specimens. Figure 4.13 presents those comparisons.

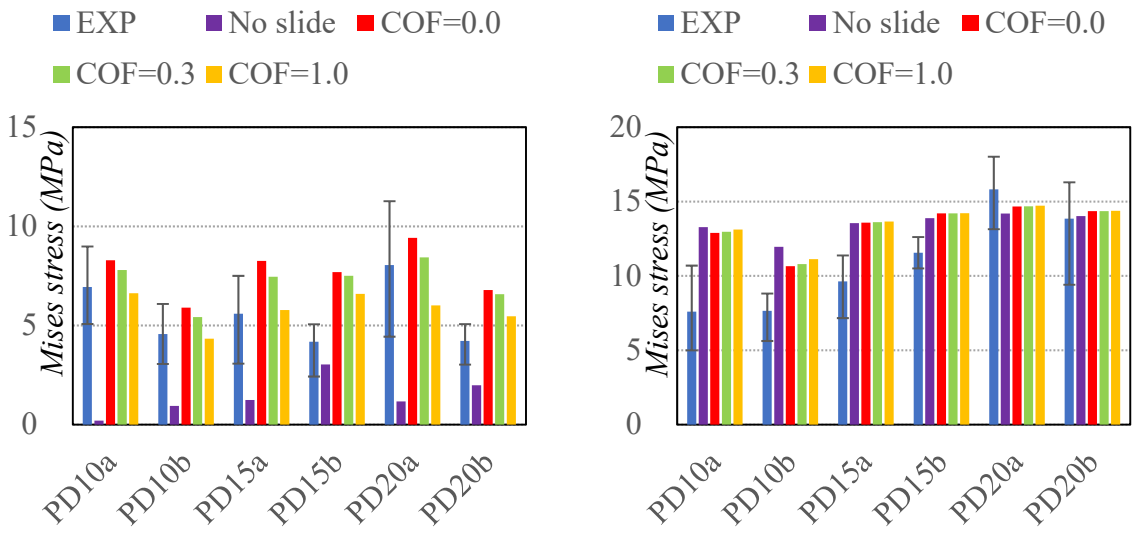

a. Part A *b. Part B*

Figure 4.13 Mises stress of part A and part B in both experiments and TLGAP

In Figure 4.13, the results of experiments are shown in bar and error bar type. The violet column shows the results of the fixed conditions between ETFE and arch, while the red, green and yellow bars present the results in case the static friction coefficient between ETFE and arch is *0.0*, *0.3*, *1.0*, respectively. At part *B*, the introduced prestress was mainly depended on the drawing value of *b*. The slide between ETFE and steel arch almost did not affect to the equivalent stresses at part *B*. Therefore, the Mises stresses of all cases of analyses were the same (Figure 4.13b). The results of experiments confirmed partially the results of *TLGAP*.

At part *A*, the same phenomenon was observed throughout the specimens. The increment of friction coefficient will decrease the slide values between the film and the arch. As a result, the higher friction coefficient is, the smaller Mises stress of part *A* is. The average values of the experiment results are in high agreement with the results of proposed method in case of *0.3* of static friction coefficient between ETFE and galvanized steel arch. Those results indicate the validity of proposed method firmly because the static friction coefficient between ETFE and steel plate are around *0.2* to *0.3* according to the technical report of Chemours Co., *[CH17]*.

(c) Observed slide values at position of arch

The static friction coefficient of 0.3 is used to investigate the slide values between ETFE film and steel arches in this section according to the results of section 4.4.3b. The deformation shapes of six analytical models are shown in Figure 4.14.

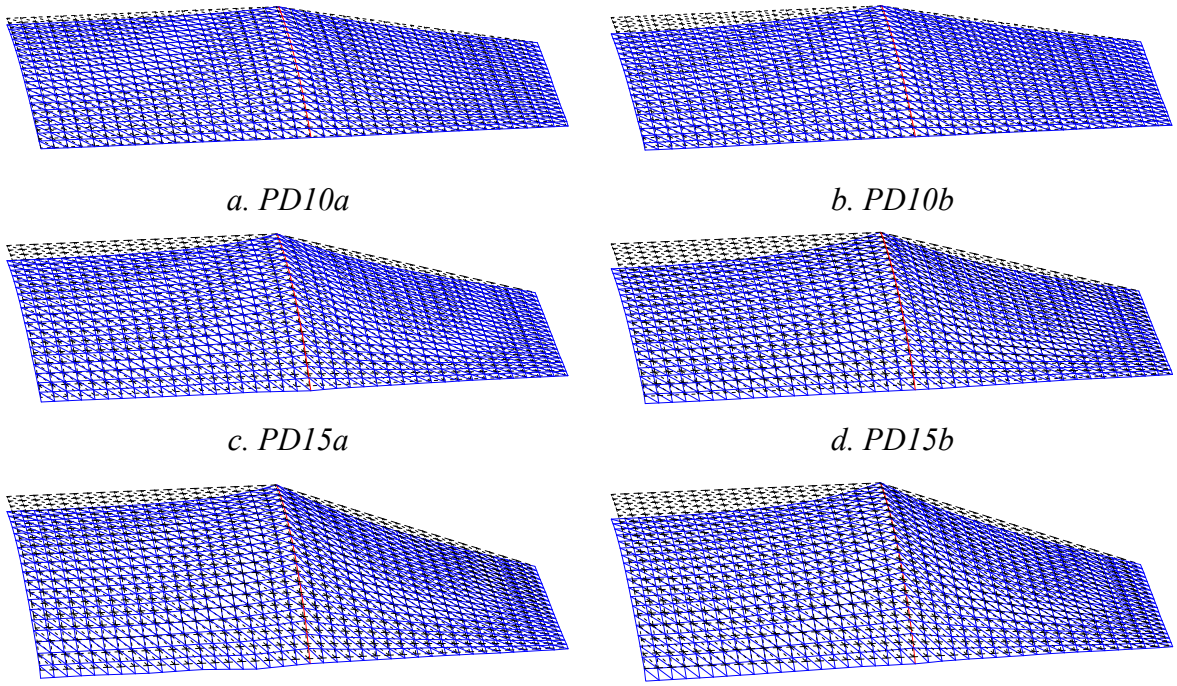

a. PD10a *b. PD10b*

c. PD15a *d. PD15b*

e. PD20a *f. PD20b*

Figure 4.14 Initial shapes and deformation shapes in TLGAP, $\mu = 0.3$

In this figure, the dash black lines show the initial shape, while the blue solid lines present the deformation shapes of proposed analytical method for the *0.3* of static friction coefficient between ETFE and steel arch. In addition, the red solid lines indicate the slides between ETFE and arches.

The relation between the slide values in *X* and *Y* directions (Figure 3.18) during the experiments and the relation between slide values in x_0 and y_0 directions (Figure 4.7) during the load steps in proposed analytical method are shown in Figure 4.15. In this figure, the dash lines with circle, square, diamond, triangle and minus markers present the results at point *I*, *II*, *III*, *IV* and *V* respectively. Generally, the high agreement can be seen between the experiments and suggested analytical method.

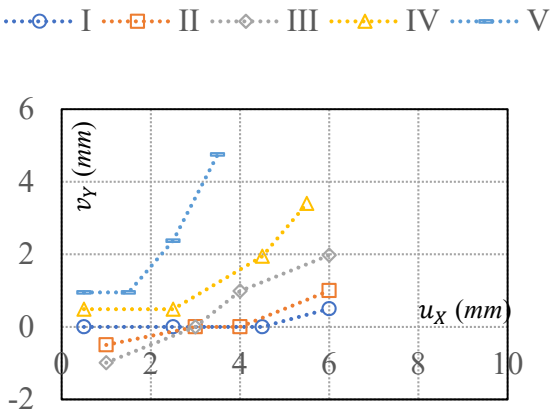

a1. PD10a, Experiment

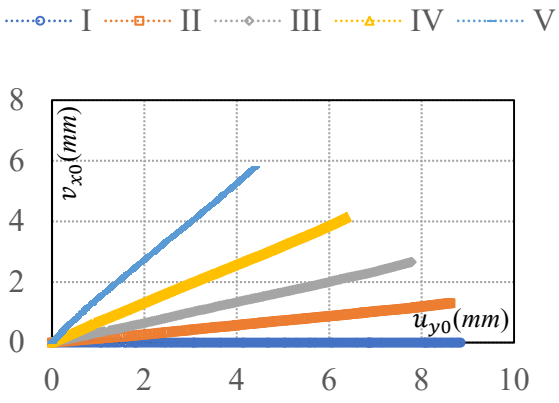

a2. PD10a, TLGAP

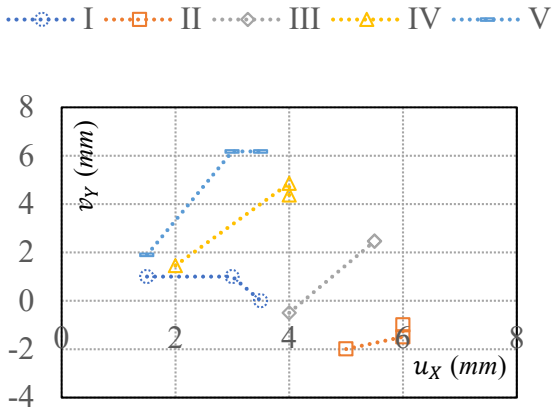

b1. PD10b, Experiment

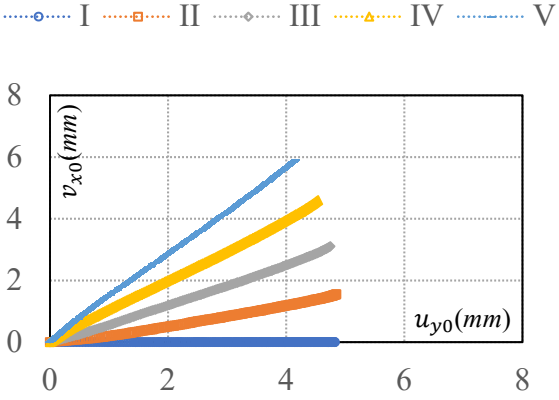

b2. PD10b, TLGAP

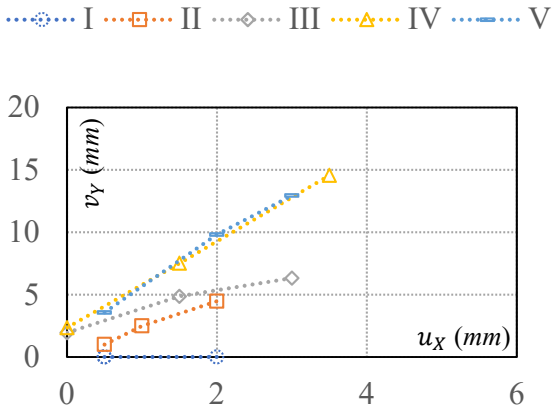

c1. PD15a, Experiment

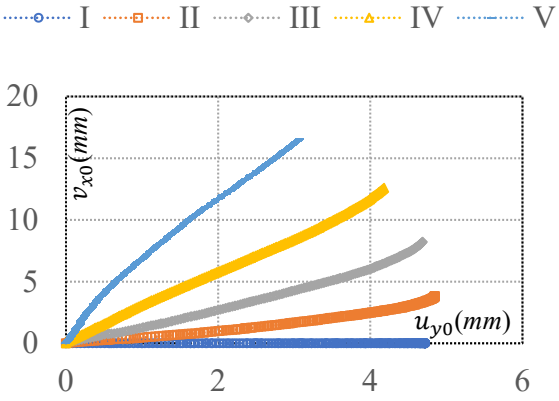

c2. PD15a, TLGAP

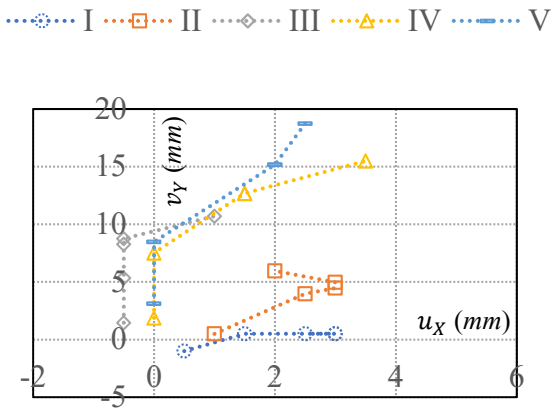

d1. PD15b, Experiment

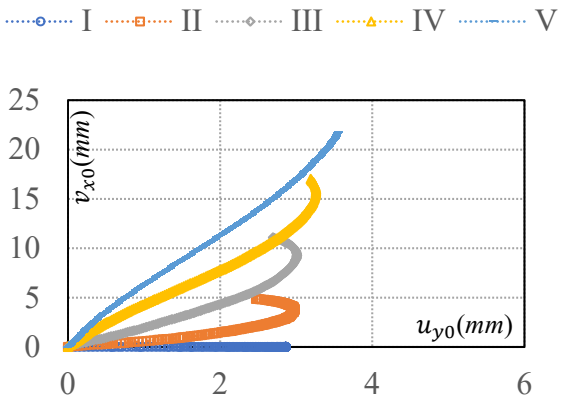

d2. PD15b, TLGAP

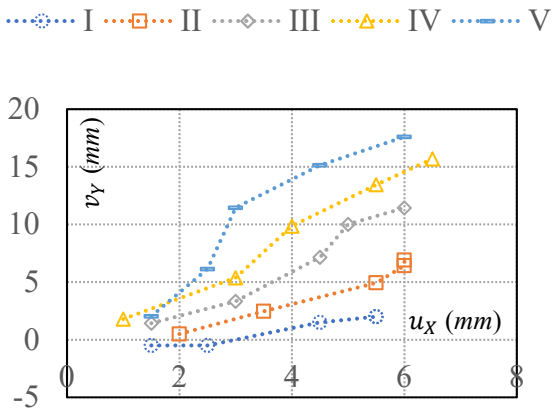

e1. PD20a, Experiment

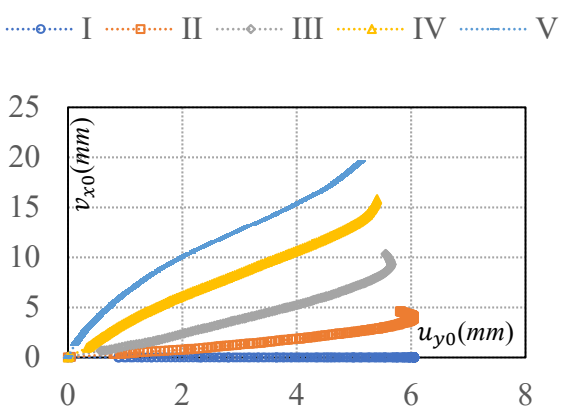

e2. PD20a, TLGAP

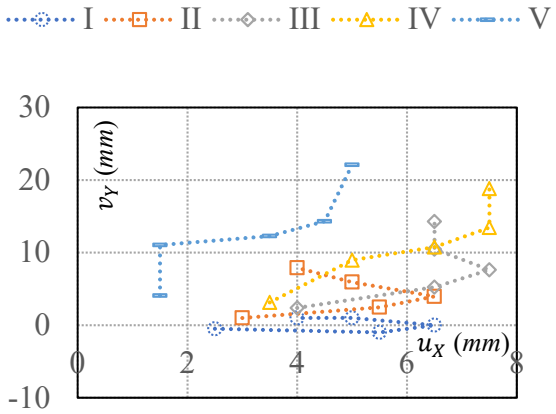

f1. PD20b, Experiment

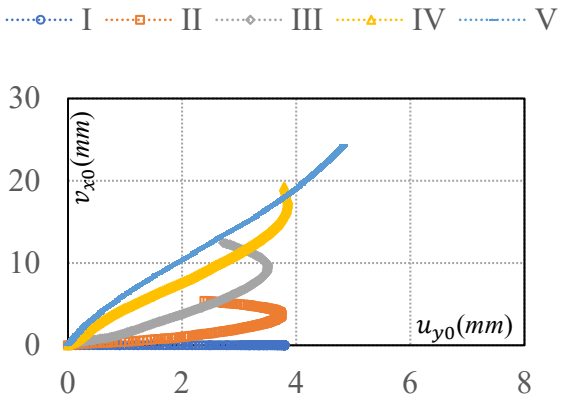

f2. PD20b, TLGAP

Figure 4.15 Slide history between ETFE and steel arches in both experiments and TLGAP, $\mu = 0.3$

The slide values in x_0 and y_0 directions in the proposed analytical method are transformed into the *X* and *Y* directions and compared with the results of the experiments. The Figure 4.16 shows these comparisons. The horizontal axis presents the results of *TLGAP*, while the vertical axis indicates the results of experiments. The proposed analytical method is in high agreement with the observed values of experiments in *Y* direction, while there have a few of differences in *X* direction, especially in case of *PD10a* and *PD20b* specimens. However, the history of slide in *X* and *Y* directions is almost the same between the analyses and the experiments (Figure 4.15a, Figure 4.15f). Therefore, these discrepancies can be accepted, and the validity of proposed method is confirmed.

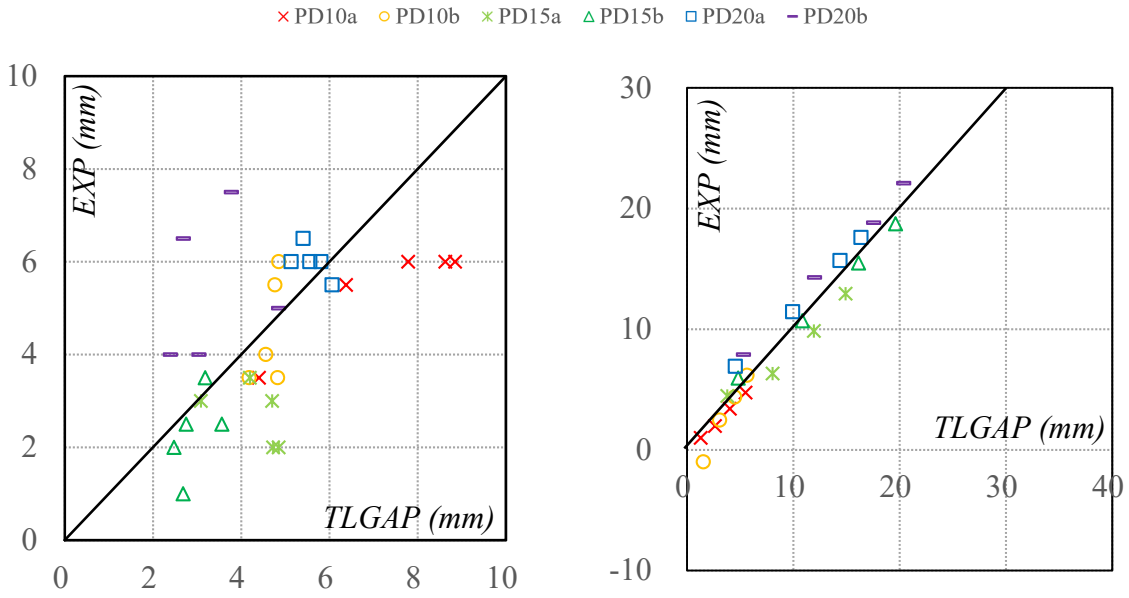

a. Slide in X direction *a. Slide in Y direction*

Figure 4.16 The comparison of slide values between experiments and TLGAP, $\mu = 0.3$

4.5 Summary

(a) The total Lagrangian formulations were established for both triangular membrane element and node-to-node contact elements. The analytical procedure which used these formulations to solve the problems of geometrical nonlinearity, the material nonlinearity and the nonlinearity of friction contact was also suggested.

(b) The number of load steps affected to the accuracy of results of the proposed analytical method. The greater number of load steps was, the more accuracy the results were. However, the increment of load steps accompanied with the increment of calculation time. In those sample analyses, *200* of equal load steps was recommended.

(c) The analytical proposed method was in the high agreement with the existing commercial software *ANSYS* for the frictionless case. Moreover, this method was effective for the friction contact too.

(d) The accuracy of proposed analytical method was confirmed by stretch fabrication experiments in both Mises stress and observed slide values between ETFE film and galvanized steel arches. The results of proposed method for the *0.3* of static friction coefficient between ETFE and galvanized steel arches were in good agreement with the results of experiments.

Chapter 5.
Fabrication of three-dimensional ETFE curved surface by stretching drape strips considering friction contact

Chapter 5. Fabrication of 3D ETFE curved surface by stretching drape strips considering friction contact

5.1 Introduction

The fabrication of low-rise 3D smooth curved surface of saddle type tensile membrane structure by stretching plane strips of ETFE film for the middle part was confirmed. However, the establishment of high-rise 3D smooth curved surface by drawing the plane strips still had problems because of the occurrence of wrinkling and the insufficient prestress. Therefore, the stretching of drape strips for the middle part should be proposed to fabricate the high-rise smooth curved surface. In addition, the results of the proposed analytical method in Chapter 4 were in good agreement with the results of experiments of Chapter 3 for the *0.3* of static friction coefficient between ETFE and galvanized steel arches. However, the possibility of using this value of static friction coefficient should be investigated furthermore by both the element experiments and the stretch fabrication experiments. Therefore, the purposes of this chapter are:

(1) The rolling test is carried out to investigate the static friction coefficient between ETFE film and black/galvanized steel pipes.

(2) The stretch fabrication experiments for saddle type of tensile membrane structure of *15%* rise ratio: (a) the results of form finding and cutting pattern analysis in Chapter 2 are applied to fabricate the specimens of *1:1* and *3:1* of prescribed stress ratios between the *MD* and *TD* directions for the middle part; (b) The analytical method in Chapter 4 is used to predict the drawing values considering the friction contact between ETFE film and galvanized steel arches. This prediction guarantees the sufficiency of introduced prestress and the absence of wrinkling; (c) The stretch fabrication experiments are carried out to confirm this fabrication technique.

(3) The pressurization test is investigated to confirm the strength of the ETFE tensile membrane structure type after above introduced prestress stage.

5.2 Rolling test on static friction coefficient between ETFE and steel pipes

5.2.1. Process and setup of experiments

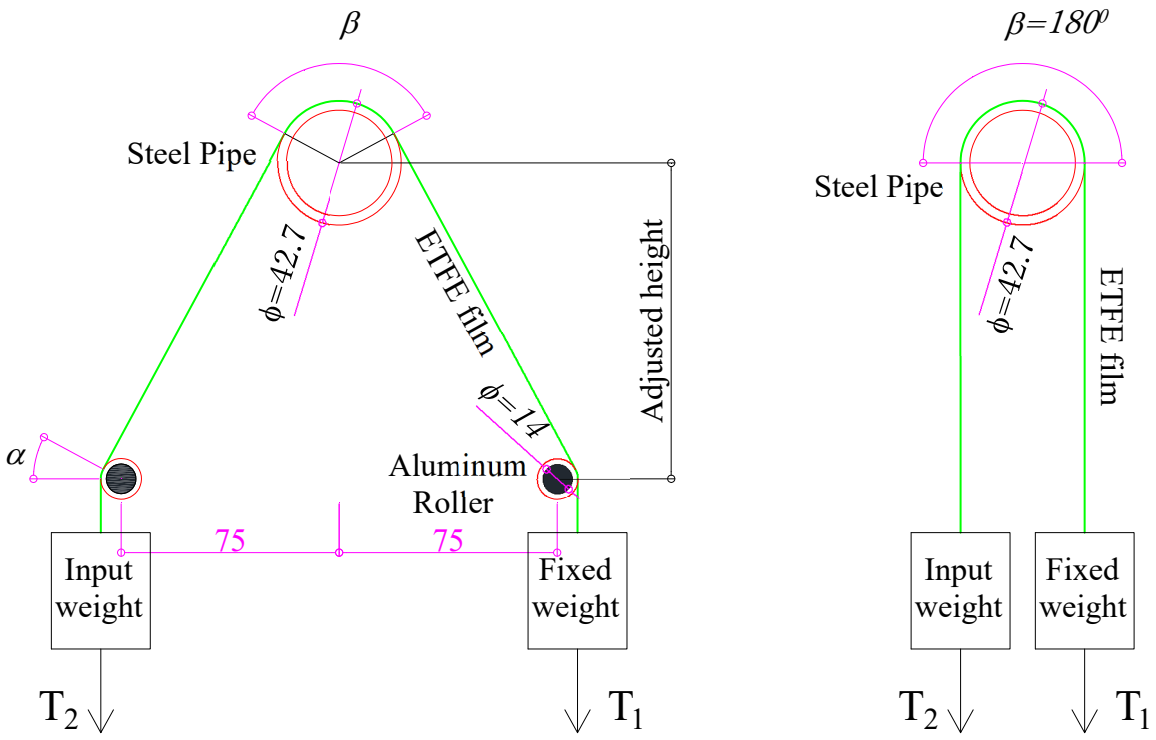

a. Phase 1 *b. Phase 2*

Figure 5.1 Setup of rolling test on static friction coefficient (all dimensions are in millimeter)

Figure 5.1 shows the setup of rolling test for static friction coefficients between ETFE film and steel pipes. The setup of experiment consists the test steel pipes, ETFE film, two aluminum rollers and weights, and these components comprise a simple system in which a pulley method *[SU95], [YS14]* is implemented for friction measurement. The steel pipes are fixed in the experiments. There are two types of steel pipes which are described in Table 5.1, while the properties of ETFE film for the test are shown in Table 5.2.

The experiments were carried out in two phases. In *phase 1*, the two aluminum rollers, which can be adjusted the heights, were used to investigate the effect of five contact angles: $\beta = 76^0(\alpha = 52^0)$, $\beta = 95^0(\alpha = 42^0)$, $\beta = 110^0(\alpha = 35^0)$, $\beta = 123^0(\alpha = 28^0)$, $\beta = 180^0(\alpha = 0^0)$ on the static friction coefficient between the ETFE film and steel pipes. The contacts between two aluminum pipes and ETFE were reduced by the setup of rollers and the lubrication of oil. However, this setup still had the effect on the test results of friction contact between steel pipes and ETFE films which will be discussed in the next section. Therefore, the experiments were carried out in *phase 2* in which only one of contact angle $\beta = 180^0$ was

setup to measure the friction between the test steel pipes and ETFE film.

In the experiments, the specimens of ETFE film were put on the steel pipes, and the identical weights were set up at the ends of the film. Next, the input weight (T_2) was increased slowly by adding water to a container hung on at the one end of ETFE specimens. When the slide between the ETFE film and steel pipes was observed, both fixed weight (T_1) and the input weight (T_2) were measured by the *A&D EK-6000H* equipment. In *phase 1*, the fixed weight (T_1) was set up as *150g*, while this weight was changed within range of *50g*, *100g*, *150g*, *200g* and *250g* in *phase 2*. The experiments were repeated in six trials for one case of fixed weight in both phases.

Table 5.1 The properties of ETFE specimens

Parameters	Values
Width	*20~30 mm*
Thickness	*200 μm*
Type	*Printed dot*

Table 5.2 The properties of steel pipes

Parameters	Values
Material test standard	*JIS G3452*
Dimensions	$\emptyset = 42.7\ mm$
Thickness	$t = 3.2\ mm$
Division	*Black & Galvanized types*

Figure 5.2 presents the photos of the setup of the experiments, the specimens of ETFE film and the steel pipes.

a. Experiments' setup

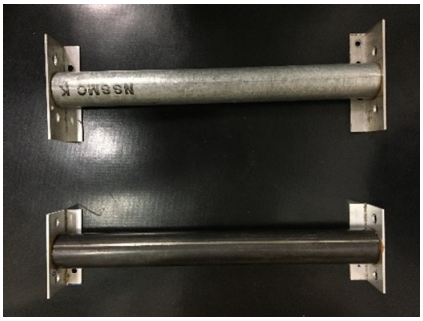

b. Test steel pipes

c. Test ETFE specimens

Figure 5.2 Photos of setup of experiments, ETFE specimens and steel pipes

5.2.2. Results and discussions on static friction coefficient between ETFE and steel pipes

In *phase 1* and *phase 2*, the static friction coefficients between ETFE and steel pipes can be obtained via the Euler's belt formula in Eq. (5.1)

$$ln\left(\frac{T_2}{T_1}\right) = \mu \cdot \theta \tag{5.1}$$

where, T_2 is the input weight, T_1 is the fixed weight, μ is static friction coefficient, and θ is the contact angle.

a. Phase 1

The relations between the contact angle in *phase 1* and the natural logarithm between the input weights and fixed weights are shown in Figure 5.3.

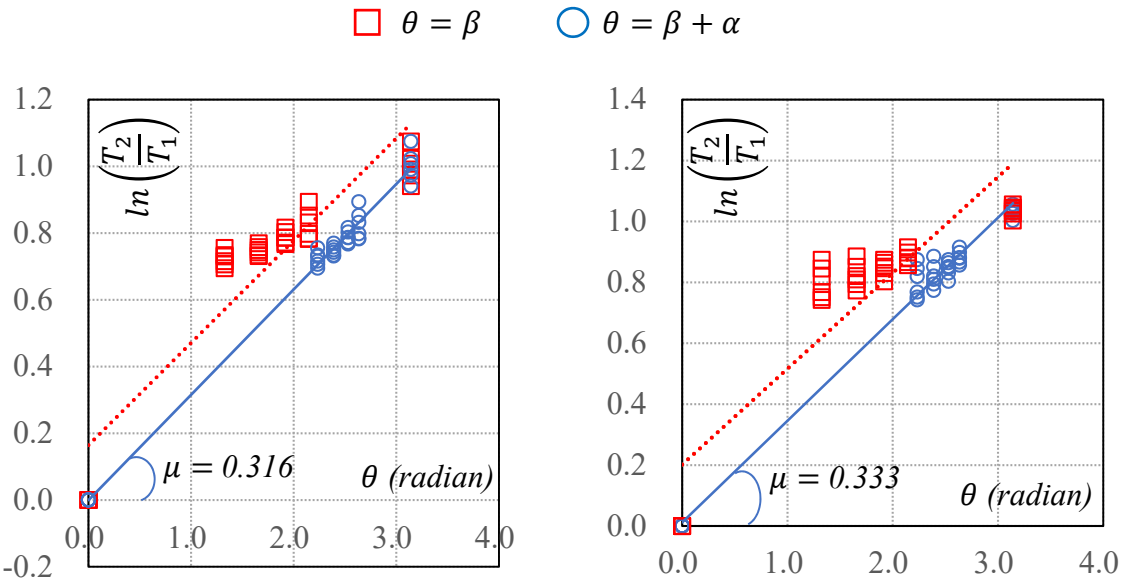

a. ETFE and galvanized steel pipe *b. ETFE and black steel pipe*

Figure 5.3 Effect of friction contact angle on static friction coefficients

In *phase 1*, when the friction contacts between ETFE film and aluminum rollers are ignored the contact angle θ is determined as the angle β which is described in Figure 5.1a. In Figure 5.3, the square makers represent the relation between $\theta = \beta$ and the natural logarithm $ln(T_2/T_1)$, while the dash lines show the linear regression lines [BR09]. Mathematically, the equation Eq. (5.1) implied that when the contact angle is zeros, the natural logarithm $ln(T_2/T_1)$ is also zeros. Therefore, those regression lines should pass through the origin. However, it can be seen from Figure 5.3 that the constant terms of the dash regression lines are obtained because of the effect of friction contact between ETFE and aluminum rollers.

When we assume that the static friction coefficient between ETFE and aluminum rollers is

a half of static friction coefficient between ETFE film and test steel pipes, the contact angle θ is determined as $\beta + \alpha$ which are described in Figure 5.1a. The relations between $\theta = \beta + \alpha$ and the natural logarithm $ln(T_2/T_1)$ are shown by the circle markers in Figure 5.3. And the constant terms of the regression lines which are indicated by solid lines, are eliminated by this assumption.

In conclusion, the slopes of solid regression lines represent the static friction coefficients between ETFE film and steel pipes as: (a) *0.316* in case of ETFE and galvanized steel pipe; (b) *0.333* in case of ETFE and black steel pipe

b. Phase 2

In *phase 2,* the contact angle is set up as $\theta = \beta = 180^0$ (Figure 5.1b) to eliminate the effect of friction contact of aluminum rollers. The fixed weight was changed to check the effect of tension of ETFE film. There were five cases of tension of ETFE film of *25*, *49*, *74*, 98 and *123 N/m*. The experiments were repeated randomly in six trials for one case of tension. The static friction coefficients between ETFE film and steel pipes are calculated by Eq. (5.1), and the results are shown in the relation with the tension of the film in Figure 5.4.

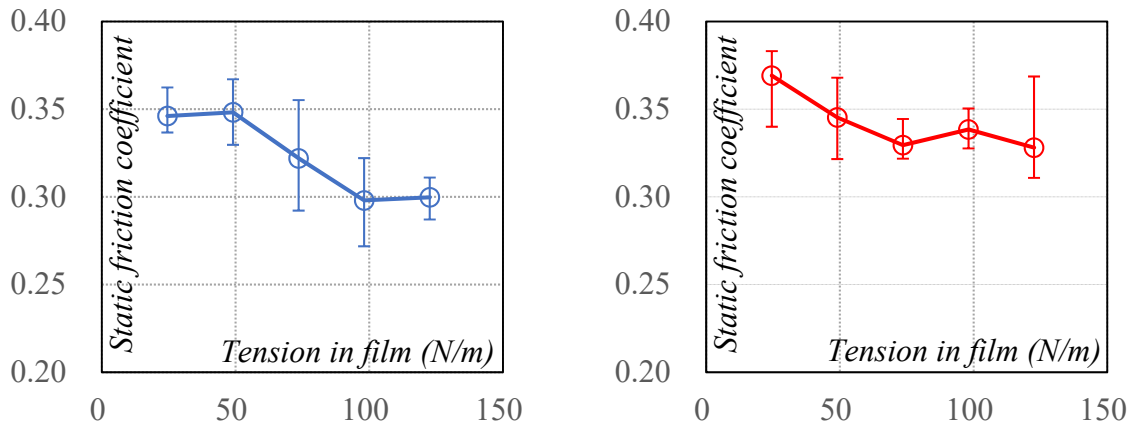

a. ETFE and galvanized steel pipe *b. ETFE and black steel pipe*

Figure 5.4 Effect of tension of film on static friction coefficients

In Figure 5.4, the solid lines show the average values of static friction coefficients, while the bars and error bars present the maximum and minimum values of six random measurements. As we can see from Figure 5.4, the average values of static friction coefficient between ETFE film and galvanized steel pipe decrease from *0.346* to *0.300* when tension forces in ETFE film increase from *25 N/m* to *123 N/m*. The same phenomenon was observed in case of friction contact between ETFE and black steel pipe. The average values of static friction coefficient between ETFE film and black steel pipe decrease from *0.369* to *0.328*. The reason can be

explained as the contact areas between the film and asperities of the surfaces of steel pipes were more widely under the low tension. This is so-called the anchor effect [YS14]. This effect can also be used to explain the reason why the friction coefficient between ETFE and black steel pipe are larger than this coefficient between ETFE and galvanized steel pipe.

5.2.3. Summary on static friction coefficient between ETFE film and steel pipes

The average values of static friction coefficient between ETFE film and galvanized steel pipe is *0.323*, and this coefficient between ETFE film and black steel pipe is *0.342*. Compared with the static friction coefficient between ETFE and steel plate of around *0.2* to *0.3* according to technical report of Chemours Co., [CH17], those results indicated the validity. In addition, the phenomenon that the static friction coefficient decreases with the increase of the film tension is confirmed by above element experiments. Moreover, the results of analytical method in Chapter 4 were in good agreement with the results of the stretch fabrication experiments in Chapter 3 for the 0.*3* of static friction coefficient between ETFE and galvanized steel pipe. In conclusion, the value of *0.3* of the static friction coefficients between ETFE film and galvanized steel arch can be used in the stretch fabrication method.

5.3 Fabrication experiments of 3D ETFE curved surface by stretching drape strips

5.3.1. Overview of experiments

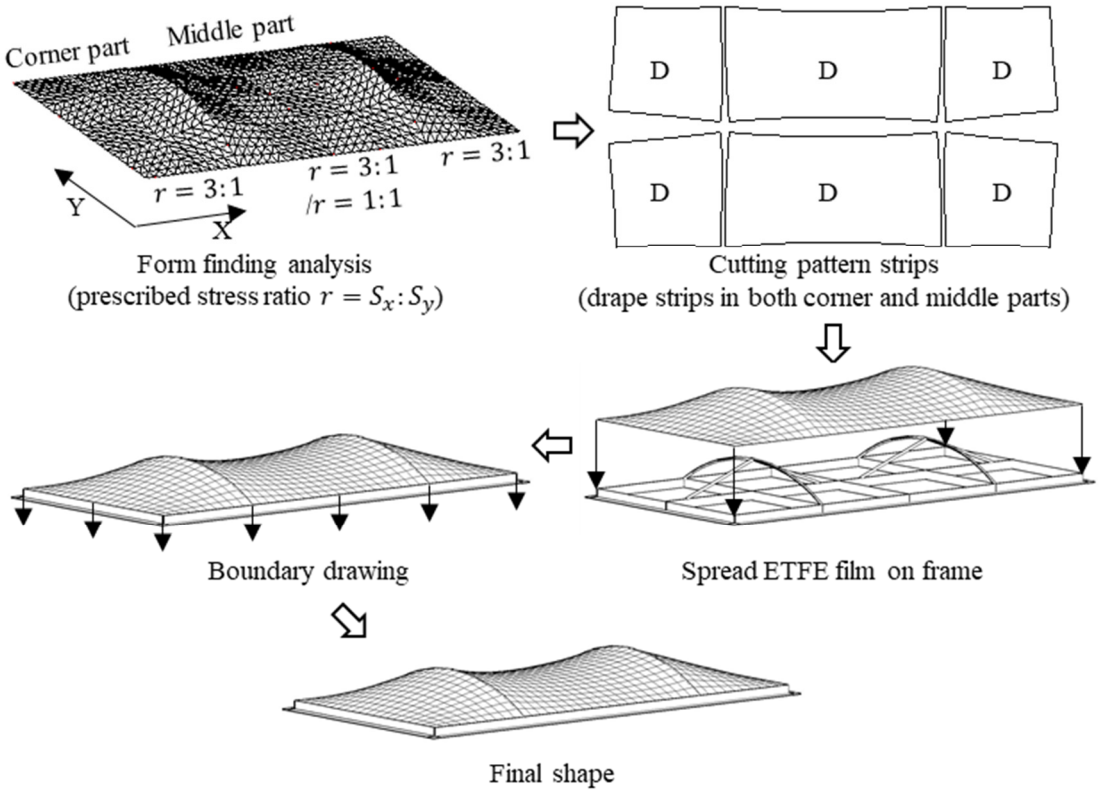

Figure 5.5 The process of stretch fabrication experiments, drape strips for middle part

The process of stretch fabrication experiments was described in Chapter 3. Figure 5.5 represents this process for the convenience in which the drape strips are used for the middle part of the saddle tensile membrane structure. Only *15%* of rise ratio is investigated in the experiments of this chapter. The ideal shape of the corner part is found by form finding analysis for the *3:1* of prescribed stress ratio between *X* and *Y* directions, while the ideal shapes of the middle part are obtained for the *3:1* and *1:1* of the prescribed stress ratios. There are two types of specimens which cutting pattern shapes of the corner part and the middle part are shown in Figure 5.6. Each type of cutting strips has two specimens named as *a* and *b*, so there are four specimens totally as *DD1511a/b* and *DD1531a/b*. The letter *"D"* indicates the drape type of strips for both corner and middle parts. While the former number *15* presents the rise ratio of *15%*, the later number *11* and *31* show the values of *1:1* and *3:1* of the prescribed stress ratio for the middle part, respectively. Table 5.3 represents the information of specimens. The thickness of ETFE film is $250\mu m$ in these experiments.

Table 5.3 Information of specimens

Specimens	Rise ratio	Types of cutting strip		ETFE properties	
		Corner	Middle	Thickness	Type
DD1511a/b	*15%*	*Drape (3:1)*	*Drape (1:1)*	*250 μm*	*Printed dot*
DD1531a/b	*15%*	*Drape (3:1)*	*Drape (3:1)*	*250 μm*	*Printed dot*

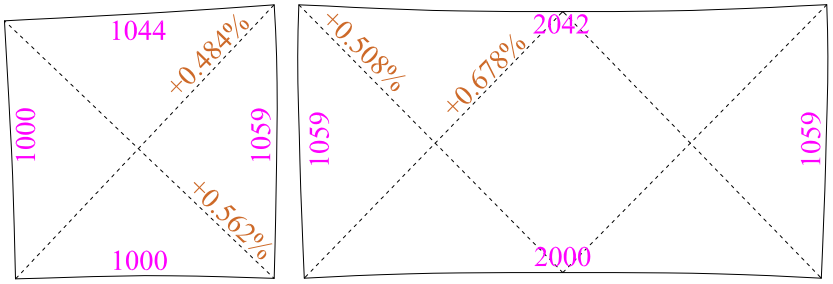

Corner part *Middle part*

a. DD1511 specimens

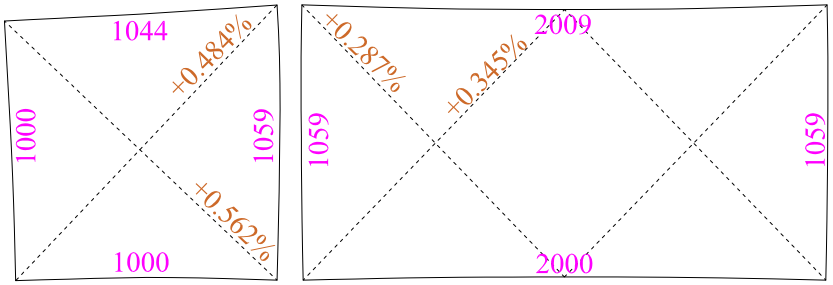

Corner part *Middle part*

b. DD1531 specimens

Figure 5.6 Types of cutting strips (all dimensions are in millimeter)

The numbers show the lengths of cutting lines, while the percentages indicate the expansions of the lengths of drape strips and the corresponding lengths of the form finding shapes in Figure 5.6.

5.3.2. Prediction for values of drawing boundary

Two purposes of the prediction are: (1) the introduced Mises prestress on ETFE film is around the first yield point of this film, and the equivalent strain is smaller than *10%*; (2) The absence of wrinkling is required.

Figure 5.7 shows the assumptions for analytical models of the prediction. The models of a quarter of specimens, which have *400* triangle membrane elements and *10* node-to-node contact elements, are used to predict the behavior of ETFE film and friction contact between the film and supporting galvanized steel arches.

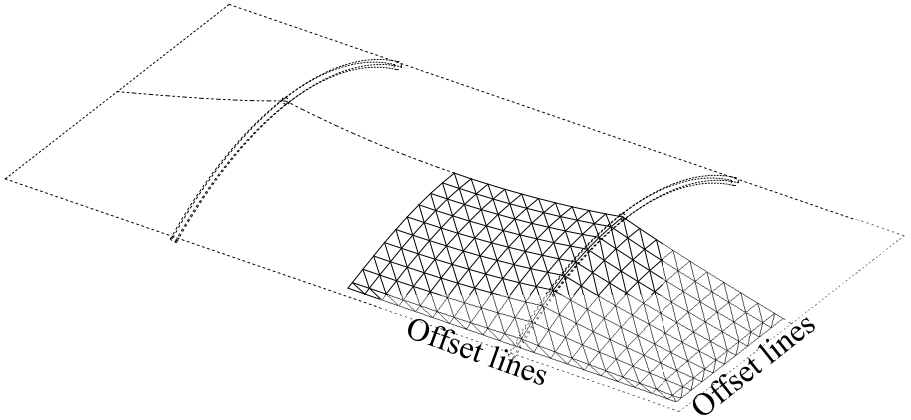

a. 3D view of the models of a quarter of specimens

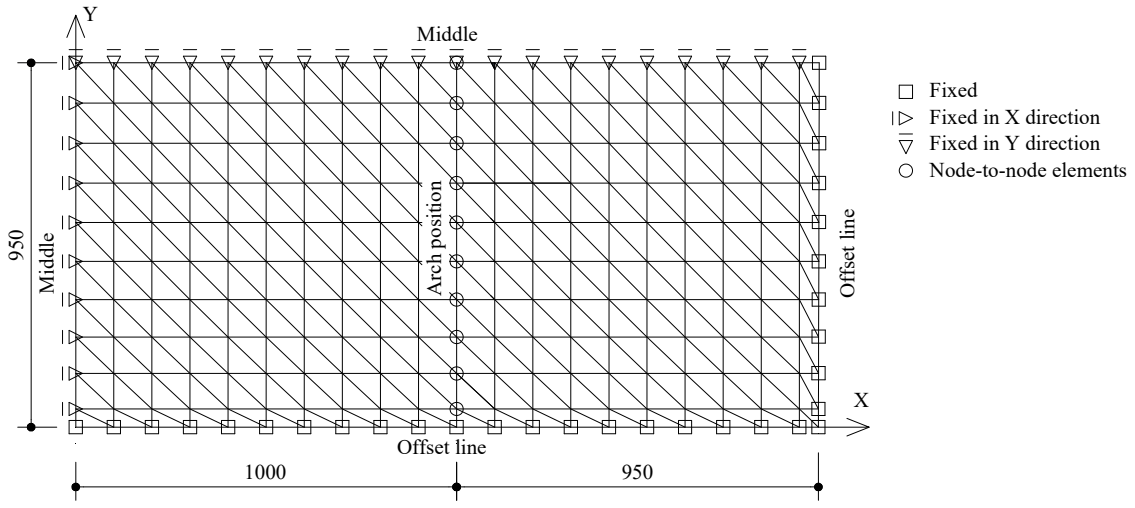

b. XY plane

Figure 5.7 Models of a quarter of specimens in prediction

The initial shapes of those models are adapted from the results of form finding analysis. The offset points are assumed in fixed conditions, and the movements of these points are used as forced displacement conditions in these analytical models. The relation between the motion of those offset points and the boundary drawing values in section 3.3.4 are used to determine

the drawing values. In the other words, one of drawing values of *a*, *b*, *c* and *d* will give the corresponding movements of offset points which can be determined by Figure 3.17. While the properties of ETFE film are similar in Chapter 4 (Table 4.2), the static friction coefficient between ETFE film and galvanized steel arches is adapted as *0.3*.

(a) Prediction for sufficient introduced Mises prestress

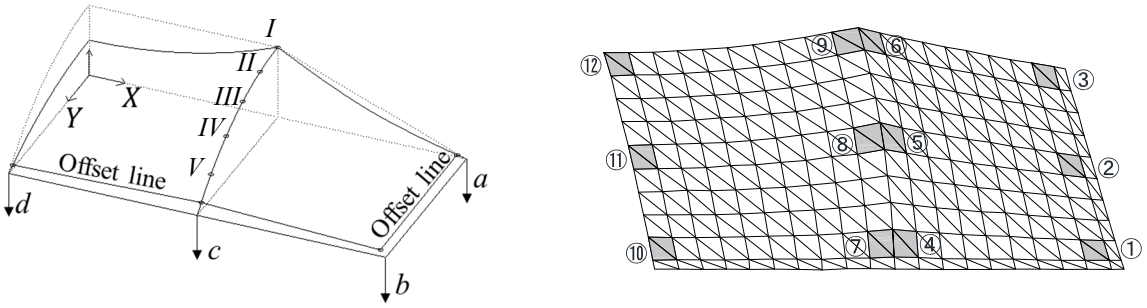

a. Positions of drawing values *b. Observed elements*

Figure 5.8 Drawing values and observed elements

Figure 5.8 indicates the drawing values at four special positions and the observed elements in the prediction. As mentioned above, this prediction will guarantee that the introduced Mises prestress on ETFE film is around the first yield point of this film, and the equivalent strain is smaller than *10%*. This work increases the yield strength of the film and promises the absence of the tear of the film. Therefore, the drawing values of *a, b, c* and *d* at the final step are determined in Table 5.4.

Table 5.4 Prediction for drawing values

Specimens	*a (mm)*	*b (mm)*	*c (mm)*	*d (mm)*
DD1511	40	30	40	40
DD1531	40	30	40	50

The results of nodal Mises stress distribution on ETFE film and the deformation shapes according to the prediction are shown in Figure 5.9. The dash line shows the initial shape, while the solid line indicates the final shape in this figure. All elements of *DD1531* and *DD1511*specimens reaches to around the first yield point of ETFE film of *13.28MPa.*

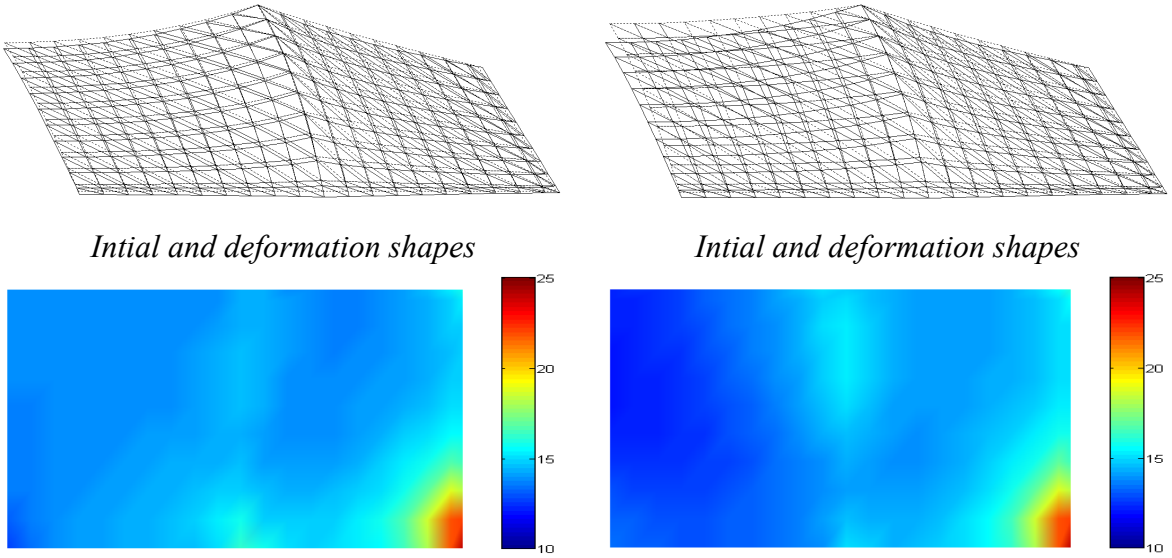

Intial and deformation shapes *Intial and deformation shapes*

Nodal Mises stress distribution *Nodal Mises stress distribution*

a. DD1511 *b. DD1531*

Figure 5.9 Distribution of predicted Mises stress on ETFE film

The relation between the Mises stress and equivalent strain of twelve elements in Figure 5.8 are represented in Figure 5.10. It should be noted that while the Mises stress is calculated by Eq. (5.2), the equivalent plastic strain is saved during the analysis by the suggested analytical method in Chapter 4.

$$S_{eq} = \sqrt{(S_{xx})^2 + \left(S_{yy}\right)^2 - S_{xx}S_{yy} + 3\left(S_{xy}\right)^2} \tag{5.2}$$

where, S_{xx}, S_{yy} and S_{xy} are the 2^{nd} Piola-Kirchhoff stresses in *x, y* local coordinate of membrane elements and the shear stress, respectively.

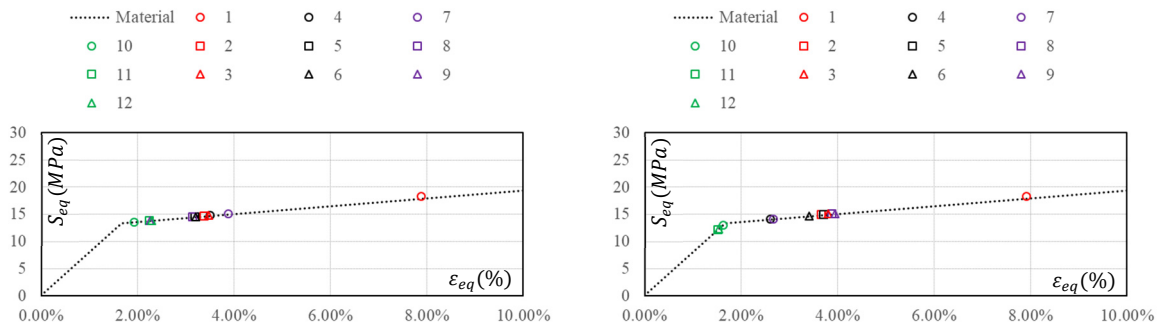

a. DD1511 *b. DD1531*

Figure 5.10 Relations between Mises stresses and equivalent strains

In Figure 5.10, the dash line shows the material model of ETFE film, while the color maker

points present the results of the prediction of twelve elements. Figure 5.10 shows that the equivalent strains of element *1* are smaller than *10%*. Therefore, the drawing value of *b* is determined as *30mm*. In case of *DD1531* specimen, the Mises stresses of element *10*, *11*, *12* can be increased up to the first yield point of ETFE film by the increment of *d* values. However, the limit ratio of drawing values *d/c* should be suggested because of the absence of wrinkling. This problem will be discussed in the next part.

(b) Prediction for the absence of wrinkling

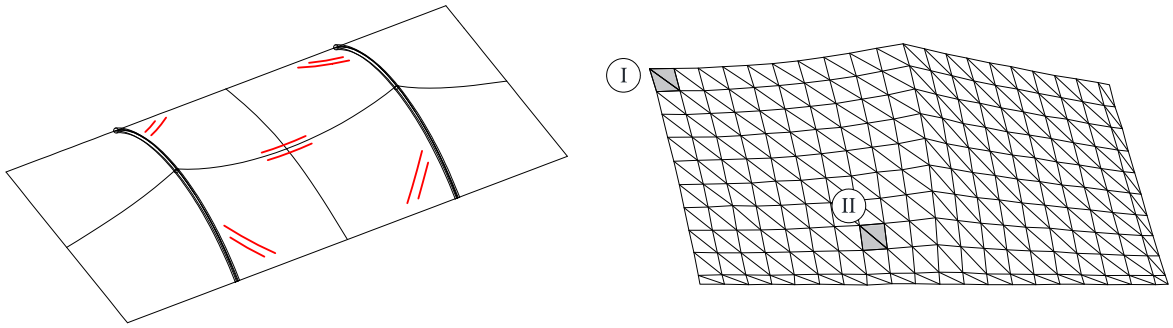

a. Position of wrinkling in PD15 specimens *b. Representative elements*

Figure 5.11 Observed representative elements in prediction of wrinkling

Figure 5.11b shows the two observed elements for the prediction of wrinkling which correspond to the occurred position of wrinkling in the stretch fabrication experiments of Chapter 3. The drawing values of *a*, *b* and *c* remain constant as shown in Table 5.4 in this prediction, while the value of *d* is increased from *c* to *2c*. The minimum principal stresses and strains, which are calculated by Eq. (5.3), are shown in the relation with the ratio *d/c* in Figure 5.12.

$$S_{min} = \frac{S_{xx} + S_{yy}}{2} - \sqrt{\left(\frac{S_{xx} - S_{yy}}{2}\right)^2 + {S_{xy}}^2}$$
$$\varepsilon_{min} = \frac{\varepsilon_{xx} + \varepsilon_{yy}}{2} - \sqrt{\left(\frac{\varepsilon_{xx} - \varepsilon_{yy}}{2}\right)^2 + \left(\frac{\varepsilon_{xy}}{2}\right)^2} \quad (5.3)$$

where, S_{xx}, S_{yy} and S_{xy} are the *2nd* Piola-Kirchhoff stresses in *x, y* local coordinate of membrane elements and the shear stress, respectively, ε_{xx}, ε_{yy} and ε_{xy} are Green-Lagrange strains in *x, y* local coordinate of membrane elements and the shear strains, respectively. All of these values are obtained by the analytical method in Chapter 4.

In Figure 5.12, while the dash lines show the results of minimum principal stresses, the solid lines present the results of minimum principal strains. Moreover, the lines with circle, square

and triangle markers indicate the prediction results of *PD15, DD1511* and *DD1531* respectively. It should be noted that the *PD15* is the specimen in previous experiments which had the plane strips for the middle part.

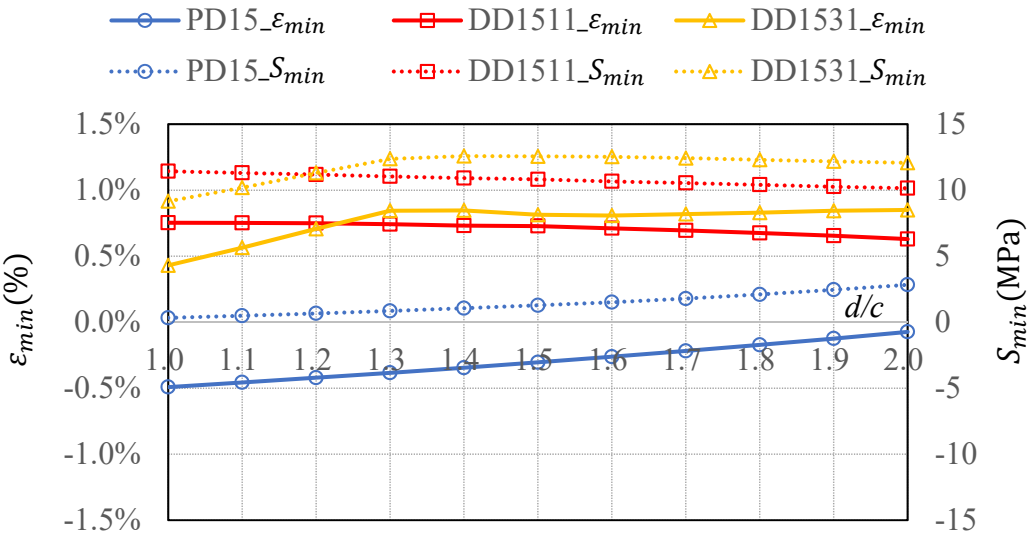

a. Elements I

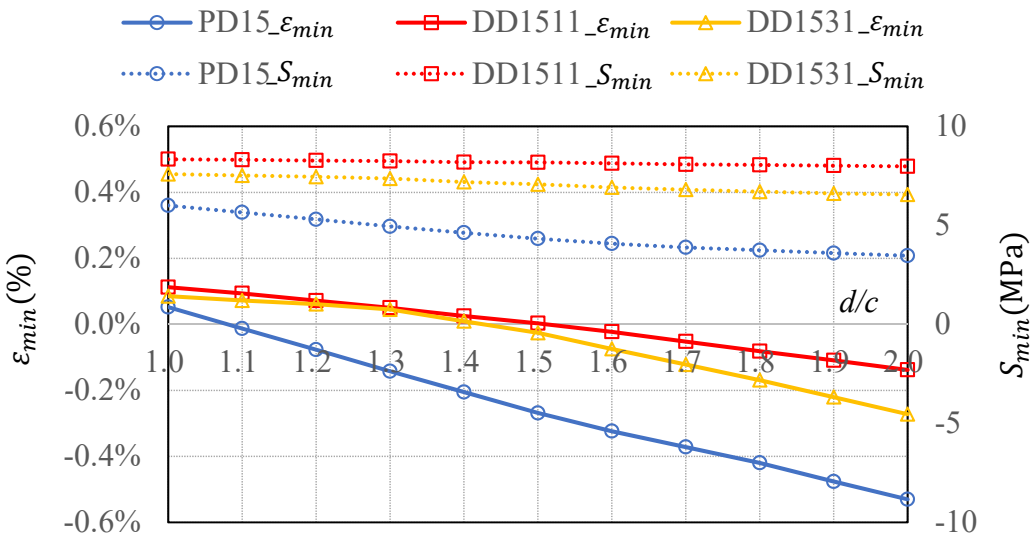

b. Elements II

Figure 5.12 Minimum principal stresses and strains

Up to now several wrinkling criteria have been proposed. Generally, three main types can be categorized: the first is based upon the principal stresses [PC88], [BT92]; the second upon the principal strains [RM82]; the third upon the principal stress and strains [DR87]. However, this prediction is based upon the principal minimum strains. It can be seen from Figure 5.12 that although the minimum principal stresses of elements *I* and *II* are larger than zeros in case of

PD15, the minimum principal strains of these elements smaller than zeros for 1.5 of *d/c* (*PD15b*) and *2.0* (*PD15a*). As a result, the wrinkling was observed in the experiments of section 3.3.3. Therefore, the ratio between *d* and *c* for *DD1511* and *DD1531* specimens are controlled smaller than *1.5* and *1.4*, respectively in order that the minimum principal strains of element *II* are larger than zeros.

(c) The process of drawing

The experiments were carried out in four steps according to the predictions, and the values of drawing boundary are shown in Table 5.5.

Table 5.5. The process of experiments

	a (mm)	*b (mm)*	*c (mm)*	*d (mm)*
Step 1	*10*	*10*	*10*	*10*
Step 2	*20*	*15*	*20*	*20/25**
Step 3	*30*	*20*	*30*	*30/40**
Step 4	*40*	*30*	*40*	*40/50**

** The first value was used for DD1511a/b, while the second value was used for DD1531a/b*

5.3.3. Smooth curved surface

The 3D curved surfaces without wrinkling could be established by the suggested drawing values as shown in Table 5.5. Figure 5.13 represents the initial and final shapes throughout four specimens.

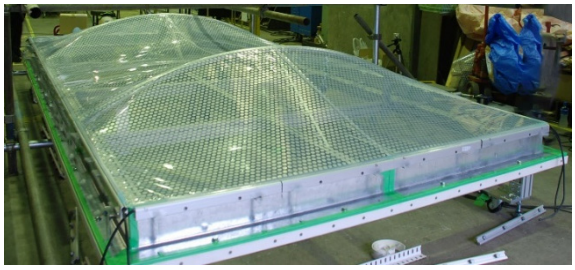

a1. DD1511a, Initial shape

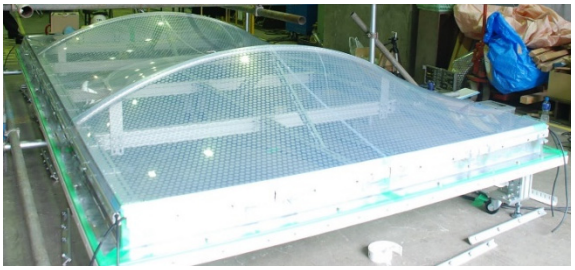

a2. DD1511a, Final shape

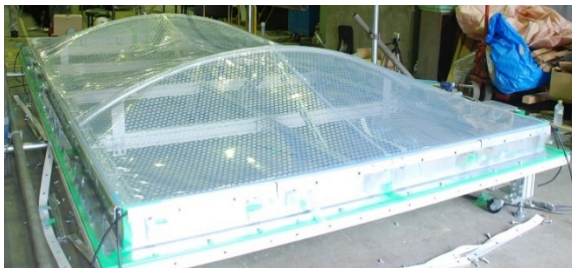

b1. DD1511b, Initial shape

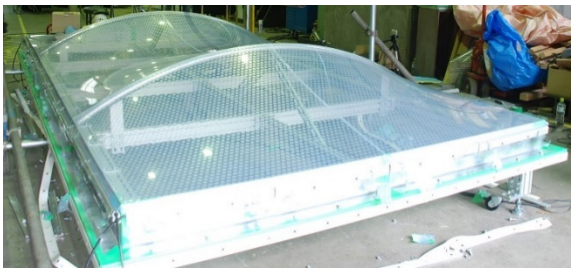

b2. DD1511b, Final shape

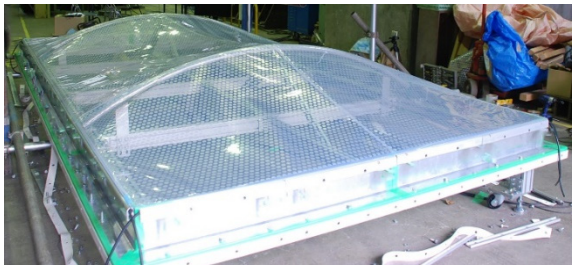

c1. DD1531a, Initial shape

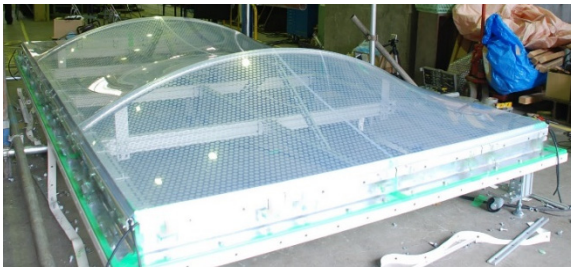

c2. DD1531a, Final shape

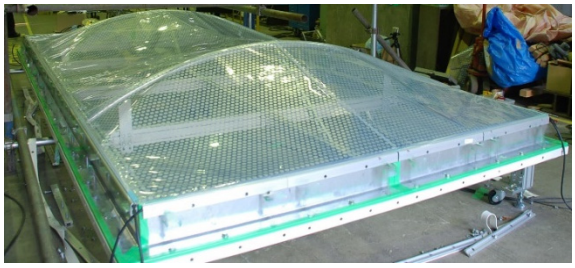

d1. DD1531b, Initial shape

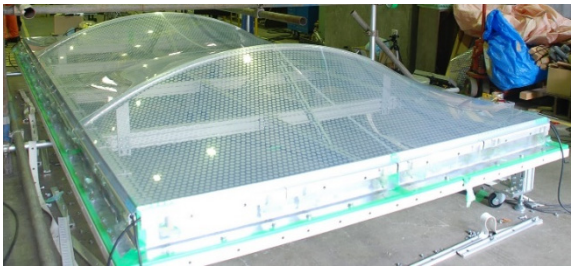

d2. DD1531b, Final shape

Figure 5.13 Smooth three-dimensional curve surfaces

5.3.4. Stress distributions on the final curved surfaces

The Mises stresses of the film after the drawing boundary process are checked by both the measurement in experiments and the analytical method. In the experiments, the lengths of four edges and two diagonals of part *A* and part *B* as shown in Figure 3.8 were measured. The paper tape and caliper were used to measure these lengths to increase the precision in the experiments of this chapter. The results of Green-Lagrange strains of part *A* and *B* are shown in Figure 5.14 at the final step.

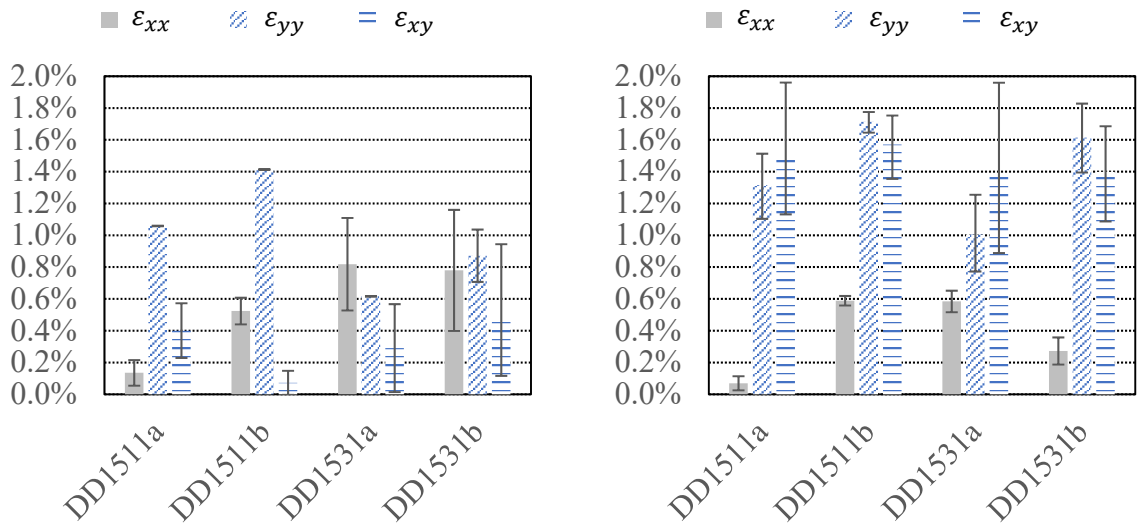

a. Part A *b. Part B*

Figure 5.14 Green-Lagrange strains of part A and part B

In Figure 5.14, the solid bar shows the strain in long direction (*MD*), while the diagonal pattern and horizontal pattern columns presents the strains in short direction (*TD*) and shear strain, respectively. At part *A*, strain in *TD* direction ε_{yy} is around five times larger than strain in *MD* direction ε_{xx} in case of *DD1511* specimens, while the *MD* and *TD* strains in case of *DD1531* specimens are almost the same. The length of middle cutting pattern line was *2042mm* for *DD1531* as shown in Figure 5.6. This length was larger than *2009mm* of *DD1531*. Therefore, the strain in *MD* direction ε_{xx} of part *A* of *DD1531* was larger than that of *DD1511* for the same values of drawing boundary. The same phenomenon was observed in *TD* direction. According to these observed strains, the 2^{nd} Piola-Kirchhoff stresses of part *A* and part *B* can be obtained as same as section 3.3.2.

In analysis, the suggested analytical method of Chapter 4 is used for the *0.3* of the friction coefficients between ETFE film and galvanized steel arch. The models of a quarter of specimens are same with section 5.3.2. However, the motions of offset points, which were observed in the experiments, are used directly as the input forced displacements conditions. The results of

relation between the drawing values of *a*, *b*, *c* and *d* and the movements of special offset points *1**, *2**, *3** and *4** (Figure 3.16) during the experiments are shown in Figure 5.15.

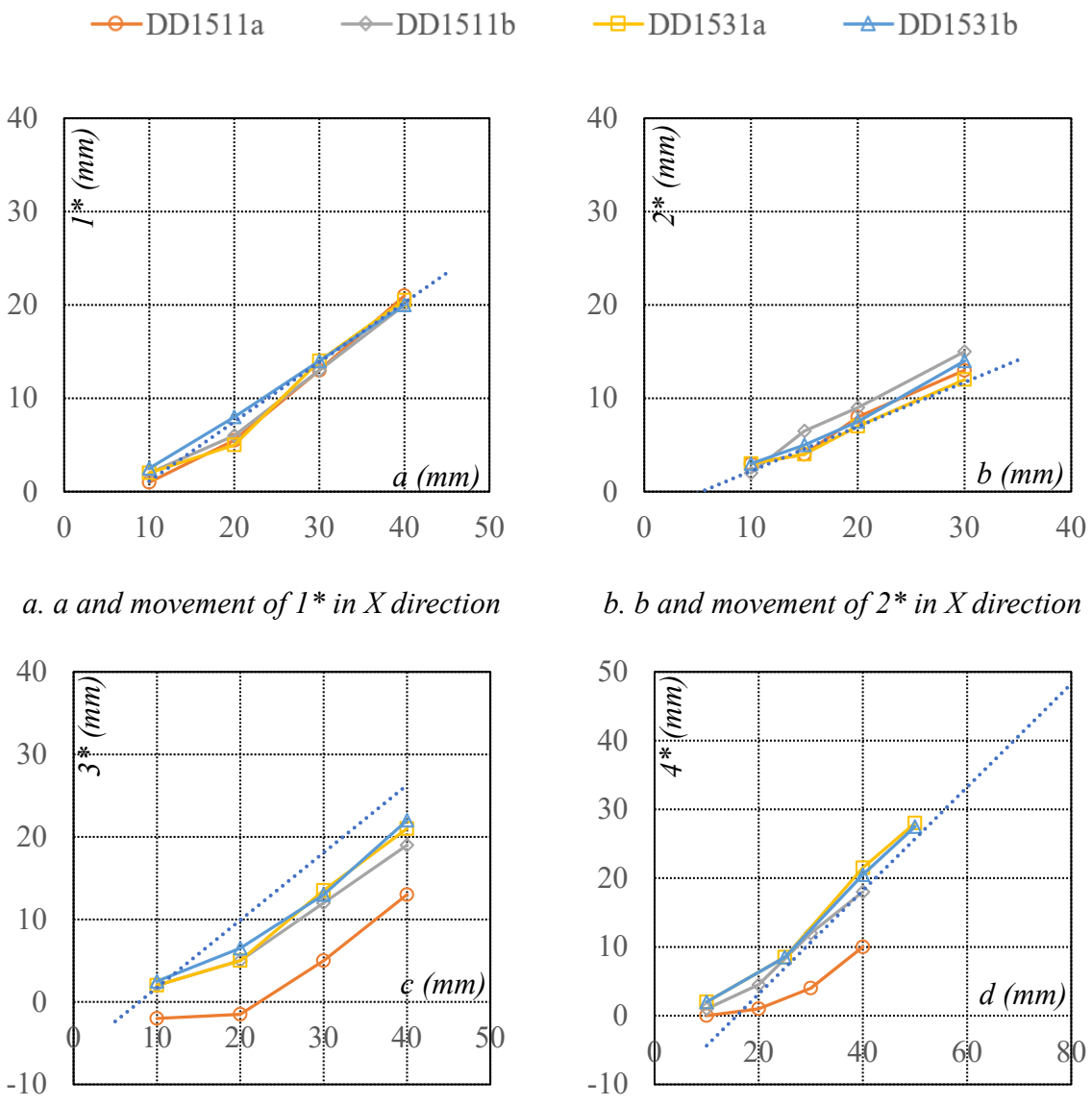

a. a and movement of 1 in X direction*

b. b and movement of 2 in X direction*

c. c and movement of 3 in Y direction*

d. d and movement of 4 in Y direction*

Figure 5.15 The movements of offset points during the experiments

In this figure, the solid lines with circle, diamond, square and triangle markers represent the results of the motion of offset points in *DD1511a/b* and *DD1531a/b*, respectively. The dash lines indicate the suggested functions which were suggested in section 3.3.4. Generally, the results obtained in the experiments of this chapter were in high agreement with the suggested functions.

The stress distribution in long direction (*MD*), short direction (*TD*), shear stress and Mises stress over *400* membrane elements at the final step are shown in Figure 5.16.

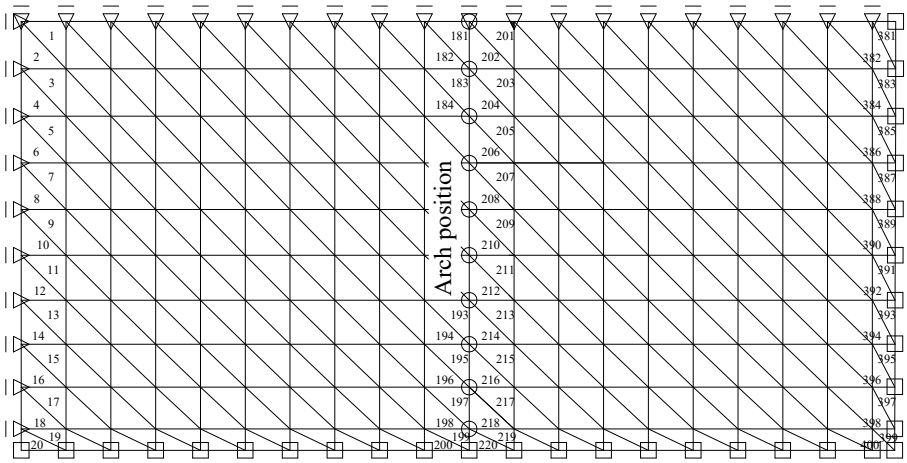

a. Element numbers

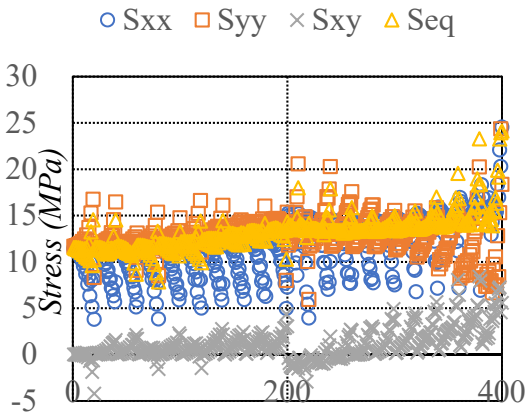

b. DD1511a

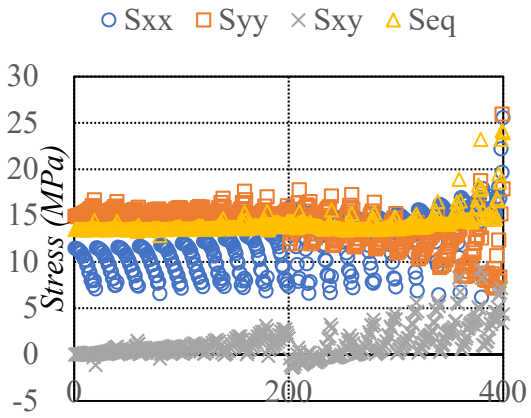

c. DD1511b

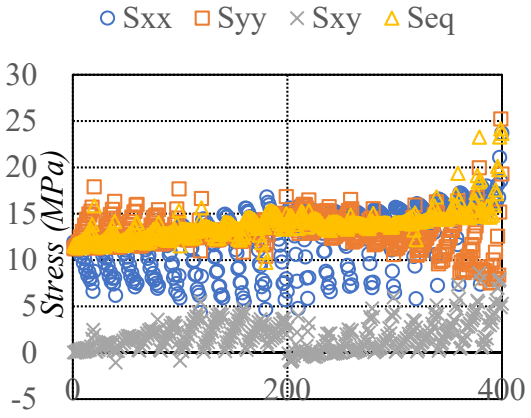

d. DD1531a

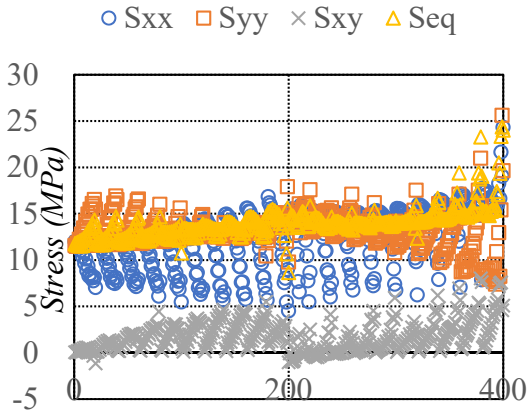

e. DD1531b

Figure 5.16 Stress distribution, TLGAP, $\mu = 0.3$

In Figure 5.6, the circle, square, *x* sign and triangle markers show the results of the final stress in *MD* direction, *TD* direction, shear stress and Mises stress. It can be seen that the final Mises stress on the film almost reaches the first yield point of ETFE film of *13.28 MPa*. The sufficient input prestress is confirmed by the suggested drawing values. The nodal distribution Mises stress are shown in Figure 5.17.

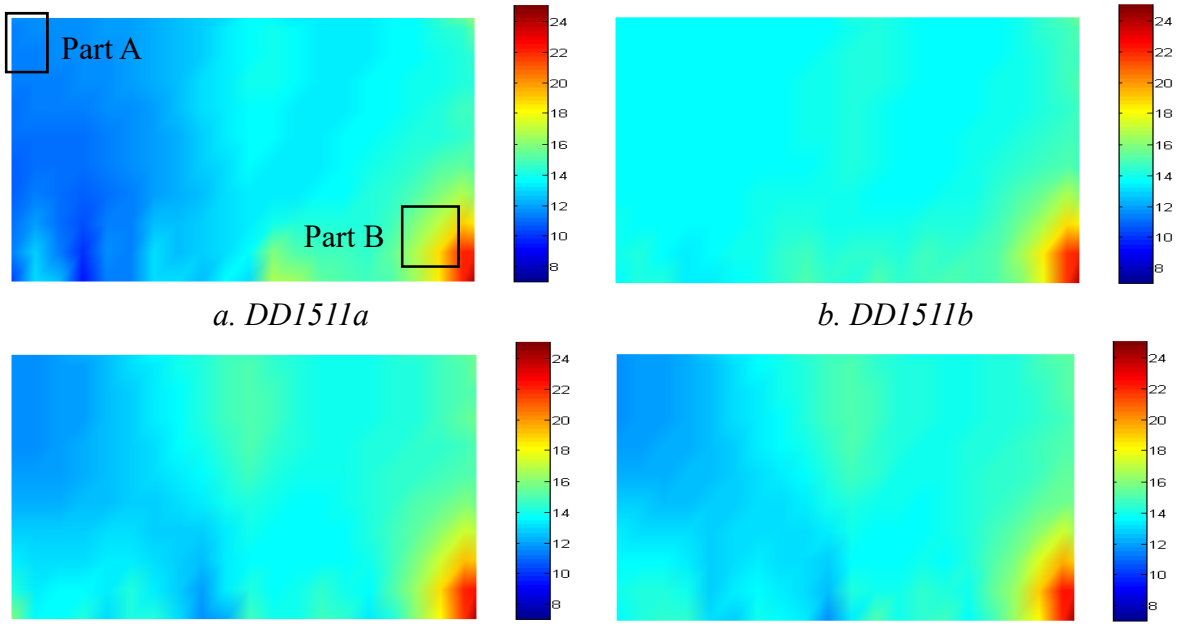

a. DD1511a *b. DD1511b*

c. DD1531a *d. DD1531b*

Figure 5.17 Mises stress distribution, TLGAP, $\mu = 0.3$

The results of Mises stress at part *A* and part *B* are shown in Figure 5.18 in both experiments and analyses. The dot pattern columns indicate the results of experiments, while the diagonal pattern columns show the results of analyses. Again, the high agreement between the suggested analytical results and the results of the experiments are observed, so the validity of suggested analytical method is confirmed additionally.

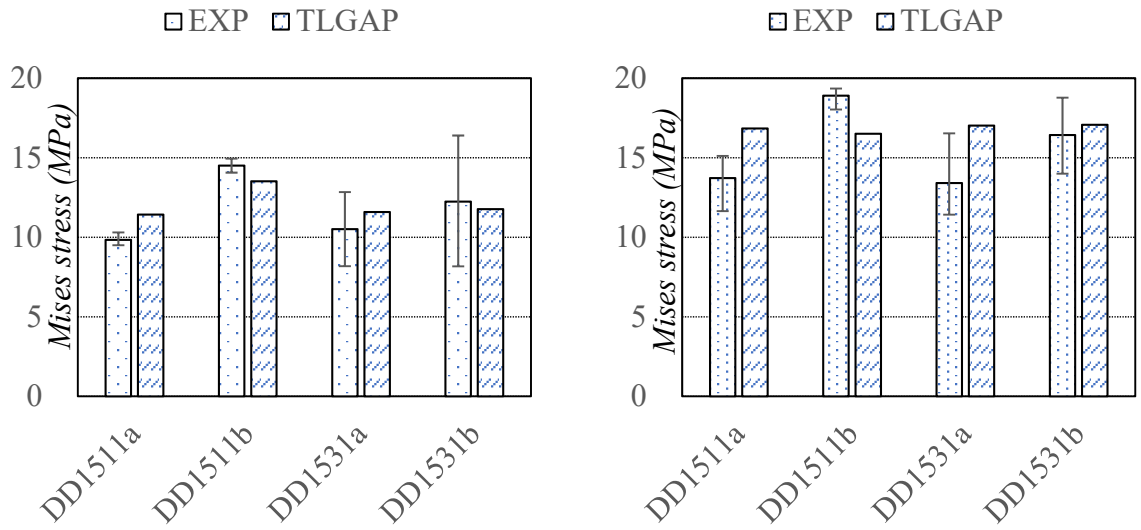

a. Part A *b. Part B*

Figure 5.18 Mises stress of part A and part B

At part *A*, the Mises stress of *DD1511* and *DD1531* specimens are almost the same in case the suggested drawing values of $\frac{d}{L}$ are 2% for *DD1511* specimens and 2.5% for *DD1531* specimens. These stresses are around 1.6 times larger than that of *PD15* specimens, although the drawing value of $\frac{d}{L}$ is 3% for *PD15*. The effectiveness of drape strips is confirmed. Here, *L* is span of this saddle type of structure, and the results of *PD15* can be referred in Figure 4.13.

5.3.5. Slide between ETFE and supporting arches

The initial and deformation shapes in the analyses are shown in Figure 5.19. The dash lines show the initial shape, while the solid lines indicate the deformation shape in this figure. The slides between ETFE film and the galvanized steel arches were observed by both experiments and analyses at five special position as shown in Figure 3.18. The results of these observations are shown in Figure 5.20. It should be noted that the slides were observed in *X* and *Y* directions (Figure 3.18) in the experiment, while they were obtained in x_0 and y_0 directions (Figure 4.7) in the analyses.

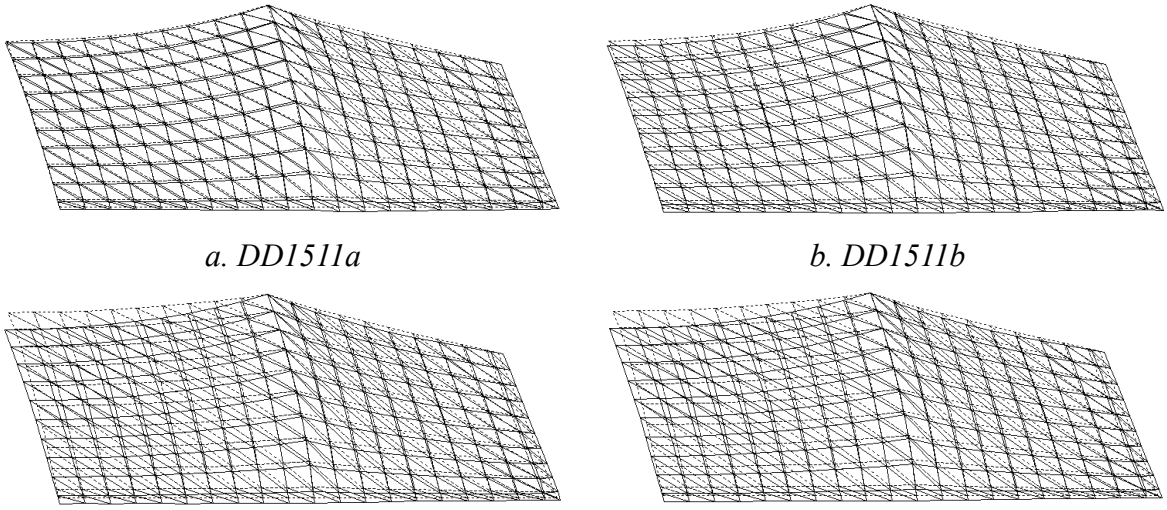

a. DD1511a *b. DD1511b*

c. DD1531a *d. DD1531b*

Figure 5.19 Initial and deformation shapes, TLGAP, $\mu = 0.3$

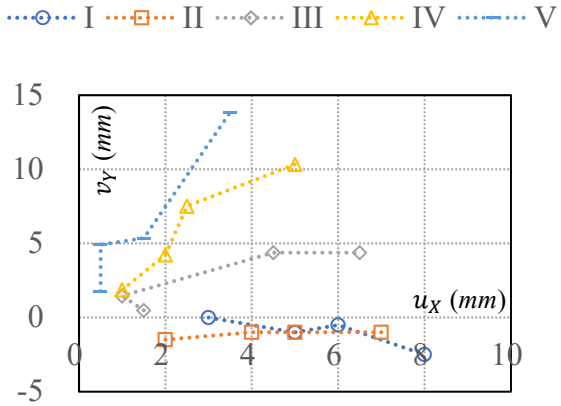

a1. DD1511a, Experiment

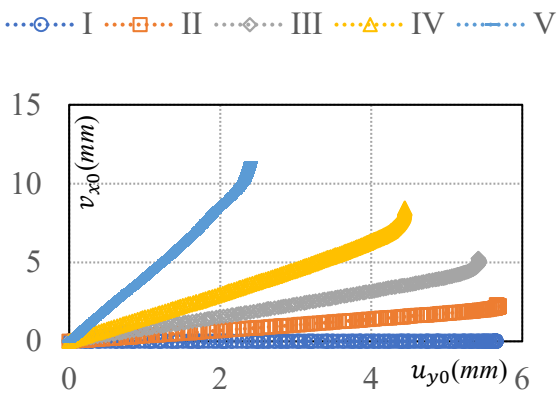

a2. DD1511a, TLGAP

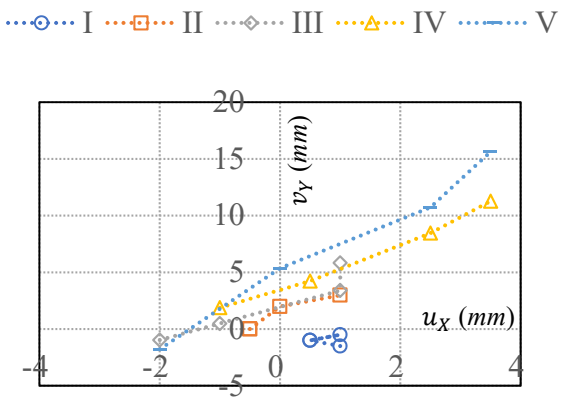

b1. DD1511b, Experiment

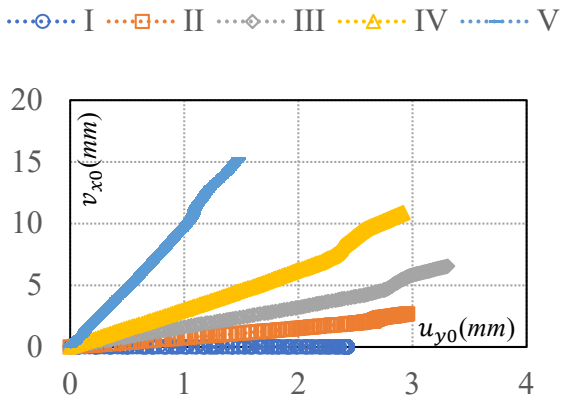

b2. DD1511b, TLGAP

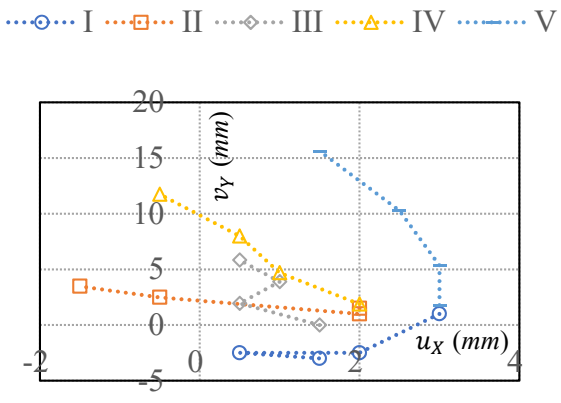

c1. DD1531a, Experiment

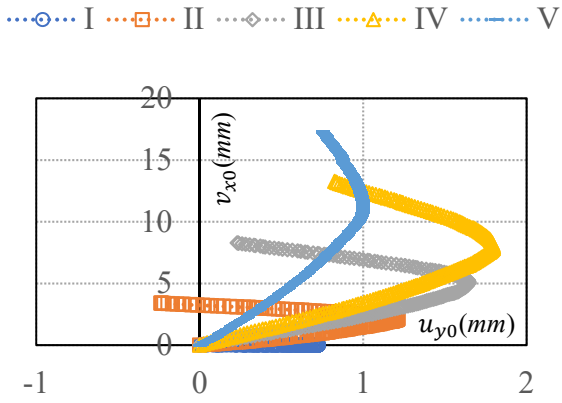

c2. DD1531a, TLGAP

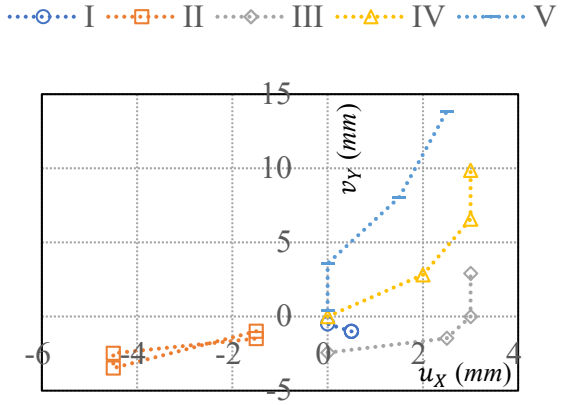

d1. DD1531b, Experiment

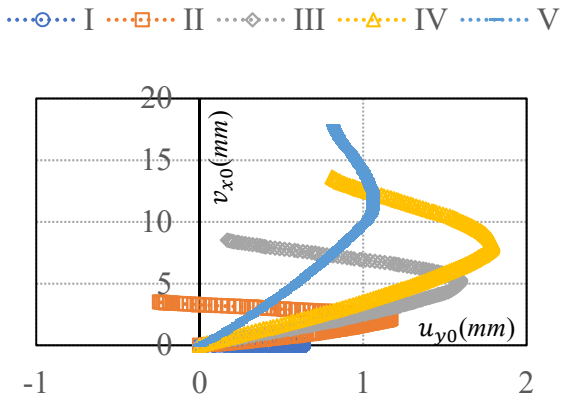

d2. DD1531b, TLGAP

Figure 5.20 Slide history between ETFE and steel arches in both experiments and TLGAP, $\mu = 0.3$

In Figure 5.20, the dash lines with circle, square, diamond, triangle and minus markers present the results at point *I*, *II*, *III*, *IV* and *V*, respectively. Again, the high agreement can be seen between the experiments and the analyses. The slide values in x_0 and y_0 directions in analyses are transformed into the *X* and *Y* directions and compared with the results of the experiments. Figure 5.21 shows these comparisons.

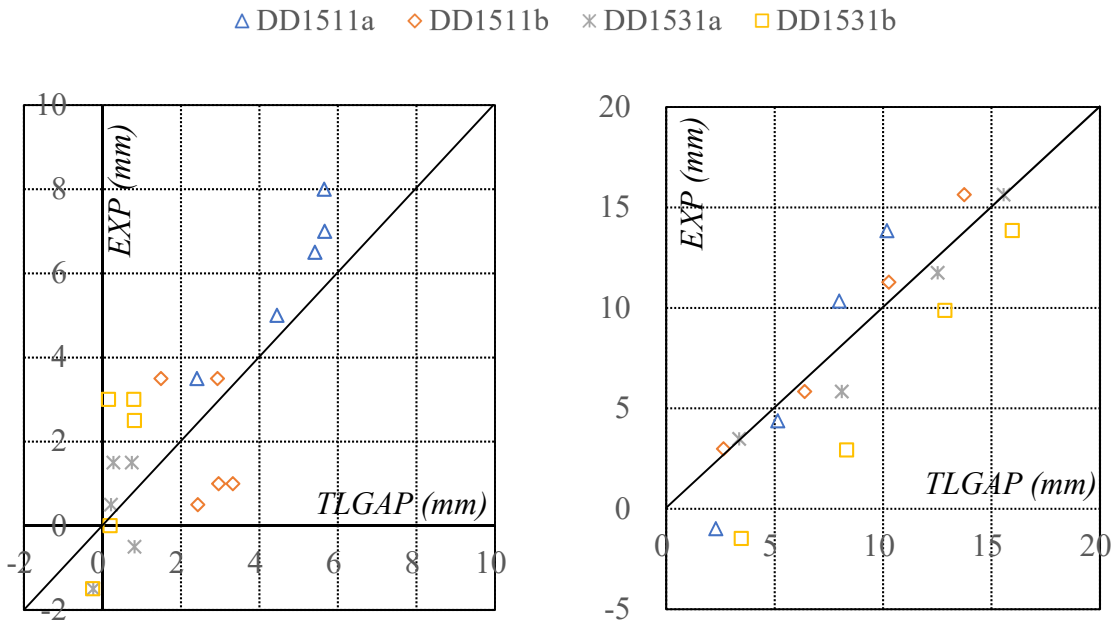

a. Slide in X direction *a. Slide in Y direction*

Figure 5.21 The comparison of slide values between experiments and TLGAP, $\mu = 0.3$

The horizontal axis presents the results of analyses, while the vertical axis indicates the results of experiments. It can be seen that the analyses are in high agreement with the observed values of experiments in both *X* and *Y* direction. The validity of suggested analytical method of Chapter 4 is confirmed additionally.

5.3.6. Saddles heights

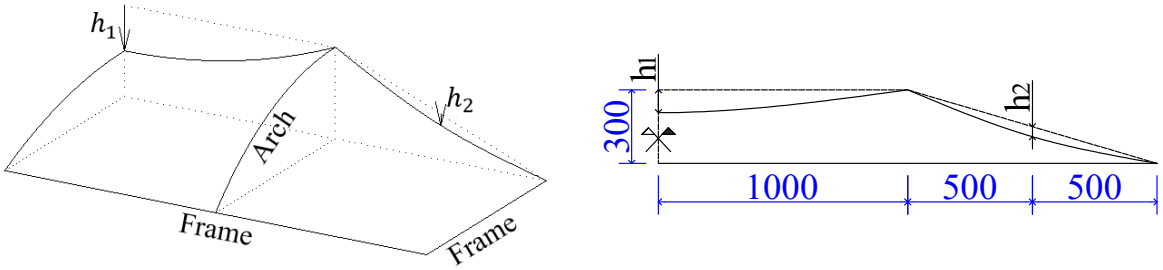

a. 3D view *b. Elevation view*

Figure 5.22 Saddle heights
(All dimensions are in millimeter)

The saddle heights h_1 and h_2, which are presented in Figure 5.22, are measured by the carpenter's square with precision of *0.5mm* at the first and final steps of experiments. The results of those heights are shown in Figure 5.23 versus the target heights of minimum surface.

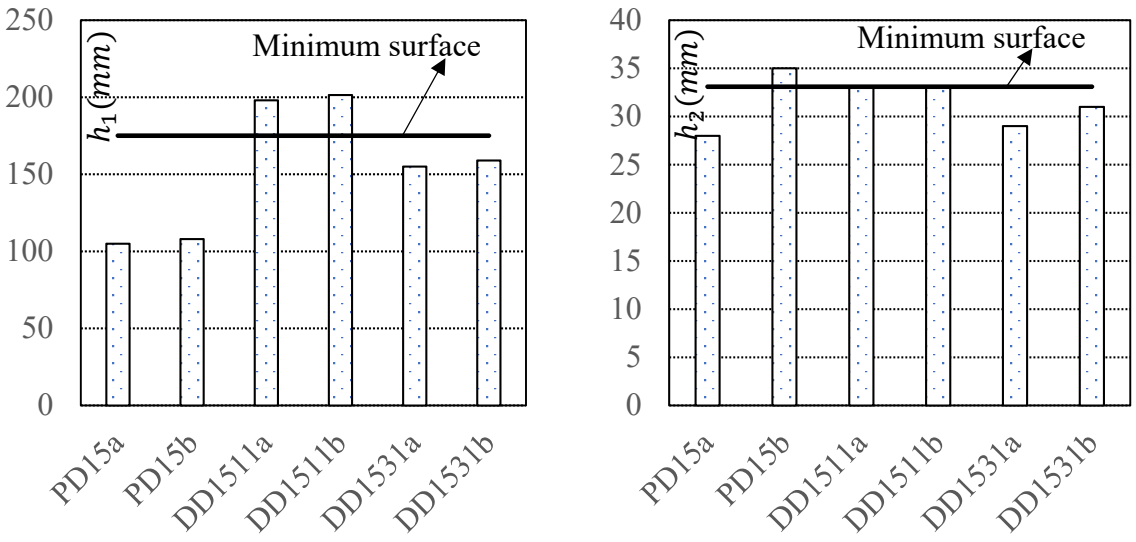

a. $h_1(mm)$ *b.* $h_2(mm)$

Figure 5.23 The results of saddle heights

The saddle height h_1 of specimens *DD1511a/b* at the final shape was higher than the results of minimum surface, while this height of specimens *DD1531a/b* moved toward to the minimum surface results. Therefore, the prescribed stress ratios in form finding analysis should be chosen depending on the viewpoints of architecture. In addition, the final shapes of *PD15*, which used the plane strips for the middle part, were far from the results of minimum surfaces. In conclusion, when the rise ratio of saddle type of membrane structure is high, the drape strips

for the middle part are strongly recommend.

The saddle height h_2 of four specimens (*DD1511a/b*, *DD1511a/b*) moved toward to the height of minimum surface, and the same results were observed in case of *PD15* specimens. The prescribed stress ratio between *MD* and *TD* directions of *3:1* in form finding analysis for the corner part was accepted highly.

5.4 Pressurization experiments

5.4.1. The setup of experiments and results

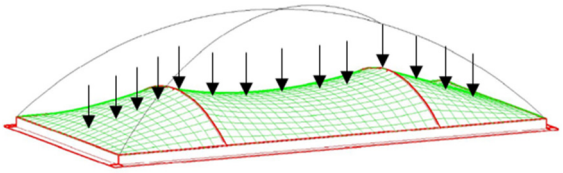

a. Compressor for pressurization

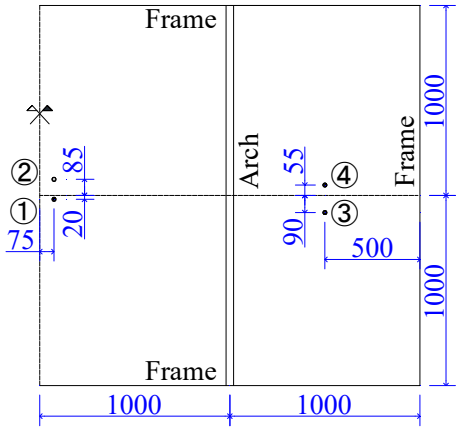

b. Setup of laser displacement meters

Figure 5.24 The overview of pressurization tests

The pressurization test is investigated to confirm the strength of the ETFE membrane structure after the introduced prestress stage. This test was carried out after around ten hours of the stretch fabrication period. The internal pressure was input by the compressor. The process of pressure is described as follow: *0kPa* → *0.5kPa* → *0kPa* → *1kPa* → *0kPa* → *1.5kPa* → *0kPa* → *2kPa* → *0kPa.* The vertical displacements of ETFE film were measured by the laser displacement meters during the pressurization test. The setup of laser meters is described in Figure 5.24b. Figure 5.25 indicates the shapes of specimen *DD1531b* at the initial pressure of *0kPa* and the final pressure of *2kPa*.

The relation between pressure and vertical displacements of positions ① and ④ are shown in Figure 5.26.

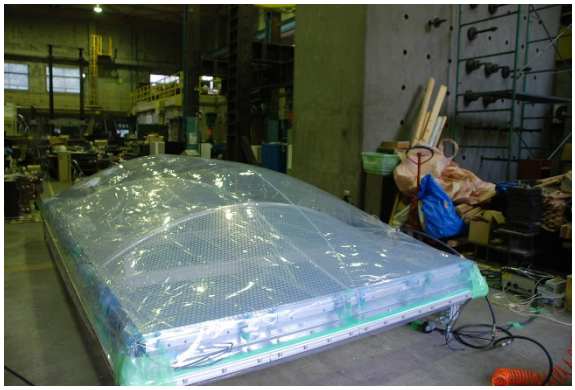

a. Initial shape at 0 kPa

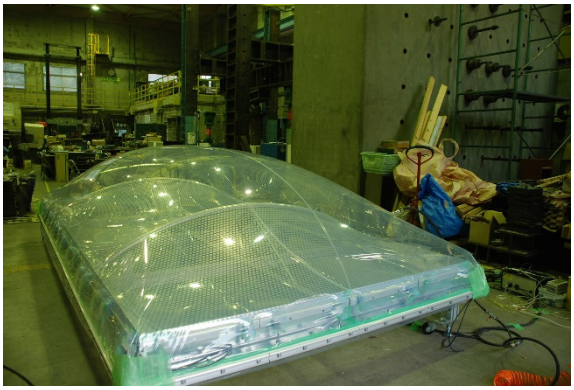

b. Final shape at 2 kPa

Figure 5.25 The photos of pressurization tests, DD1531b

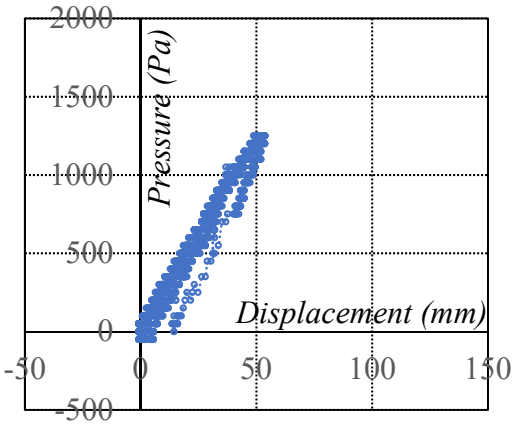

a1. DD1511a

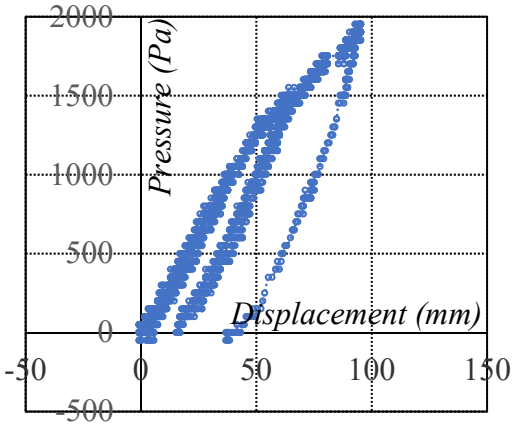

a2. DD1511b

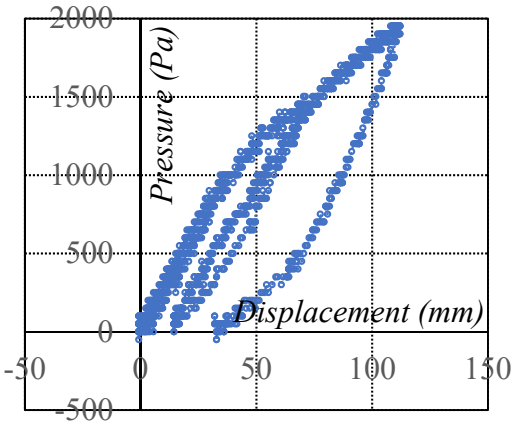

a3. DD1531a

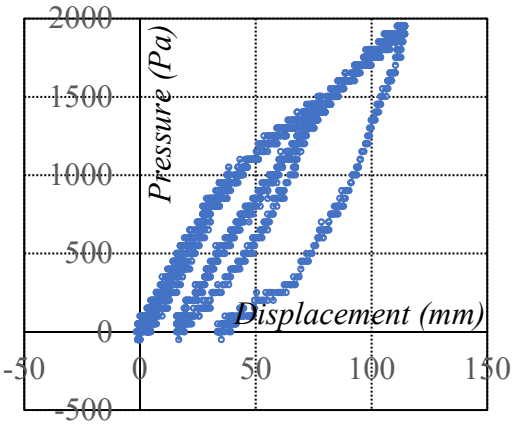

a4. DD1531b

a. Relation between pressure and vertical displacement of ① position

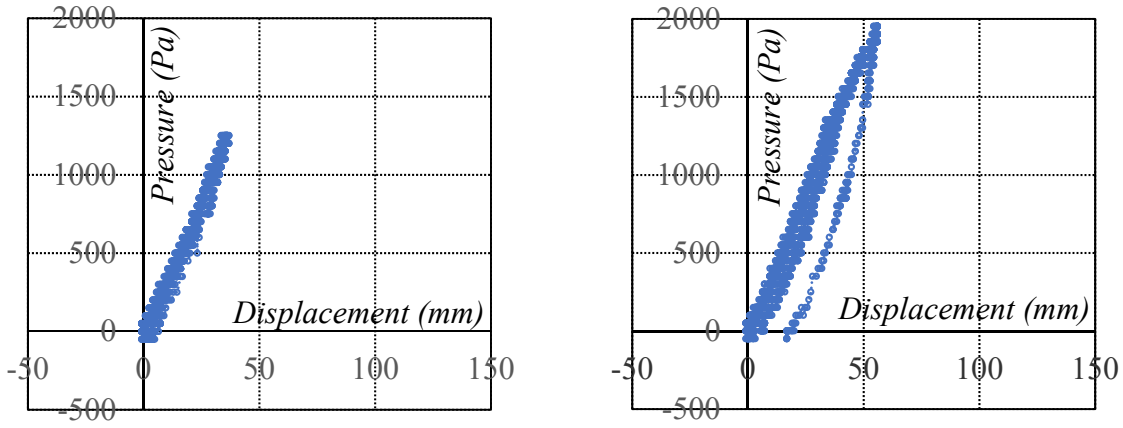

b1. DD1511a

b2. DD1511b

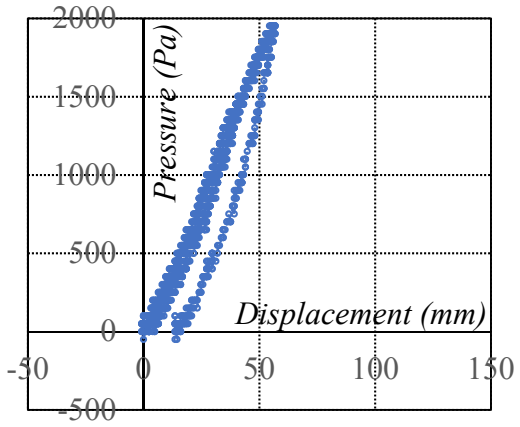

b3. DD1531a

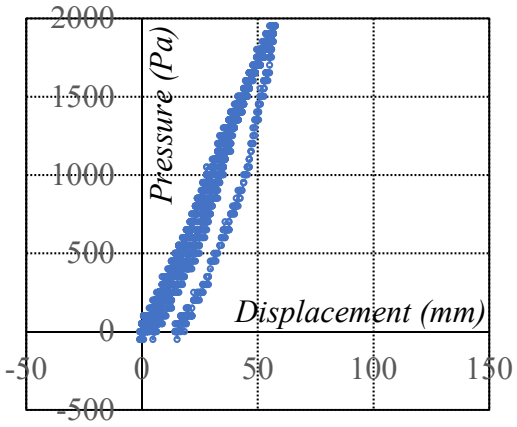

b4. DD1531b

b. Relation between pressure and vertical displacement of ④ position

Figure 5.26 Pressurization test results

In case of specimen *DD1511a*, the air was escaped at the corner of specimens because of the setup of experiments. As a result, the experiment was interrupted at the pressure of around *1.3kPa*. The gum tape was used to solve this problem in the rest of experiments, and the target of pressure of *2.0kPa* could be reached.

The residual displacements were observed at very high of pressure of *1.5kPa*. The sufficiency of introduced prestress was confirmed. The stiffness of structure at the corner part are larger than the middle part because the dimensions of corner part (*1mx2m*) are smaller than middle part (*2mx2m*), and the introduced prestress of the corner part are larger than that of the middle part (Figure 5.15). In addition, the reduction of the rigidity of structures can be seen at the pressure of 1.3*kPa* from those relation curves.

5.4.2. Effectiveness of using drape strips

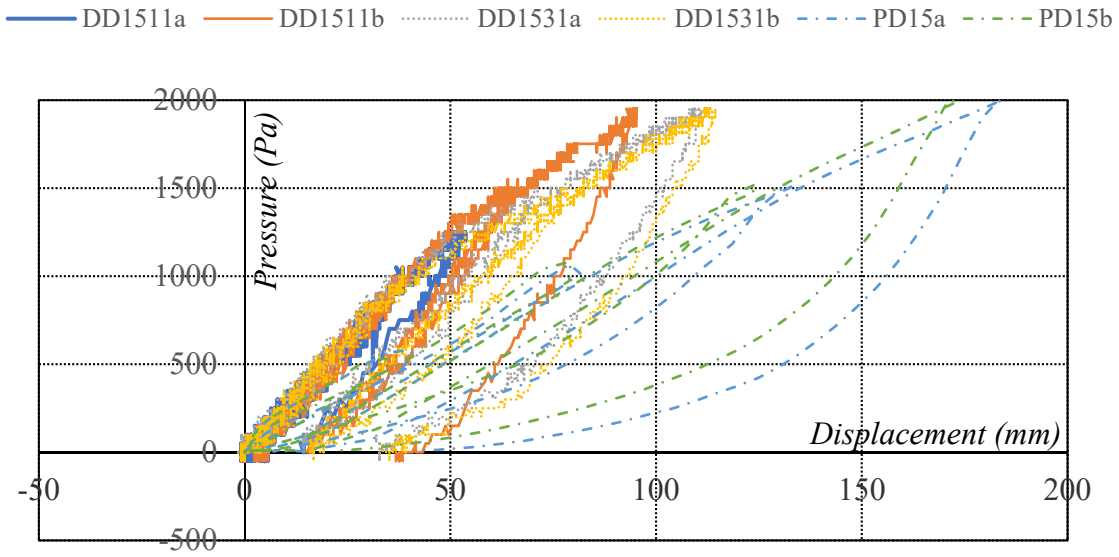

a. Relation between pressure and displacement at ① position over six specimens

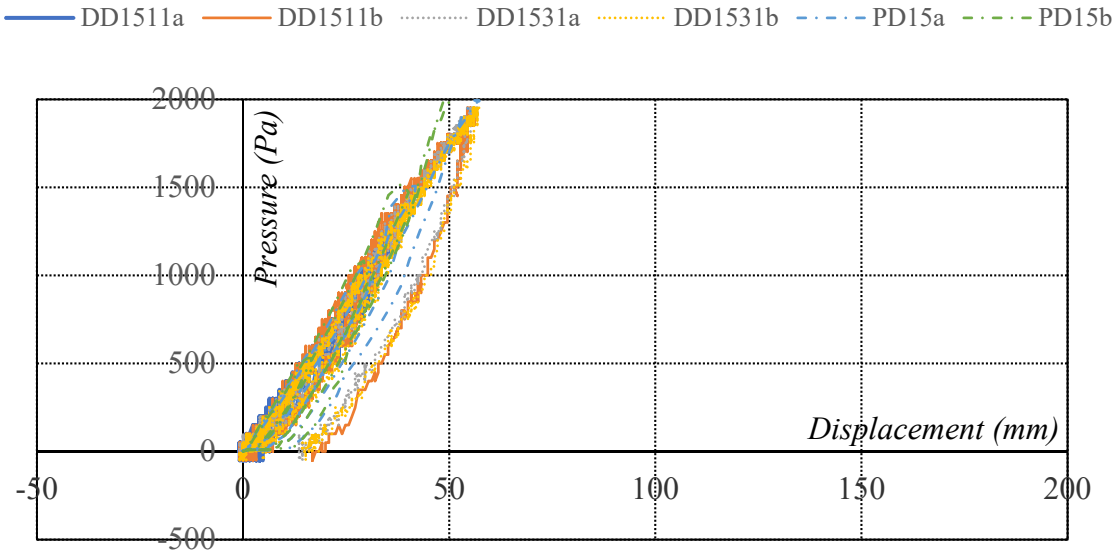

b. Relation between pressure and displacement at ④ position over six specimens

Figure 5.27 Comparison between plane strips and drape strips in pressurization test

The using of drape strips for the middle part of the saddle type of membrane structure introduced two advantages: (1) the absence of wrinkling after stretch fabrication period; (2) the sufficiency of introduced prestress for the middle part. The former advantage was confirmed by

the results stretch fabrication test in Figure 5.13. The later advantage is confirmed additionally by the comparison in the pressurization test. In Figure 5.27, the solid and dotted lines show the results of *DD1511*, *DD1531*, respectively, while the dot-and-dash lines present the results of *PD15*. It should be noted that *PD15* were the specimens which used plane type of cutting pattern for the middle part of previous experiments. In Figure 5.27a, the stiffness of the structures for the middle parts of *DD1511* and *DD1531* specimens was larger than that of *PD15* specimens. The reason can be explained by the enough pre-stress of tension and the final smooth curved surface. In contrast, the stiffness of the structures for the corner parts was the same over specimens because the same cutting pattern types were used in this part.

5.4.3. Modeling of pressurization tests

The assumptions for the models of pressurization test are:

(a) The initial shapes are obtained directly from the final shapes of the models of stretch fabrication test in section 5.3.4.

(b) The initial prestresses are also obtained directly from the results of analyses of stretch fabrication test. This assumption ignores the effect of viscous properties of ETFE film or the reduction of prestress.

(c) The material model for ETFE film is considered in two cases. The material model remains constant as shown in the stretch fabrication test for *case 1*, while the first yield point of ETFE is assumed to increase for *case 2*. Table 5.6 shows the assumption of ETFE model in two cases. While the *Table 5.6a* present the model in *case 1*, which is reminded for the convenience, the *Table 5.6b* indicates the material model in *case 2*.

Table 5.6. The assumption models for ETFE film

Table 5.6a Case 1

Young modulus	*800 MPa*
First yield point	*13.28 MPa*
Second yield point	*23.04 MPa*
First strain hardening ratio	*80.5 MPa*
Second strain hardening ratio	*3.0 MPa*

Table 5.6b Case 2

Young modulus	*800 MPa*
First yield point	*15 MPa*
Second yield point	*23.04 MPa*
First strain hardening ratio	*66 MPa*
Second strain hardening ratio	*3.0 MPa*

It should be noted that the first yield point of ETFE film depends not only on the temperature but also on the strain-rate [CG11], [MK08]. Therefore, the increments of the first yield point in *case 2* can be explained by two reasons: (1) The stretch fabrication affected to the first yield point. As it can be seen from Figure 5.16, all part of ETFE film reached the Mises stress of around *15MPa* after the stretch fabrication test; (2) The ETFE film in stretch fabrication test had the higher first yield point than that of the uniaxial test. The results of analysis model in

pressurization tests are shown in Figure 5.28 regards of the results of experiments. It should be noted that the static friction coefficient between ETFE and steel galvanized arch is *0.3* in these analyses.

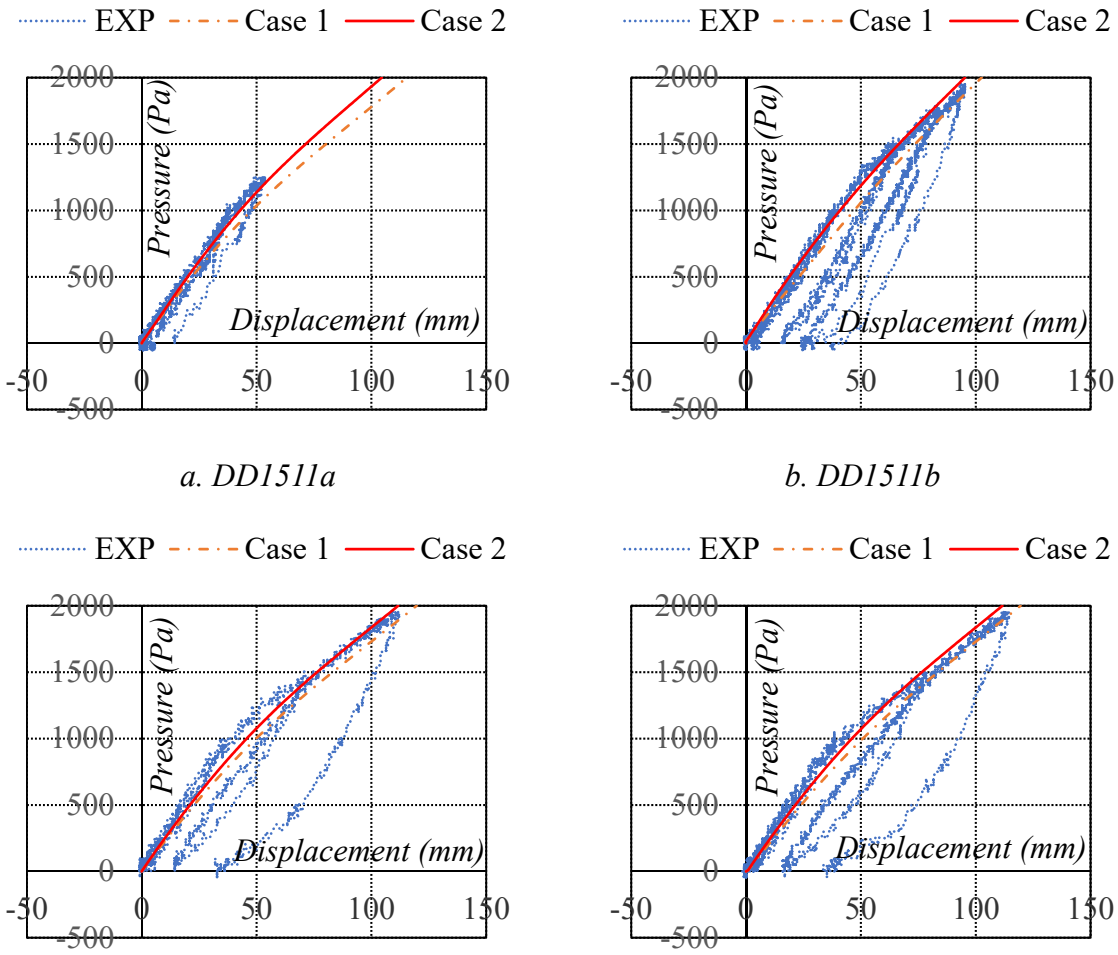

a. DD1511a *b. DD1511b*

c. DD1531a *d. DD1531b*

Figure 5.28 The analytical results of pressurization test

In Figure 5.28, the dash line shows the results of pressurization tests, while the dash-dot and solid lines present the results of analyses for *case 1* and *case 2* models of material, respectively. As we can see in Figure 5.28, the results of analyses of *case 2* and the results of the experiments are in higher agreement than that of *case 1*. The increment of the first yield point can be confirmed by those results.

The next part will investigate the slide between the ETFE film and galvanized arch in pressurization tests. The deformation shapes of specimens for *case 2* of material model are shown in Figure 5.29. In this figure, the dash lines indicate the initial shape, while the solid line represent the deformation shape. The slide between the ETFE and arch was so small in these analyses.

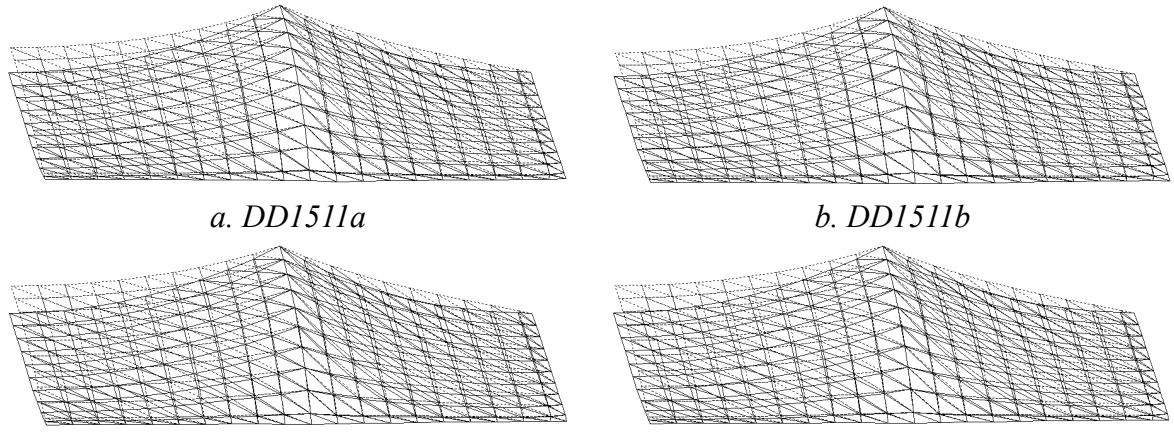

a. DD1511a *b. DD1511b*

c. DD1531a *d. DD1531b*

Figure 5.29 Initial and deformation shapes in pressurization tests, TLGAP, $\mu = 0.3$

Figure 5.30 shows the slide at five special contact points (Figure 3.17) in x_0 and y_0 directions (Figure 4.7) during the modeling of pressurization tests. It can be seen that the slide values at points *I* and *II* are almost zeros, while the slide values at point *III*, *IV*, *V* are smaller than *2mm*. The pressure on the ETFE film at both sides of arch are almost the same during the pressurization, so the slide between the ETFE and arch are small in those tests.

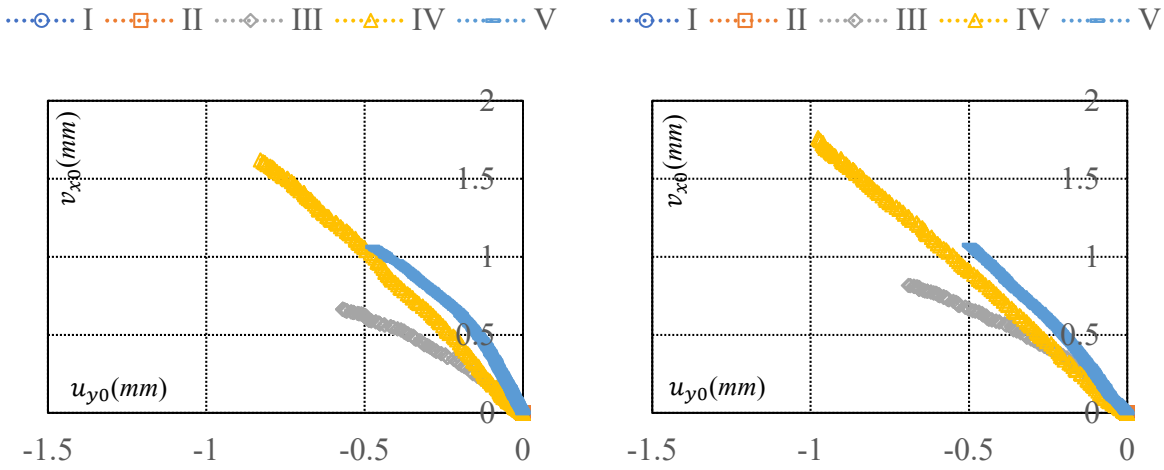

a. DD1511a *b. DD1511b*

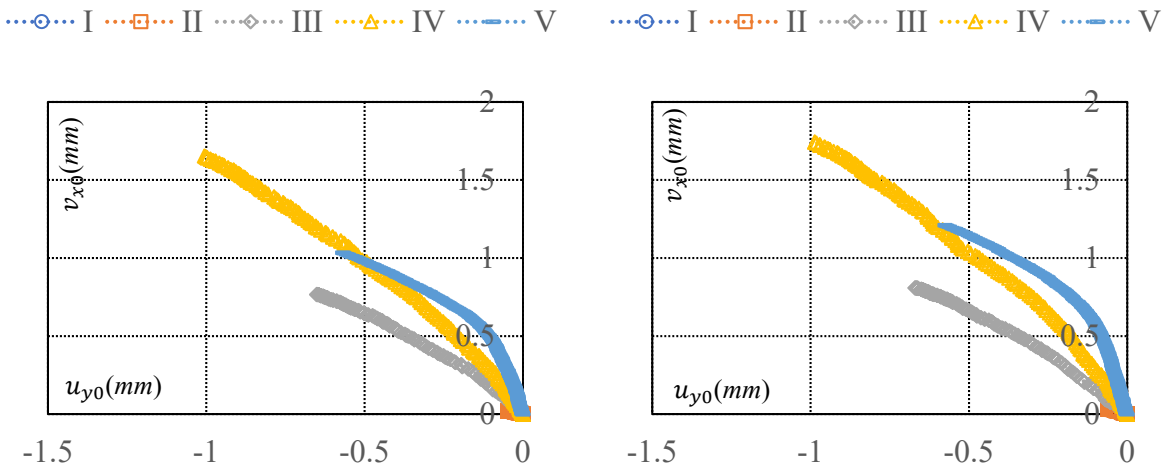

c. DD1531a *d. DD1531b*

Figure 5.30 Slide between ETFE and steel arch in pressurization tests

The Mises stress distribution for the *case 2* of ETFE material are shown in both cases: (1) slide consideration with static friction coefficient of *0.3*; (2) no slide or fixed conditions at the positions of arch in Figure 5.31. It can be seen from Figure 5.31 that the Mises stress distribution is almost the same regardless of the consideration of slide at the positions of arch.

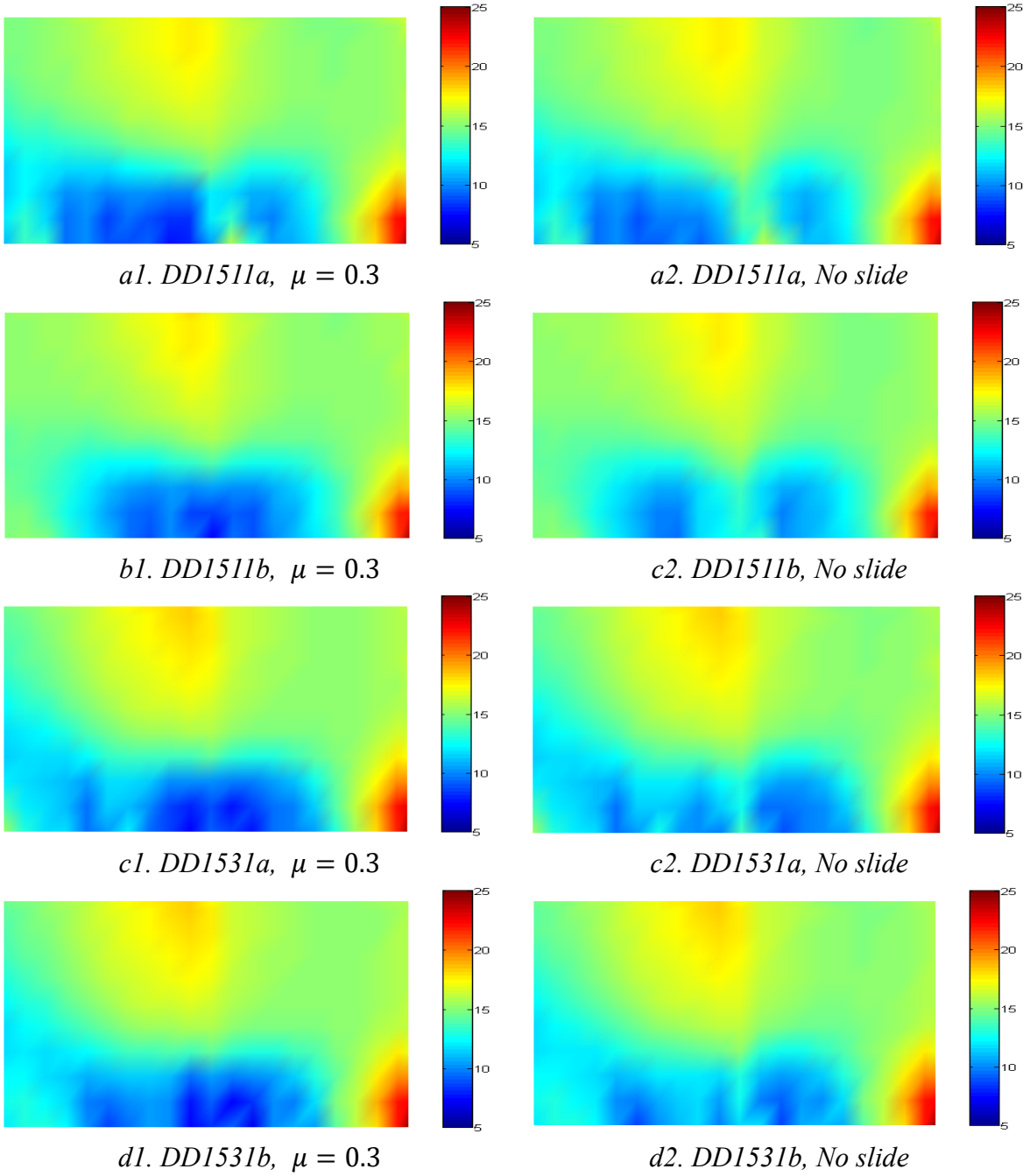

a1. DD1511a, $\mu = 0.3$ *a2. DD1511a, No slide*

b1. DD1511b, $\mu = 0.3$ *c2. DD1511b, No slide*

c1. DD1531a, $\mu = 0.3$ *c2. DD1531a, No slide*

d1. DD1531b, $\mu = 0.3$ *d2. DD1531b, No slide*

Figure 5.31 Nodal Mises stress distributions in pressurization tests

5.5 Summary

(a) The 3D smooth curved surface of *15%* rise ratio of saddle type of membrane structure could be established by drawing drape strips with several prescribed stress ratios. In this fabrication technique, the drawing values of *a* and *c* are determined by *2%* of span of structure, while the drawing values at corner of *b* is *1.5%* of span. The drawing values *d* are *2%* and *2.5%* for drape strips which used prescribed stress ratios between *MD* and *TD* directions in form finding analysis of *1:1* and *3:1*, respectively. Those drawing values will guarantee: (1) all parts of ETFE film got the introduced prestress of around its first yield point; (2) The absence of wrinkling was confirmed; (3) The tear of ETFE at corner edge was absented.

(b) The value of *0.3* of static friction coefficient between ETFE film and galvanized steel arch could be used positively in the prediction of the behavior of ETFE film during the stretch fabrication technique.

(c) The suggested analytical method in Chapter 4 was confirmed not only by the stretch fabrication tests but also by the pressurization tests.

(d) The pressurization tests confirmed the sufficient introduced prestress of ETFE film. The reduction of the rigidity of structures after the prestress construction stage was seen at the pressure of around 1.3kPa.

(e) The effect of friction contact between ETFE and galvanized steel arch on the distribution of stress in ETFE film was small in pressurization tests. The slide between ETFE and galvanized steel arch could be ignored if the external forces of ETFE film are balanced at both sides of arch.

Chapter 6.
Conclusion

Chapter 6. Conclusion

6.1 Conclusion

In this thesis, the analytical method which could solve the geometrical nonlinearity, the material nonlinearity and the nonlinearity of friction contact condition was developed. In addition, the stretch fabrication technique for saddle type of ETFE tensile membrane structure with less weld lines by drawing the combination of plane and/or drape strips was also established. The summaries of this thesis are listed below:

(1) The analytical method

The total Lagrangian formulations were established for both triangular membrane element and node-to-node contact element. The analytical procedure which used these formulations to solve the problems of the geometrical nonlinearity, the material nonlinearity and the nonlinearity of friction contact was also suggested. In this procedure, the incremental step-by-step solution was used. The status of node-to-node contact element from the discrete time t to the discrete time $t + \Delta t$ was assumed to be only in stick or slip condition. The stick-slip phenomenon could be occurred frequently within the assumptions of this study. When the slide condition is adapted, the slide direction is updated by the friction contact forces of node-to-node element in previous stick condition. On the other words, the stiffness and slide direction of node-to-node contact element were independent with the incremental nodal displacements from the discrete time t to the discrete time $t + \Delta t$. This work improved the convergence criteria during the static loading process. The accuracy and applicability of suggested analytical method are confirmed by the existing commercial software *ANSYS* for the frictionless case. Moreover, this method was effective for friction contact case too. The accuracy of proposed analytical method was confirmed by stretch fabrication experiments in both Mises stress and observed slide values between ETFE film and galvanized steel arches. The results of the proposed analytical method were in good agreement with the results of the experiments for the values *0.3* of static friction coefficient between ETFE and galvanized steel arches.

The small slide, however, was considered in this suggested analytical method. The effect of the change in normal contact direction during the loading process should be investigated to consider the large slide case.

(2) Stretch fabrication technique for saddle type of ETFE tensile membrane structure

In saddle type of tensile membrane structure using ETFE film, the form finding analysis

could be carried out with several prescribed stress ratios between the *MD* and *TD* directions. Those ratios were determined by the dimensions and the shapes of structures. The cutting pattern analysis based on the mathematical approach produced the drape strips without the consideration of prestress which correspond to the results of the form finding analysis. These drape strips were connected together and/or with plane strips, which are not draped, by heat seal lines into the specimens, and the boundary of these specimens was drawn to introduce the prestress. The 3D smooth curved surface with sufficient prestress could be established by those construction processes.

In case of the low-rise ratio (*10%*), the drawing the combination of drape strips of the *3:1* of prescribed stress ratio between *MD* and *TD* directions for the corner part and the plane strips for the middle part could establish the smooth curved surface.

In case of high-rise ratio (*15%*), the drape strips were also required for the middle part. Both of *1:1* or *3:1* of prescribed stress ratio between *MD* and *TD* directions for drape strips of the middle part could be used to establish the smooth curved surface. The adjustment of drawing values guaranteed that the introduced prestresses in those cases were almost the same. However, the saddle height of the final curved surface for the case of *1:1* of prescribed stress ratio was higher than that of *3:1* of prescribed stress ratio. Therefore, the prescribed stress ratios in form finding analysis should be chosen according to the viewpoints of architecture.

6.2 Application of the presented method in tensile membrane structure using ETFE film

(1) The value *0.3* of static friction coefficient between ETFE film and galvanized steel arches is recommended to evaluate the effect of friction contact during the introduced prestress stage.

(2) The suggested analytical method can be used to predict approximately the behavior of the ETFE film during the stretch fabrication process. The suggested method is simple and easily incorporated into existing nonlinear finite element programs.

(3) When the tensile membrane structure has the multiple supporting arches, the selection between drape strips, which are determined by several prescribed stress ratios in form finding analysis, and/or plane strips is recommended to establish the smooth curved surface. This selection depends on the dimensions and the required final shapes of the structures.

(4) The relationship between the motion of offset point of ETFE film and the drawing values was established. This relationship can be used to predict the behaviors of ETFE film and determine the drawing values in the practical construction.

References

References

[AN07] ANSYS Academic Research, Release 17.0, Help System, Elements Reference, ANSYS, Inc (2007)

[AS04] A. Socolius, R. Bennewitz, E. Gnecco, and E. Meyer: *Transition from Stick-Slip to continuous sliding in atomic friction: Entering a new regime of Ultralow friction*, Physical review letter, Vol. 92, Number 13, pp. 134301-1, 134301-4

[BM98] B. Maurin and R. Motro: *Form finding and cutting pattern of textile membranes: new theoretical developments*, Proceeding of Techtextile Symposium 98-Vol. 1, pp. 117-123, Lyon, France, 1998

[BT92] B. Tabarrok, Z. Qin: *Nonlinear analysis of tension structures*, Computers & Structures Vol. 45, No. 5/6, pp. 973-984, 1992

[BT93] B. Tabarrok, Z. Qin: *Form finding and cutting pattern generation for fabric tension structures*, Microcomputers in Civil Engineering, Vol.8, pp. 377-384, 1993

[BR09] B. Richard, S. Gordon: *Statistical methods in practice: for scientists and technologists*, Chichester, U.K.: Wiley. pp. 95‑96, 2009

[CG11] C. Galliot, R.H. Luchsinger: *Uniaxial and biaxial mechanical properties of ETFE foils*, Polymer Testing 30, 2011, pp. 356-365

[CH17] https://www.chemours.com/Teflon_Industrial/en_US/assets/downloads/tefzel-etfe-film-properties.pdf

[DP92] Djordje Peric and D. R. J. Owen: *Computational model for 3-D contact problems with friction based on the penalty method*, International Journal for numerical methods in engineering, Vol. 35, pp 1289-1309, 1992

[DR87] D.G. Roddeman, C.W.J. Oomens, J.D. Janssen and J. Drukker: *The*

wrinkling of thin membranes; Part I-Theory, ASME Journal of Applied Mechanics, Vol. 54, pp. 884-887, 1987

[DV12] D. Veenendaal and P. Block: *An overview and comparison of structural form finding methods for general networks*, International Journal of Solids and Structures, Vol.49, pp. 3741-3753, 2012

[EJ13] E. Jeong: *A study on visco-plastic behavior and stretch fabrication of tensile membrane structures using ETFE film*, PhD Thesis, 2013

[EJ14] E. Jeong and M. Kawabata: *An Experimental and Analytical Study on Stretching Effect of ETFE film*, Research Report on Membrane Structures, 2014

[FM06] F. Moriyama: *Study on viscoelastic behavior of ETFE film Pneumatic Structure*, PhD Thesis, 2006

[HN95] H. Noguchi and T. Hisada: *Integrated FEM formulation for Total/Updated-Lagrangian method in geometrically nonlinear problems*, JMSE In. J, Series A, Vol. 38, No.1, 1995, pp23-29

[HN01] H. Noguchi, T. Kawashima: *Formulation for geometrically non-linear analysis of membrane structures with cable reinforcement by ALE-EFGM*, Journal of the Japan Society of Mechanical Engineers (JSME), Vol. 67, No. 00-1438, pp 1276-1282, 2001 (in Japanese)

[HN04] H. Noguchi, T. Kawashima: *Meshfree analyses of cable-reinforced membrane structures by ALE-EFG method*, Engineering Analysis with Boundary Elements 28 (2004) 443-451

[HS95] Haruhiko Sakai, Eizaburou Tachibana: *Numerical analysis of cable reinforced membrane structures using foldable finite element*, Research report on Membrane structure, 1995 (in Japanese)

[HT89] H. Tsubota and A. Yoshida: *Theoretical analysis for determining cutting patterns for membrane structures by adopting optimization technique*, Journal of Structural and Construction Engineering, Transaction of AIJ, pp.

101-111, 1989 (in Japanese)

[HT93] H. Tsubota and A. Yoshida: *Determination of actual initial equilibrium state and optimum cutting patterns for membrane structures*, Proceedings of the Seiken-IASS Symposium on Nonlinear analysis and Design for shell and Spatial Structures, pp. 457-464, Tokyo, Japan, 1993

[JA74] J.H. Argyris, T. Angelopoulos, B. Bichat: *A general method for the shape finding of lightweight tension structures*, Computer Methods in Applied Mechanics and Engineering, Vol. 3, pp. 135-149, 1974

[JA17] Japan Architecture Institute: *Guidebook for Numerical Analysis of Spatial Structures, 2017*

[JCS85] J. C. Simo and R. L. Taylor: *Consistent Tangent Operators for Rate-Independent Elastoplasticity,* Comp. Meth. in Appl. Mech. and Eng., Vol. 48, 1985, pp. 101-118

[JCS86] J. C. Simo and R. L. Taylor: *A Return Mapping Algorithm for Plane Stress Elastoplasticity,* Int. J. for Num. Meth. in Eng., Vol. 22, 1986, pp. 649-670

[JO81] J.T. Oden: *Exterior penalty methods for contact problems in elasticity*, Nonlinear Finite Element Analysis in Structural Mechanics, Berlin, 1981, pp. 655-665

[JL08] J. Linhard, R. Wuchner and K. Bletzinger: *Introducing cutting patterns in form finding and structural analysis*, Textile Composites and Inflatable Structure II, pp. 69-84, 2008

[JS86] J.W. Simons and P.G. Bergan: *A finite element formulation of three-dimensional contact problems with slip and friction*, Computational Mechanics (1986) 1, 153-164

[KB76] K. Bathe and Haluk Ozdemir: *Elastic-plastic Large Deformation Static and Dynamic Analysis*, Computers & Structures, Vol. 6, pp. 81-92, 1976

[KB84] K. Bathe and A. Chaudhary: *On Finite Element Analysis of Large*

Deformation Frictional Contact Problems, Unified Finite Element Methods, North-Holland, Amsterdam, 1984

[KB99] K. Bletzinger, E. Ramm: *A general finite element approach to the form finding of tensile structures by the updated reference strategy*, International Journal of Space Structures, Vol. 14, pp. 131-145, 1999

[KI89] K. Ishii: *State of the art report on form finding problem of membrane structures*, Research Report on Membrane Structures, pp. 83-107, 1989

[KI90] K. Ishii: *State-of-the-art report on the stress deformation analysis of membrane structure*, MSA 1990, Japan, pp. 69-105

[KI99] K. Ishii: *Form finding analysis in consideration of cutting patterns of membrane structures*, International Journal of Space Structures Vol.14, No.2, 1999, pp.105-119

[MB88] M.R. Barnes: *Form finding and analysis of prestressed nets and membranes,* Computers and Structures, Vol. 30, pp.685-695, 1988

[MB99] M.R. Barnes: *Form finding and analysis of tension structures by dynamic relaxation,* International Journal of Space Structures, Vol. 14, pp.89-104, 1999

[MI99] Masatoshi Ishida, Haruji Tsubota, Yutaka Seto, Akihiro Kusaka: *Theoretical analysis for equilibrium state of membrane structures considering slide between cable and membrane element*, J. Struct. Constr. Eng., AIJ, No. 526, 77-84, Dec.,1999 (in Japanese)

[MK07] M. Kawabata: *Viscoplastic properties of ETFE film and structural behavior of fil, cushion,* Proceedings of the IASS Symposium, Venice, 2007

[MK08] M. Kawabata, E. Jeong and K. Nishikawa: *Curved surface fabrication and strengthening of film structures by stretching plane film*, Proceedings of IASS Symposium, 2008

[MO73] M. Ohnaka: *Experimental studies of stick-slip and their application to the*

earthquake source mechanism, Journal of Phys. Earth, Vol. 21, pp. 285-303, 1973

[MO00] M. Ohsaki and K. Uetani: *Shape-stress trade-off design of membrane structures for specified sequence of boundary shapes*, Comput. Methods Appl. Mech. Engrg. Vol. 182, pp. 73-88, 2000

[MW08] M. Wu, J. Lu: *Experimental studies on ETFE cushion model*, Proceedings of the IASS Symposium, Mexico, 2008

[NK15] N.-H. Kim: *Finite element analysis for contact problems*, Springer Science Business Media, New York, 2015 DOI 10.1007/978-1-4419-1746-1_5

[NK88] N. Kikuchi and J. T. Oden: *Contact Problems in Elasticity: Study of Variational Inequalities and Finite Element Methods*, SI AM Stud. Appl. Math., SIAM, New York, 1988

[NT93] N. Turkkan and K. Srivastava: *Development of a cutting pattern for a flexible structural membrane*, Proceedings of IASS Symposium on Public Assembly Structures from Antiquity to the Present, pp. 597-604, Istanbul, Turkey, 1993

[OZ05] O.C. Zienkiewicz and R.L. Taylor: *The finite element method for solid and structural mechanics*, Sixth Edition, Chapter 13, pp.434, 2005

[PC88] P. Contri, B.A. Schrefter: *A geometrically nonlinear finite element analysis of wrinkled membrane surfaces by a no-compression material model*, Communications in Appl. Num. Meth., Vol .4, pp. 5-15, 1988

[QB19] Q.H. Bui, M. Kawabata: *Total Lagrangian formulation for ETFE membrane structure considering friction contact*, Journal of Structural Engineering, Japan, Vol. 65B, March 2019

[RB09] R. Boddy; G. Smith: *Statistical methods in practice: for scientists and technologists*, Chichester, U.K.: Wiley. pp. 95‑96, 2009

[RH82] R. B. Haber, J.F. Abel: *Initial equilibrium solution methods for cable*

reinforced membranes. Part I – Formulations, Computer Methods in Applied Mechanics and Engineering, Vol. 30, pp. 263-284, 1982

[RH83] R. B. Haber and J.F. Abel: Contact-slip analysis using mixed displacements, Jour. of Eng. Mech., Vol. 109, No. 2, pp 411-429, 1983

[RH84] R. B. Haber: *A mixed Eulerian-Lagrangian displacement model for large-deformation analysis in solid mechanics*, Computer methods in applied mechanics and engineering, Vol. 43, pp 277-292, 1984

[RM82] R.K. Miller, J.M. Hedgepeth, V.I. Weingarten, P. Das and S. Kahyai: *An algorithm for finite element analysis of partly wrinkled membrane,* AIAA, Vol. 20, pp. 1761-1763, 1982

[RP08] R.M.O. Pauletti and P.M. Pimenta: *The natural force density method for the shape finding of taut structures,* Computer Methods in Applied Mechanics and Engineering, Vol. 197, pp. 4419-4428, 2008

[SL93] S.H. Lee: *Rudimentary considerations for adaptive Gap/Friction element based on the penalty method*, Computers & Structures, Vol. 47, No. 6, pp. 1043-1056, 1993

[SJ99] S.H. Ju, R.E. Rowlands: *A three-dimensional frictional contact element whose stiffness matrix is symmetric*, Journal of Applied Mechanics, Vol. 66, pp. 460-467, 1999

[SU95] S. Uchiyama, J.H. Coert, L. Berglund, P.C. Amadio, and K.N. An: *Method for the measurement of friction between tendon and pulley*, Journal of Orthopaedic Research, Vol.13, pp. 83-89, 1995

[TY98] T. Yagi and H. Ohmori: *A new approach for cutting pattern analysis of membrane structures,* Proceedings of IASS Symposium on Lightweight Structures in Architecture, pp. 895-910, Sydney, Australia, 1998

[TY04] T. Yoshino, S. Segawa, K. Oda: *"Material Characteristics of ETFE film under the bi-axial tension and stress-displacement analysis considering the elasto-plastic characteristics"*, Research Report on Membrane Structures, 2004

[UH86] U. Hangleiter and L. Grundig: *Cutting pattern for structural membranes*, Proceeding of 1sr. International Conference on Lightweight Structures in Architecture, pp. 279-286, Sydney, Australia, 1986

[YS14] Y. Sunami, Y. Fujiwara, Y. Kotobuki and H. Kashimoto: *Experimental study on friction characteristics between plastic film and steel roller*, The 3rd International Conference on Design Engineering and Science, pp. 160-164, 2014

[ZZ92] Zhi-Hua Zhong and Jaroslav Mackerle: *Static Contact Problems-A Review*, Engineering Computations, Vol. 9, pp.3-37, 1992

Published papers

Published papers

1. Peer-reviewed papers

Quang Hieu Bui, Masaya Kawabata: *"Nonlinear finite element procedure for membrane structures using ETFE films considering friction contact condition"*, Research Report on Membrane Structures 2016, The Membrane Structures Association of Japan, pp 9-14

Quang Hieu Bui, Masaya Kawabata: *"Total Lagrangian formulation for ETFE membrane structure considering friction contact",* Journal of Structural Engineering, Architectural Institute of Japan, Vol 65B, March 2019

Quang Hieu Bui, Masaya Kawabata: *"An experiment on fabrication technique to establish three-dimensional curved surface of ETFE membrane structure by stretching cutting pattern strips"*, Research Report on Membrane Structures, The Membrane Structures Association of Japan, April 2019 (Submitting)

2. Conference papers

Eisuke Ishida, Quang Hieu Bui, Masaya Kawabata: *"Study on fabrication of film panel of parallel arch model by three-dimensional composite cutting patter-Part I Study on combination of three-dimensional cutting and plane cutting"*, Architectural Institute of Japan, Conference, August 2018, pp. 739-740

Quang Hieu Bui, Masaya Kawabata: *"Nonlinear analysis of membrane structures using ETFE films considering the friction contact between the films and steel arch"*, Architectural Institute of Japan, Conference, August 2018, pp. 741-742

Acknowledgements

This thesis was carried out at the Space Structure Laboratory, Graduate School of Urban Innovation, Yokohama National University, under the supervision of Associate Professor Masaya Kawabata.

First and foremost, I would like to express my deep gratitude to my supervisor, Assoc. Prof. Masaya Kawabata for his extraordinary support and guidance, not only in the field of research, but in all aspects of university life. I am especially grateful for the time he devoted to this thesis, as well as for his patient guidance, enthusiastic encouragement.

Besides my supervisor, I would like to thank my examining committee: Prof. Yasuhisa Tagawa, Prof. Akira Tasai, Assoc. Prof. Kuniyoshi Sugimoto, and Assoc. Prof. Yuka Matsumoto for their comments, suggestions, discussions and even the hard questions.

I would like to address special thanks to Japanese Government Scholarship which supported the finance during my doctoral course. And the support for the stretch fabrication experiments from Taiyo Kogyo Corporation is also gratefully acknowledged.

My grateful thanks are extended to all members of Space Structure Laboratory, who readily helped me to carryout the experiments regardless of the time. Specially, I would really appreciate the support from Mr. Eisuke Ishida, who has accompanied me during the completion of the experiments.

I further wish to express my gratitude to my family for their helps, encouragement throughout the years in the PhD's life.

Finally, I would like to particularly thank my dear wife, Nguyen Xuan Huong, for her tremendous effort and invaluable help during my doctoral course. She quitted her favorite job as high-school teacher in Vietnam, worked part-time job in Japan, and always heard about the friction contact problem in membrane structures although her specialty is biology. Her love carried me through all the difficult times.

March 2019

BUI QUANG HIEU